



HAL
open science

Topology and Geometry of Gaussian random fields I: on Betti Numbers, Euler characteristic and Minkowski functionals

Pratyush Pranav, Rien van de Weygaert, Gert Vegter, Bernard J.T. Jones, Robert J. Adler, Job Feldbrugge, Changbom Park, Thomas Buchert, Michael Kerber

► To cite this version:

Pratyush Pranav, Rien van de Weygaert, Gert Vegter, Bernard J.T. Jones, Robert J. Adler, et al.. Topology and Geometry of Gaussian random fields I: on Betti Numbers, Euler characteristic and Minkowski functionals. Monthly Notices of the Royal Astronomical Society, 2019, 485 (3), pp.4167-4208. 10.1093/mnras/stz541 . hal-01975050

HAL Id: hal-01975050

<https://hal.science/hal-01975050v1>

Submitted on 4 Jul 2023

HAL is a multi-disciplinary open access archive for the deposit and dissemination of scientific research documents, whether they are published or not. The documents may come from teaching and research institutions in France or abroad, or from public or private research centers.

L'archive ouverte pluridisciplinaire **HAL**, est destinée au dépôt et à la diffusion de documents scientifiques de niveau recherche, publiés ou non, émanant des établissements d'enseignement et de recherche français ou étrangers, des laboratoires publics ou privés.

Topology and geometry of Gaussian random fields I: on Betti numbers, Euler characteristic, and Minkowski functionals

Pratyush Pranav¹,^{2,3}★ Rien van de Weygaert,² Gert Vegter,⁴ Bernard J. T. Jones,² Robert J. Adler,³ Job Feldbrugge,^{2,5} Changbom Park,⁶ Thomas Buchert¹ and Michael Kerber⁷

¹Univ Lyon, ENS de Lyon, Univ Lyon1, CNRS, Centre de Recherche Astrophysique de Lyon UMR5574, F-69007 Lyon, France

²Kapteyn Astronomical Institute, Univ. of Groningen, PO Box 800, NL-9700 AV Groningen, the Netherlands

³Technion – Israel Institute of Technology, Haifa 32000, Israel

⁴Johann Bernoulli Inst. for Mathematics and Computer Science, Univ. of Groningen, P.O. Box 407, NL-9700 AK Groningen, the Netherlands

⁵Perimeter Institute for Theoretical Physics, University of Waterloo, Waterloo ON N2L 2Y5, Canada

⁶Korean Institute of Advanced Studies, Hoegiro 87, Dongdaemun-gu, Seoul 130-722, Korea

⁷Institut für Geometrie, TU Graz, Kopernikusgasse 24A 8010 Graz

Accepted 2019 February 18. in original form 2018 December 18

ABSTRACT

This study presents a numerical analysis of the topology of a set of cosmologically interesting 3D Gaussian random fields in terms of their Betti numbers β_0 , β_1 , and β_2 . We show that Betti numbers entail a considerably richer characterization of the topology of the primordial density field. Of particular interest is that the Betti numbers specify which topological features – islands, cavities, or tunnels – define the spatial structure of the field. A principal characteristic of Gaussian fields is that the three Betti numbers dominate the topology at different density ranges. At extreme density levels, the topology is dominated by a single class of features. At low levels this is a *Swiss-cheeselike* topology dominated by isolated cavities, and, at high levels, a predominantly *Meatball-like* topology composed of isolated objects. At moderate density levels, two Betti numbers define a more *Sponge-like* topology. At mean density, the description of topology even needs three Betti numbers, quantifying a field consisting of several disconnected complexes, not of one connected and percolating overdensity. A *second* important aspect of Betti number statistics is that they are sensitive to the power spectrum. They reveal a monotonic trend, in which at a moderate density range, a lower spectral index corresponds to a considerably higher (relative) population of cavities and islands. We also assess the level of complementary information that the Betti numbers represent, in addition to conventional measures such as Minkowski functionals. To this end, we include an extensive description of the Gaussian Kinematic Formula, which represents a major theoretical underpinning for this discussion.

Key words: cosmology: theory – large-scale structure of universe – cosmic background radiation – methods: numerical – methods: data analysis – methods: statistical.

1 INTRODUCTION

The richness of the big data samples emerging from astronomical experiments and simulations demands increasingly complex algorithms in order to derive maximal benefit from their existence. Generally speaking, most current analyses express inter-

relationships between quantitative properties of the data sets, rather than geometric or topological, i.e. structural, properties.

In this study, we introduce a new technique that successfully attacks the problem of characterizing the structural nature of data. This exercise involves an excursion into the relatively complex and unfamiliar domain of *homology*, which we attempt to present in a straightforward manner that should enable others to use and extend this aspect of data analysis. On the application side, we demonstrate the power of the formalism through a systematic study of Gaussian random fields using this novel methodology.

* E-mail: pratyuze@gmail.com, pratyush.pranav@ens-lyon.fr

A Gaussian random field is a stochastic process, X , defined over some parameter space of S , and characterized by the fact that the vector $(X(s_1), \dots, X(s_k))$ has a k -dimensional, multivariate normal distribution for any collection of points (s_1, \dots, s_k) in S . Gaussian random fields play a key role in cosmology: in the standard cosmological view, the primordial density and velocity fields have a Gaussian character, making Gaussian fields the initial conditions for the formation of all structure in the Universe. A Gaussian random field is fully specified by its power spectrum, or in the real space, its correlation function. As a result, the determination and characterization of the power spectrum of the theoretical models, as well as observational data, has been one of the main focal points in the analysis of the primordial cosmic fluctuation field as well as the Megaparsec – large scale – matter and galaxy distribution at low redshifts.

A substantial body of theoretical and observational evidence underpins the assumption of Gaussianity of the primordial cosmic density and velocity fields. These have established Gaussian random fields as a prominent aspect of the current standard cosmological worldview. The primary evidence for this is the near-perfect Gaussian nature of the Cosmic Microwave Background (CMB) radiation temperature fluctuations. These directly reflect the density and velocity perturbations on the surface of last scattering, and thus the mass distribution at the recombination and decoupling epoch 379 000 yr after the big bang, at a redshift of $z \approx 1090$ (see e.g. Peebles 1980; Jones 2017). In particular the measurements by the *COBE*, *WMAP*, and *Planck* satellites established that, to a high accuracy, the CMB temperature fluctuations define a homogeneous and isotropic Gaussian random field (Smoot et al. 1992; Bennett et al. 2003; Spergel et al. 2007; Komatsu et al. 2011; Planck Collaboration XIII 2016; Buchert, France & Steiner 2017; Aghanim et al. 2018). Second, that the primordial fluctuations have a Gaussian nature, narrowly follows from the theoretical predictions of the inflationary scenario, at least in its simplest forms. According to this fundamental cosmological theory, the early Universe underwent a phase transition at around $t \approx 10^{-35}$ s after the big bang (Guth 1981; Linde 1981; Kolb, Salopek & Turner 1990; Liddle & Lyth 2000). As a result, the Universe underwent a rapid exponential expansion over at least 60 e-foldings. The inflationary expansion of quantum fluctuations in the generating inflation (field) leads to a key implication of this process, the generation of cosmic density, and velocity fluctuations. It involves the prediction of the resulting density fluctuation field being adiabatic and a homogeneous Gaussian random field, with a near scale-free Harrison–Zeldovich spectrum, $P(k) \propto k^1$ (Harrison 1970; Zeldovich 1972; Mukhanov & Chibisov 1981; Guth & Pi 1982; Starobinsky 1982; Bardeen, Steinhardt & Turner 1983). Third, the *Central Limit Theorem* states that the statistical distribution of a sum of many independent and identically distributed random variables will tend to assume a Gaussian distribution. Given that when the Fourier components of a primordial density and velocity field are statistically independent, each having the same Gaussian distribution, then the joint probability of the density evaluated at a finite number of points will be Gaussian (Bardeen et al. 1986).

On the basis of these facts, Gaussian random fields have played a central role in describing a multitude of fields of interest that arise in cosmology, making their characterization an important focal point in cosmological studies (Doroshkevich 1970; Bardeen et al. 1986; Hamilton, Gott & Weinberg 1986; Bertschinger 1987; Mecke & Wagner 1991; Scaramella & Vittorio 1991; Mecke, Buchert & Wagner 1994; van de Weygaert & Bertschinger 1996; Schmalzing & Buchert 1997; Matsubara 2010). When assessing the structure and

patterns of the temperature fluctuations in the CMB, the interest is that of Gaussian fields on the 2D surface of a sphere, i.e. on 2D space S^2 . When studying the cosmic galaxy and matter distribution, the parameter space is that of a large, but essentially fine, subset of 3D space \mathbb{R}^3 (i.e. assuming curvature of space is almost perfectly flat, as has been inferred from the *WMAP* and *Planck* CMB measurements; Spergel et al. 2007; Planck Collaboration XIII 2016).

In this study, we address the topological characteristics of 3D Gaussian fields, specifically in terms of the topological concepts and language of homology (Munkres 1984; Robins 2006; Rote & Vegter 2006; Zomorodian 2009; Edelsbrunner & Harer 2010; Robins 2013; Robins 2015). These concepts are new to cosmology (see below) and will enrich the analysis of cosmological data sets considerably (see e.g. Adler, Agami & Pranav 2017; Elbers & van de Weygaert 2018). The principal rationale for this study of Gaussian field homology is the definition and development of a reference base line. In most cosmological scenarios Gaussian fields represent the primordial mass distribution out of which 13.8 Gyr of gravitational evolution has morphed the current cosmic mass distribution. Hence, for a proper understanding of the rich (persistent) homology of the cosmic web, a full assessment of Gaussian field homology as reference point is imperative.

Topology is the branch of mathematics that is concerned with the properties of space that are preserved under continuous deformations, including stretching (compression) and bending, but excluding tearing or glueing. It also includes invariance of properties such as connectedness and boundary. As such it addresses key aspects of the structure of spatial patterns, the ones concerning the organization, i.e. shape, and connectivity (see e.g. Robins 2006; Robins 2013; Patania, Vaccarino & Petri 2017). The topological characterization of the models of cosmic mass distribution has been a focal point of many studies (Doroshkevich 1970; Adler 1981; Bardeen et al. 1986; Gott, Dickinson & Melott 1986; Hamilton et al. 1986; Canavezes et al. 1998; Canavezes & Efstathiou 2004; Pogosyan, Gay & Pichon 2009; Choi et al. 2010; Park & Kim 2010). Such topological studies provide insights into the global structure, organization, and connectivity of cosmic density fields. These aspects provide key insight into how these structures emerged, and subsequently interacted and merged with neighbouring features. Particularly helpful in this context is that topological measures are relatively insensitive to systematic effects such as non-linear gravitational evolution, galaxy biasing, and redshift-space distortion (Park & Kim 2010).

The vast majority of studies of the topological characteristics of the cosmic mass distribution concentrate on the measurement of the genus and the Euler characteristic (Gott et al. 1986; Hamilton et al. 1986; Gott et al. 1989). The notion of genus is, technically, only well defined for 2D surfaces, where it is a simple linear function of the Euler characteristic. For 3D manifolds with smooth boundaries, there is also a simple relationship between the Euler characteristic of a set and the genus of its boundary. Beyond these examples, however, these relationships break down and, in higher dimensions, only the Euler characteristic is well defined. We will therefore typically work with the Euler characteristic, rather than the genus, even when both are defined.

While the genus, the Euler characteristic – and the Minkowski functionals discussed below – have been extremely instructive in gaining an understanding of the topology of the mass distribution in the Universe, there is a substantial scope for an enhancement of the topological characterization in terms of a richer and more informative description. In this study, we present a topological

analysis of Gaussian random fields through *homology* (Munkres 1984; Adler et al. 2010; Edelsbrunner & Harer 2010; van de Weygaert et al. 2011; Feldbrugge & van Engelen 2012; Park et al. 2013; Bobrowski & Kahle 2014; Kahle 2014; Pranav et al. 2017; Wasserman 2018). Homology is a mathematical formalism for specifying in a quantitative and unambiguous manner about how a space is connected,¹ through assessing the boundaries of a manifold (Munkres 1984). To this end, we evaluate the topology of a manifold in terms of the holes that it contains, by assessing their boundaries.

A d -manifold can be composed of topological holes of 0 up to d – dimensions. For $d < 3$, the holes have an intuitive interpretation. A 0-dimensional hole is a *gap* between two isolated independent objects. A 1D hole is a *tunnel* through which one can pass in any one direction without encountering a boundary. A 2D hole is a *cavity* or *void* fully enclosed within a 2D surface. This intuitive interpretation in terms of *gaps* and *tunnels* is only valid for surfaces embedded in \mathbb{R}^3 , \mathbb{S}^3 , or \mathbb{T}^3 . Following the realization that the identity, shape, and outline of these entities is more straightforward to describe in terms of their boundaries, homology turns to the definition of holes via *cycles*. A 0-cycle is a connected object (and hence, a 0-hole is the gap between two independent objects). A 1-cycle is a *loop* that surrounds a tunnel. A 2-cycle is a *shell* enclosing a void. The d -cycle for a d -dimensional manifold is trivially zero till the superlevel set includes the whole manifold, and one otherwise.

The statistics of the holes in a manifold and their boundaries are captured by its *Betti numbers*. Formally, the Betti numbers are the ranks of the homology groups. The p -th homology group is the assembly of all p -dimensional cycles of the manifold, and the rank of the group is the number of *independent* cycles. In all, there are $d + 1$ Betti numbers β_p , where $p = 0, \dots, d$ (Betti 1871; Vegter 1997; Robins 2006; Rote & Vegter 2006; Edelsbrunner & Harer 2010; van de Weygaert et al. 2011; Robins 2013; Pranav et al. 2017). The first three Betti numbers have intuitive meanings: β_0 counts the number of independent components, β_1 counts the number of loops enclosing the independent tunnels, and β_2 counts the number of shells enclosing the isolated voids.

There is a profound relationship between the homology characterization in terms of Betti numbers and the Euler characteristic. The *Euler-Poincaré* formula (Euler 1758) states that the Euler characteristic is the alternating sum of the Betti numbers (see Equation 35 below). One immediate implication of this is that the set of Betti numbers contain more topological information than is expressed by the Euler characteristic (and hence the genus used in cosmological applications). Visually imagining the 3D situation as the projection of three Betti numbers on to a 1D line, we may directly appreciate that two manifolds that are branded as topologically equivalent in terms of their Euler characteristic may actually turn out to possess intrinsically different topologies when described in the richer language of homology. Evidently, in a cosmological context this will lead to a significant increase of the ability of topological analyses to discriminate between different cosmic structure formation scenarios.

The Euler characteristic of a set is an essentially topological quantity. For example, the Euler characteristic of a 3D set is the number of its connected components, minus the number of its holes, plus the number of voids it contains (where each of the terms requires careful definition). Numbers are important here, but the sizes and shapes of

the various objects are not. Nevertheless, it is a deep result, known as the Gauss–Bonnet–Chern–Alexandrov Theorem, going back to Euler (1758), requiring both Differential and Algebraic Topology² to prove that – at least for smooth, stratified manifolds³ – the Euler characteristics can actually be computed from geometric quantities. That is, the Euler characteristic also has a geometric interpretation and is actually associated with the integrated Gaussian curvature of a manifold. In fact, together with other quantities related to volume, area, and length, the Euler characteristic forms a part of a more extensive geometrical description via the *Minkowski functionals*, or *Lipschitz-Killing curvatures* of a set.

There are $d + 1$ Minkowski functionals, $\{Q_k\}_{k=0, \dots, d}$, defined over nice subsets of \mathbb{R}^d (Mecke et al. 1994; Schmalzing & Buchert 1997; Sahni, Sathyprakash & Shandarin 1998; Schmalzing et al. 1999; Kerscher 2000). All are predominantly geometric in nature. For compact subsets of \mathbb{R}^3 , the four Minkowski functionals, in increasing order, are proportional to volume, surface area, integrated mean curvature, or total contour length, and integrated Gaussian curvature, itself proportional to the Euler characteristic. Analyses based on Minkowski functionals, genus, and Euler characteristic have played key roles in understanding and testing models and observational data of the cosmic mass distribution (Gott et al. 1986; Hamilton et al. 1986; Mecke et al. 1994; Kerscher et al. 1997; Schmalzing & Buchert 1997; Canavezes et al. 1998; Kerscher et al. 1998; Sahni et al. 1998; Kerscher et al. 1999, 2001; Hikage et al. 2003; Canavezes & Efstathiou 2004; Pogosyan et al. 2009; Choi et al. 2010; Park & Kim 2010; van de Weygaert et al. 2011; Codis et al. 2013; Park et al. 2013; Wiegand, Buchert & Ostermann 2014). Generalizations of Minkowski functionals for vector and tensor fields have also been applied in cosmology and have been useful in quantifying substructures in galaxy clusters (Beisbart, Buchert & Wagner 2001). Tensor-valued Minkowski functionals allow to probe directional information and to characterize preferred directions, e.g. to measure the anisotropic signal of redshift space distortions (Appleby et al. 2018), or to characterize anisotropies and departures from Gaussianity in the CMB (Chingangbam et al. 2017; Ganesan & Chingangbam 2017; Joby et al. 2019).

The topological analysis of Gaussian fields using genus, Euler characteristic, and Minkowski functionals has occupied a place of key importance within the methods and formalisms enumerated above. Of fundamental importance, in this respect, has been the realization that the expected value of the genus in the case of a 2D manifold, and the Euler characteristic in the case of a 3D manifold, as a function of density threshold has an analytic closed form expression for Gaussian random fields (Adler 1981; Bardeen et al. 1986; Adler & Taylor 2010). Amongst others, this makes them an ideal tool for validating the hypothesis of initial Gaussian conditions through a comparison with the observational data. Important to note is that the functional form of the genus, the Euler characteristic, and the Minkowski functionals is independent of the specification of the power spectrum for Gaussian fields, and is a function only of the dimensionless density threshold ν . The contribution from power

²Algebraic Topology is a branch of mathematics that uses concepts from abstract algebra to study topological spaces. Differential Topology is the field of mathematics dealing with differentiable functions on differentiable manifolds.

³A topologically stratified manifold \mathbb{M} is a space that has been decomposed into pieces called strata; these strata are topological submanifolds and are required to fit together in a certain way. Technically, \mathbb{M} needs to be a ‘ C^2 Whitney stratified manifold’ satisfying mild side conditions (Adler & Taylor 2010).

¹There is a notion of k -connectedness, $k = 0, \dots, d$, where d is the dimension of the manifold. Within this, 0-connectedness is the same as the ‘usual’ notion of connectedness.

spectrum is restricted to the amplitude of the genus curve through the variance of the distribution, or equivalently, the amplitude of the power spectrum. This indicates that the shape of these quantities is invariant with respect to the choice of the power spectrum. While this makes them highly suitable measures for testing fundamental cosmological questions such as the Gaussian nature of primordial perturbations, they are less suited when testing for differences between different structure formation scenarios is the primary focus.

Given the evident importance of being able to refer to solid analytical expressions, in this study we will report on the fundamental developments of the past decade which have demonstrated that the analytic expressions for the genus, Euler characteristic, and Minkowski functionals of Gaussian fields belong to an extensive family of such formulae, all emanating from the so-called *Gaussian kinematic formula* or GKF (Adler & Taylor 2010, 2011; Adler, Taylor & Worsley 2018). The GKF, in one compact formula, gives the expected values of the Euler characteristic (and so genus), all the Lipschitz-Killing curvatures, and so Minkowski functionals, as well as their extensions, for the superlevel sets (and their generalizations in vector-valued cases) of a wide class of random fields, both Gaussian and only related somehow to Gaussian. This is for both homogeneous and non-homogeneous cases, and cover all examples required in cosmology. Even though hardly known in the cosmological and physics literature, its relevance and application potential for the study of cosmological matter and galaxy distributions, as well as other general scenarios, is self-evident (see e.g. Codis et al. 2013).

Because of its central role for understanding a range of relevant topological characteristics of Gaussian and other random fields, we discuss the GKF extensively in Section 4. Of conclusive importance for the present study, the interesting observation is that homology and the associated quantifiers such as Betti numbers are not covered by the GKF. In fact, a detailed and complete statistical theory parallel to the GKF for them does not exist. In this respect, it is good to realize that the GKF is mainly about geometric quantifiers. The exception to this is the Euler characteristic. Nonetheless, in a sense the latter may also be seen as a geometric quantity via the Gauss–Bonnet Theorem. To date there is no indication that – along the lines of the GKF – an analytical description for Betti numbers and other homological concepts is feasible (also see Wintraecken & Vegter 2013). Nonetheless, this does not exclude the possibility of analytical expressions obtained via alternative routes. One example is analytical expressions for asymptotic situations, such as those for Gaussian field excursion sets at very high levels. For this situation, the seminal study by Bardeen et al. (1986) obtained the statistical distribution for Betti numbers, i.e. for the *islands* and *cavities* in the cosmic matter distribution. Even more generic is the approach followed by the recent study of Feldbrugge & van Engelen (2012); (Feldbrugge et al., in preparation). They derived path integral expressions for Betti numbers and additional homology measures, such as persistence diagrams. While it is not trivial to convert these into concise formulae, the numerically evaluated approximate expression for 2D Betti numbers turns out to be remarkably accurate.

This paper presents a numerical investigation of the topological properties of Gaussian random fields through homology and Betti numbers. Given the observation that generic analytical expressions for their statistical distribution are not available, this study is mainly computational and numerical. It numerically infers and analyses the statistical properties of Betti numbers, as well as those of the corresponding Euler characteristic and Minkowski functionals.

The extensive analysis concerns a large set of 3D Gaussian field realizations, for a range of different power spectra, generated in cubic volumes with periodic boundary conditions.

In an earlier preliminary paper (Park et al. 2013), we presented brief but important aspects of the analysis of the homology of 3D Gaussian random fields via Betti numbers. It illustrated the thesis forwarded in van de Weygaert et al. (2011) that Betti numbers represent a richer source of topological information than the Euler characteristic. For example, while the latter is insensitive to the power spectrum, Betti numbers reveal a systematic dependence on power spectrum. It confirms the impression of homology and Betti numbers as providing the next level of topological information. This paper extends this study to a more elaborate exploration of the property of Gaussian random fields as measured by the Betti numbers, paying particular attention to the statistical aspects. Together with the information contained in Minkowski functionals, it shows that homology establishes a more comprehensive and detailed picture of the topology and morphology of the cosmological theories and structure formation scenarios.

A powerful extension of homology is its hierarchical variant called *persistent homology*. The related numerical analysis of the persistent homology of the set of Gaussian field realizations presented in this paper is the subject of the upcoming related article (Pranav et al., in preparation). Our work follows up on early explorations of Gaussian field homology by Adler & Bobrowski (Adler et al. 2010; Bobrowski 2012; Bobrowski & Borman 2012). These studies address fundamental and generic aspects, and are strongly analytically inclined, but also give numerical results on Gaussian field homology. Particularly insightful were the presented results on their persistent homology in terms of bar diagrams.

In addition to the topological analysis of Gaussian fields by means of genus, Minkowski functionals, and Betti numbers, we also include a thorough discussion of the computational procedure that was used for evaluating Betti numbers. The homology computational procedure detailed in Pranav et al. (2017) is for a *discrete particle distribution*. On the other hand, in this paper, we detail the homology procedure for evaluating the Betti numbers for random fields whose values have been sampled on a *regular cubical grid*. The procedure is generic and can be used for the full Betti number and persistence analysis of arbitrary random fields. In the case of Gaussian fields, one may exploit the inherent symmetries of Gaussian fields to compute only two Betti numbers, from which one may then seek to determine the third one via the analytical expectation value for the Euler characteristic. Indeed, this is the shortcut that was followed in our preliminary study (Park et al. 2013).

This study, along with earlier articles (van de Weygaert et al. 2011; Pranav 2015; Pranav et al. 2017), gives the fundamental framework and so forms the basis of a planned series of articles aimed at introducing the topological concepts and language of homology – new to cosmology – for the analysis and description of the cosmic mass distribution. They define a program for an elaborate topological data analysis of cosmological data (see Wasserman 2018, for an up-to-date review of topological data analysis in a range of scientific applications). The basic framework, early results, and program are described and reviewed in van de Weygaert et al. (2011), which introduced the concepts of homology to the cosmological community. Following this, in Pranav (2015) and Pranav et al. (2017) we described in formal detail the mathematical foundations and computational aspects of topology, homology, and persistence. These provide the basis for our program to analyse and distinguish between models of cosmic structure formation in terms

of their topological characteristics, working from the expectation that they offer a considerably richer, more profound, and insightful characterization of their topological structure.

Our program follows the steadily increasing realization in the cosmological community that homology and persistent homology offer a range of innovative tools towards the description and analysis of the complex spatial patterns that have emerged from the gravitational evolution of the cosmic matter distribution from its primordial Gaussian conditions to the intricate spatial network of the cosmic web seen in the current Universe on Megaparsec scales. In this respect, we may refer to the seminal contribution by Sousbie (2011); Sousbie, Pichon & Kawahara (2011) (see also Shivashankar et al. 2016), and the recent studies applying these topological measures to various cosmological and astronomical scenarios (van de Weygaert et al. 2011; Park et al. 2013; Chen et al. 2015; Shivashankar et al. 2016; Adler et al. 2017; Makarenko et al. 2017; Codis, Pogosyan & Pichon 2018; Cole & Shiu 2018; Makarenko et al. 2018; Xu et al. 2018).

The remainder of the paper is structured as follows: We begin in Section 2 by providing an introduction to Gaussian random fields, and the presentation of the set of Gaussian field realizations that forms the basis of this study’s numerical investigation. A description of the topological background follows in Section 3. Gaussian fields and topology are then combined in Section 4 with a discussion of the GKF, which gives a rigorous formulation of what is known about mean Euler characteristic and Minkowski Functionals for Gaussian level sets. This section also explains why, with topological quantifiers such as Betti numbers, analytic results at least appear far from trivial to obtain. These sections all describe pre-existing material, but it is their combination which represents a novel approach towards characterizing the rich topology of cosmological density fields. The novel computational aspects of this study are outlined in detail in Section 5. This is followed by a description of the model realizations used for the computational studies in Section 6. Section 7 describes the Betti number analysis of our sample of Gaussian random field realizations. Subsequently, the relationship and differences between the distribution of ‘islands’ and ‘peaks’ in a Gaussian random field is investigated in Section 8. This is followed in Section 9 by an assessment of the comparative information content of Minkowski functionals and Betti numbers. The homology characteristics of the LCDM Gaussian field are discussed in Section 10. Finally, we conclude the paper with some general discussion in Section 11.

2 GAUSSIAN RANDOM FIELDS: DEFINITIONS

In this section, we define the basic concepts of Gaussian random fields, along with definitions and a description of the models analysed in this paper. Standard references for the material in this section are Adler (1981) and Bardeen et al. (1986).

2.1 Definitions

Recall that, at the most basic level, a *random field* is simply a collection of random variables, $f(x)$, where the values of x run over some parameter space \mathcal{X} . This space might be finite or infinite, countable or not. The probabilistic properties of random fields are determined by their m -point, joint, distribution functions,

$$P[f_1, \dots, f_m] df_1 \dots df_m, \quad (1)$$

where the f_1, \dots, f_m are the values of the random field at m points x_1, \dots, x_m .

A random field is called *zero mean, Gaussian*, if the m -point distributions are all multivariate Gaussian, so that

$$P[f_1, \dots, f_m] df_1 \dots df_m = \frac{1}{(2\pi)^N (\det M)^{1/2}} \times \exp\left(-\frac{1}{2} \sum f_i (M^{-1})_{ij} f_j\right) df_1 \dots df_m, \quad (2)$$

where M is the $m \times m$ covariance matrix of the f_i , determined by the covariance or autocovariance function

$$\xi(x_1, x_2) = \langle f(x_1) f(x_2) \rangle \quad (3)$$

via the correspondence

$$M_{ij} = \xi(x_i, x_j). \quad (4)$$

The angle bracket in (3) denotes ensemble averaging.

It follows from (2) that the distribution of zero mean Gaussian random fields is fully specified by second-order moments, as expressed via the autocovariance function. (From now on we shall always assume zero mean.) If we now specialize to random fields defined over \mathbb{R}^D , $D \geq 1$, so that the points in the parameter set are vectors, we can introduce the notions of *homogeneity* (or *stationarity*) and *isotropy*. A Gaussian random field is called homogeneous if $\xi(\vec{x}, \vec{y})$ can be written as a function of the difference $\vec{x} - \vec{y}$, and isotropic if it is also a function only of the (absolute) distance $\|\vec{x} - \vec{y}\|$. In the homogeneous, isotropic, case we write, with some abuse of notation,

$$\xi(r) = \xi(\|\vec{r}\|) \equiv \langle f(\vec{x}) f(\vec{x} + \vec{r}) \rangle. \quad (5)$$

An immediate consequence of homogeneity is that the variance

$$\sigma^2 = \xi(0) = \langle f^2(\vec{x}) \rangle \quad (6)$$

of f is constant. Normalizing the autocovariance function by σ^2 gives the *autocorrelation function*.

In many situations and generally for cosmological applications of homogeneous random fields, it is more natural to work with the Fourier transform

$$\begin{aligned} \hat{f}(\vec{k}) &= \int_{\mathbb{R}^D} d^D \vec{x} f(\vec{x}) \exp(i\vec{k} \cdot \vec{x}), \\ f(\vec{x}) &= \int_{\mathbb{R}^D} \frac{d^D \vec{k}}{(2\pi)^D} \hat{f}(\vec{k}) \exp(-i\vec{k} \cdot \vec{x}) \end{aligned} \quad (7)$$

of both f and, particularly, its autocovariance function ξ . The Fourier transform of ξ is known as the *power spectrum* $P(\vec{k})$. Here, and throughout our study, we follow the Fourier convention of Bardeen et al. (1986).⁴ For a random field to be strictly homogeneous and Gaussian, its Fourier modes $\hat{f}(\vec{k})$ must be mutually independent, and the real and imaginary parts $\hat{f}_r(\vec{k})$ and $\hat{f}_i(\vec{k})$,

$$\hat{f}(\vec{k}) = \hat{f}_r(\vec{k}) + i \hat{f}_i(\vec{k}), \quad (8)$$

each have a Gaussian distribution, whose dispersion is given by the value of the power spectrum for the corresponding wavenumber \vec{k} ,

$$\begin{aligned} P(\hat{f}_r(\vec{k})) &= \frac{1}{\sqrt{2\pi} P(\vec{k})} \exp\left(-\frac{\hat{f}_r^2(\vec{k})}{2P(\vec{k})}\right), \\ P(\hat{f}_i(\vec{k})) &= \frac{1}{\sqrt{2\pi} P(\vec{k})} \exp\left(-\frac{\hat{f}_i^2(\vec{k})}{2P(\vec{k})}\right). \end{aligned} \quad (9)$$

This means that the Fourier phases $\hat{\phi}(\vec{k})$,

$$\hat{f}(\vec{k}) = \|\hat{f}(\vec{k})\| e^{i\hat{\phi}(\vec{k})}, \quad (10)$$

⁴also known as ‘Kaiser convention’, personal communication.

of the field are random, i.e. if the phases $\hat{\phi}(\vec{k})$ have a uniform distribution, $U[0, 2\pi]$. The moduli $|\hat{f}(\vec{k})|$ have a Rayleigh distribution (Bardeen et al. 1986).

Under an assumption of ergodicity, which we will assume throughout, the power spectrum, denoted by $P(\vec{k})$, is continuous. For $\vec{k} \in \mathbb{R}^D$ this leads to

$$(2\pi)^D P(\vec{k}) \delta_D(\vec{k} - \vec{k}') = \langle \hat{f}(\vec{k}) \hat{f}^*(\vec{k}') \rangle, \quad (11)$$

where δ_D is the Dirac delta function.

In the case of isotropic f , P is spherically symmetric, and, once again abusing notation, we write

$$P(k) = P(\|\vec{k}\|) = P(\vec{k}). \quad (12)$$

The power spectrum breaks down the total variance of f into components at different frequencies, in the sense that

$$\begin{aligned} \sigma^2 &= \int_{\mathbb{R}^D} \frac{d^D \vec{k}}{(2\pi)^D} P(\vec{k}) = \frac{2}{(4\pi)^{D/2} \Gamma(D/2)} \int_0^\infty dk k^{D-1} P(k) \\ &= \frac{2}{(4\pi)^{D/2} \Gamma(D/2)} \int_0^\infty d(\ln k) k^D P(k). \end{aligned} \quad (13)$$

where $\Gamma(x)$ is the Gamma function. From this, one can interpret $k^D P(k)$ – with the addition as the contribution of the power spectrum, on a logarithmic scale, to the total variance of the density field. The numerical prefactors can be computed with the help of the recurrence relation $\Gamma(1+x) = x\Gamma(x)$, and the values $\Gamma(1) = 1$ and $\Gamma(1/2) = \sqrt{\pi}$ for the Gamma function. For 2D space, $D = 2$, the field variance σ^2 is given by

$$\sigma^2 = \frac{1}{2\pi} \int_0^\infty d(\ln k) k^2 P(k), \quad (14)$$

while for 3D space, $D = 3$, we have

$$\sigma^2 = \frac{1}{2\pi^2} \int_0^\infty d(\ln k) k^3 P(k). \quad (15)$$

Finally, we make the observation that since the distribution of a homogeneous Gaussian random field is completely determined by its covariance function, the distribution of isotropic Gaussian fields is determined purely and fully by the spectral density $P(k)$.

2.2 Filtered fields

When assessing the mass distribution by a continuous density field, $f(\vec{x})$, a common practice in cosmology is to identify structures of a particular scale R_s by studying the field smoothed at that scale. This is accomplished by means of a convolution of the field $f(\vec{x})$ with a particular smoothing kernel function $W_s(\vec{r}; R_s)$,

$$f_s(\vec{x}) = \int f(\vec{y}) W_s(\vec{y} - \vec{x}; R_s) d\vec{y}. \quad (16)$$

Following Parseval's theorem, this can be written in terms of the Fourier integral,

$$f_s(\vec{x}) = \int_{\mathbb{R}^3} \frac{d^3 \vec{k}}{(2\pi)^3} \hat{f}(\vec{k}) \hat{W}(k R_s) \exp(-i\vec{k} \cdot \vec{x}), \quad (17)$$

in which $\hat{W}(k R_s)$ is the Fourier transform of the filter kernel. From this, it is straightforward to see that the corresponding power spectrum $P_s(k)$ of the filtered field is the product of the unfiltered power spectrum $P(k)$ and the square of the filter kernel $\hat{W}(k R_s)$

$$P_s(k; R_s) = P(k) \hat{W}^2(k R_s). \quad (18)$$

2.3 Excursion sets

The *superlevel sets* of the smoothed field $f_s(\vec{x})$ define a manifold \mathbb{M}_ν and consists of the regions

$$\begin{aligned} \mathbb{M}_\nu &= \{\vec{x} \in \mathbb{M} \mid f_s(\vec{x}) \in [f_\nu, \infty)\} \\ &= f_s^{-1}[f_\nu, \infty). \end{aligned} \quad (19)$$

In other words, they are the regions where the smoothed density is less than or equal to the threshold value f_ν ,

$$\nu = \frac{f_\nu}{\sigma}, \quad (20)$$

with σ the dispersion of the smoothed density field.

Our analysis of the Betti numbers, Euler characteristic, and Minkowski functionals of Gaussian random fields consists of a systematic study of the variation of these topological and geometric quantities as a function of excursion manifolds \mathbb{M}_ν , i.e. as a function of density field threshold ν . In other words, we investigate topological and geometric quantities as function of density parameter ν .

3 TOPOLOGY AND GEOMETRY: BETTI NUMBERS, EULER CHARACTERISTIC, AND MINKOWSKI FUNCTIONALS

In this section, we first define the cosmologically familiar genus, Euler characteristic, and the Minkowski functionals. Subsequently, we give an informal presentation and a summary on the theory of homology, and the concepts essential to its formulation. For a more detailed description, in a cosmological framework, we refer the reader to van de Weygaert et al. (2010), van de Weygaert et al. (2011), Pranav (2015), and Pranav et al. (2017).

3.1 Euler characteristic and genus

The Euler characteristic (or Euler number, or Euler-Poincaré characteristic) is a topological invariant, an integer that describes aspects of a topological space's shape or structure regardless of the way it is bent. It was originally defined for polyhedra but, as we will see in the following subsection, has deep ties with homological algebra.

Despite this generality, for the moment we will concentrate on the 2D and 3D settings, since these are the most relevant to cosmology. Suppose \mathbb{M} is a solid body in \mathbb{R}^3 , and we triangulate it, and its boundary $\partial\mathbb{M}$ using v vertices, e edges, and t triangles and T tetrahedra, all of which are examples of *simplices*. A vertex is a 0-dimensional simplex, an edge is a 1D simplex, a triangle is a 2D simplex, and a tetrahedron is a 3D simplex (Vegter 1997; Okabe 2000; Rote & Vegter 2006; Zomorodian 2009; Edelsbrunner & Harer 2010; Pranav et al. 2017). The triangulation of $\partial\mathbb{M}$ is made up of a subset of the vertices, edges, and triangles used to triangulate \mathbb{M} , and we denote the numbers of these by v_∂ , e_∂ , and t_∂ .

Formulae going back, essentially, to Euler (1758), define the *Euler characteristics* of \mathbb{M} and $\partial\mathbb{M}$ – traditionally denoted as $\chi(\mathbb{M})$ and $\chi(\partial\mathbb{M})$ – as the alternating sums

$$\chi(\mathbb{M}) = v - e + t - T, \quad \chi(\partial\mathbb{M}) = v_\partial - e_\partial + t_\partial, \quad (21)$$

with similar alternating sums appearing in higher dimensions. It is an important and deep result that the Euler characteristic does not depend on the triangulation.

A more global, but equivalent, definition of the Euler characteristic would be to take $\chi(\mathbb{M})$ to be the number of its connected components, minus the number of its 'holes' (also known as

‘handles’ or ‘tunnels’; regions through which one can poke a finger) plus the number of its enclosed voids (connected, empty regions). For $\partial\mathbb{M}$, or, indeed, any general, connected, closed 2D surface, the Euler characteristic is equal to twice the number of components minus twice the number of tunnels. If the surface is not closed, but has b boundary components, then the number of such components needs to be subtracted from this difference.

The number of holes of a connected, closed surface S can be formalized in terms of its *genus*, $g(S)$. For a connected, orientable surface, the genus is defined, up to a constant factor, as the maximum number of disjoint closed curves that can be drawn on S , so that cutting along them does not leave the surface disconnected. It thus follows that the genus of a surface is closely related to its Euler characteristic, via

$$\chi(S) = 2 - 2g(S). \quad (22)$$

Another result linking the Euler characteristic with the genus is that for 3D regions \mathbb{M} that have smooth, closed manifolds $\partial\mathbb{M}$ as boundary, $\chi(\mathbb{M}) = \frac{1}{2}\chi(\partial\mathbb{M})$. It thus follows from (22) that

$$\chi(\mathbb{M}) = \frac{1}{2}\chi(\partial\mathbb{M}) = 1 - g(\partial\mathbb{M}). \quad (23)$$

Both the genus and the Euler characteristic have been an important focal point of topological studies in cosmology since their introduction in the cosmological setting (Gott et al. 1986; Hamilton et al. 1986). Both have been used extensively in the study of models as well as observational data, with a strong emphasis on the test of the assumption of Gaussianity of the initial phases of matter distribution in the Universe, as well as the large-scale structure at the later epochs. One reason for this is because of the existence of a closed analytical expression for the mean genus and the Euler characteristic of the excursion sets of Gaussian random fields. For excursion sets \mathbb{M}_ν of a Gaussian field at normalized level $\nu = f/\sigma$ (Equation 19), the mean Euler characteristic $\langle\chi(\nu)\rangle$ in a unit volume is given by (Doroshkevich 1970; Adler 1981; Bardeen et al. 1986; Hamilton et al. 1986):

$$\langle\chi(\nu)\rangle = -\frac{\lambda^3}{2\pi^2}(1 - \nu^2)e^{-\nu^2/2}, \quad (24)$$

where λ is proportional to the second-order moment $\langle k^2 \rangle$ of the power spectrum $P(k)$, and thus proportional to the second-order gradient of the autocorrelation function,

$$\lambda^2 = \frac{\langle \|k^2\| \rangle}{3} = \frac{\sigma_1^2}{\sigma^2} = \frac{\int_0^\infty d^3\vec{k} k^2 P(k)}{\int_0^\infty d^3\vec{k} P(k)}, \quad (25)$$

or, in other words, proportional to the second-order gradient of the correlation function,

$$\lambda^2 = -\frac{\xi''(0)}{\xi(0)}. \quad (26)$$

From this expression, we may immediately observe that the Euler characteristics has only a weak sensitivity on the power spectrum of a Gaussian field. It is limited to the overall amplitude, via its second-order moment, while the variation as a function of threshold level ν does not bear any dependence on power spectrum. For the purpose of evaluating the Gaussianity of a field, the Euler characteristic – and related genus – therefore provide a solid testbed. It is one of the reasons why the analytical expression of Equation (24) plays a central role in topological studies of the Megaparsec scale cosmic mass distribution. Nonetheless, the principal reason is that it establishes the reference point for the assessment and comparison of the majority of topological measurements.

Nonetheless, some care should be taken. As we will argue below, when discussing in Section 4 the general context for such geometric measures in terms of the GKF, this expression is valid only under strict conditions on the nature of the manifold \mathbb{M}_ν . The expression is only valid in the case where the superlevel set is a smooth, closed manifold. Additional terms would appear when the boundary $\partial\mathbb{M}_\nu$ of the manifold has edges or corners. For the idealized configurations of the cubic boxes with periodic boundary conditions, such additional terms are not relevant. However, in the real-world setting of cosmological galaxy surveys, selection effects may yield effective survey volumes that suffer a range of artefacts.

The Euler characteristic and Genus have been used extensively in the study of models as well as observational data, with a strong emphasis on the test of the assumption of Gaussianity of the initial phases of matter distribution in the Universe, as well as the large-scale structure at the later epochs.

3.2 Minkowski functionals

Although, as we emphasized in the previous subsection, the Euler characteristic is an essentially topological concept, it also has a role to play in geometry, as one of a number of geometric quantifiers, which include the notions of volume and surface area. There are $D + 1$ such quantifiers for D -dimensional sets, and they go under a number of names, orderings, and normalizations, including, Minkowski functionals, quermassintegrals, Dehn and Steiner functionals, curvature integrals, intrinsic volumes, and Lipschitz–Killing curvatures. Most of the mathematical literature treating them is integral geometric in nature (e.g. Mecke et al. 1994; Schmalzing & Buchert 1997; Sahni et al. 1998; Schmalzing et al. 1999) but they are also often computable via differential geometric techniques, for which Adler & Taylor (2010) is a useful reference for what we need. We need only Minkowski functions Q_j and Lipschitz–Killing curvatures \mathcal{L}_j , which, when both are defined, are related by the fact that

$$Q_j(\mathbb{M}) = j!\omega_j\mathcal{L}_{D-j}(\mathbb{M}), \quad j = 0, \dots, D, \quad (27)$$

and $\omega_k = \pi^{k/2}\Gamma(1 + k/2)$ is the volume of a k -dimensional unit ball ($\omega_0 = 1$, $\omega_1 = 2$, $\omega_2 = \pi$, $\omega_3 = 4\pi/3$). We will invest a little more space on these quantities than actually necessary for this paper, exploiting the opportunity to clarify some inconsistencies in the ways these terms are used in the cosmological and mathematical literatures.

A useful way to define these quantities is via what is known as Steiner’s formula (which is generally quoted in the integral geometric setting of convex sets) or Weyl’s tube formula (in the differential geometric setting of regions bounded by pieces of smooth manifolds, glued together in a ‘reasonable’ fashion). Writing V_D to denote D -dimensional volume, this reads as

$$V_D \left(\left\{ x \in \mathbb{R}^D : \min_{y \in \mathbb{M}} \|x - y\| \leq \rho \right\} \right) = \sum_{j=0}^D \frac{\rho^j}{j!} Q_j(\mathbb{M}) = \sum_{j=0}^D \omega_{D-j} \rho^{D-j} \mathcal{L}_j(\mathbb{M}), \quad (28)$$

where ρ is small, and the set in the left-hand side is known as the tube around \mathbb{M} of radius ρ .

In any dimension, it is trivial (set $\rho = 0$) to check from the definition (28) that Q_0 and \mathcal{L}_D measure D -dimensional volume. It is not a lot harder to see that Q_1 and $2\mathcal{L}_2$ measure surface area. The

other functionals are somewhat harder to define, but it is always true, and a deep result, that

$$\chi(\mathbb{M}) = \mathcal{L}_0(\mathbb{M}) = \frac{1}{D! \omega_D} Q_D(\mathbb{M}). \quad (29)$$

In the 3D case of most interest to us, this leaves only Q_2 and \mathcal{L}_1 to be defined. Integral geometrically, if the manifold \mathbb{M} is convex, $\mathcal{L}_1(\mathbb{M}) = Q_2(\mathbb{M})/2\pi$ is twice the *caliper diameter* of \mathbb{M} . The latter is defined as follows: place \mathbb{M} between two parallel planes (calipers), measure the distance between the planes, and average over all rotations of \mathbb{M} .

A property that will actually be important for us later is the scaling property that, for any $\lambda > 0$,

$$\mathcal{L}_j(\lambda\mathbb{M}) = \mathcal{L}_j(\lambda x : x \in \mathbb{M}) = \lambda^j \mathcal{L}_j(\mathbb{M}). \quad (30)$$

As we already noted, in general all the LKCs can also be calculated via differential geometry and curvature integrals, at least when $\partial\mathbb{M}$ is a smooth *stratified manifold*. These include, for example, cubes, for which the interior of the sides, edges, along with the corners, are all submanifolds of the cube, along with cubes that have been deformed in a smooth manner. In the future, we will assume that \mathbb{M} is a nice stratified manifold. The simplest situation for describing the differential geometric approach to Minkowski functionals occurs when $\partial\mathbb{M}$ is actually a smooth closed, manifold, i.e. non-stratified, and without a boundary. The formulae, for $D = 3$, are then

$$\tilde{Q}_0(\mathbb{M}) = \int_{\mathbb{M}} d^3x, \quad (31)$$

$$\tilde{Q}_1(\mathbb{M}) = \int_{\partial\mathbb{M}} d^2S(x), \quad (32)$$

$$\tilde{Q}_2(\mathbb{M}) = \int_{\partial\mathbb{M}} d^2S(x) (\kappa_1 + \kappa_2), \quad (33)$$

$$\tilde{Q}_3(\mathbb{M}) = 2 \int_{\partial\mathbb{M}} d^2S(x) \kappa_1 \kappa_2, \quad (34)$$

where $\kappa_1(x)$ and $\kappa_2(x)$ are the principal curvatures of $\partial\mathbb{M}$ at the point $x \in \partial\mathbb{M}$, and S is surface measure. Equation (34), known as the Gauss–Bonnet theorem, encapsulates the remarkable fact that a topological characteristic such as the Euler characteristic of a set, which is invariant to bending and stretching, is accessible as the integral of the curvature of its boundary. In Section 4.5, we will relate these formulae to the standard formulae used in cosmology to compute the Minkowski functionals.

There are two very important facts to always remember when using the above four formulae. The first is that different authors often define the Q_j slightly differently, so that factors of 2 and π may appear in front of the integrals. As long as there is consistency within a particular paper, this is of little consequence. Our own choice of constants is dictated by the tube formula of (28) and the simple connection (27) between the Lipschitz–Killing and Minkowski functionals. More important, however, is the fact that the simple expressions in (31)–(34) hold only because of the assumption that the space \mathbb{M} is a smooth, closed, manifold. As we will argue in the discussion in Section 4 on the GKF, in less idealistic circumstances the situation is less straightforward. If the boundary $\partial\mathbb{M}$ has edges or corners then there are additional terms, involving curvature integrals along the edges and angle calculations at the corners. These terms have typically been ignored in the cosmological literature when discussing the mean values of excursion sets, leading to results that

are actually approximations, rather than exact formulae, as they are often presented. This point will be taken up again below, in Section 4, where, while giving exact results, we shall also show why the approximations are well justified.

3.3 Homology and Betti numbers

We now return to purely topological descriptions of sets, in essence breaking up the information encoded in the Euler characteristic to component, and more informative, pieces.

A stratified manifold, which need not be connected, can be composed of a number of objects of different topological natures. For example, in 3D, each of these might be topological balls, or might have tunnels and voids in them. These independent objects, tunnels, and voids are different topological components of a manifold, and have direct relevance to some familiar properties of the cosmic mass distribution. For example, the distribution and statistics of independent components as a function of scale or density threshold is a direct measure of the clustering properties of the mass distribution. The number of tunnels as well as the changes in their connectivity, as a function of scale or density threshold, can be an indicator of percolation properties of the cosmic mass distribution. Similarly, the topological voids have a direct correspondence with the vast near empty regions of cosmic mass distribution called the cosmic voids.

The notions of connectedness, tunnels, and voids, along with their extensions to higher dimension, have formal definitions through the notion of homology (see e.g. Munkres 1984). They are associated with the p -dimensional *cycles* of a d -dimensional manifold ($p = 0 \dots d$). In dimension 3, a 0-cycle corresponds to a connected object, a 1-cycle to a loop enclosing a tunnel, and a 2-cycle to a shell enclosing a void. In general, when properly formulated, a k -cycle in an object of dimension greater than k corresponds to the k -dimensional boundary of a $(k + 1)$ dimensional void.

Not all these cycles are independent. For example, one can draw many loops around a cylinder, all of which are topologically equivalent. The collection of all p -dimensional cycles is the p -th homology group \mathbb{H}_p of the manifold, and the rank of this group is the collection of all *linearly independent* cycles. The rank is denoted by the *Betti numbers* β_p , where $p = 0, \dots, d$ (Betti 1871). In dimension 3, the three Betti numbers have simple, intuitive meanings: β_0 counts the number of independent components, β_1 counts the number of loops enclosing the independent tunnels, and β_2 counts the number of shells enclosing the independent voids.

A more mathematically rigorous definition of these concepts can be found in the traditional literature of homology (e.g. Munkres 1984). For more details, in an intuitive and cosmological setting, see van de Weygaert et al. (2011) and Pranav et al. (2017).

3.3.1 Betti numbers and Euler characteristic

Like the Euler characteristic, the Betti numbers are topological invariants of a manifold, meaning that they do not change under systematic transformations under rotation, translation, and deformation. Their relationship to the Euler characteristic is given by the following formula, which is an algebraic topological version of the original Euler–Poincaré Formula, in which the summands were numbers of simplices of varying dimension in a triangulation.

$$\chi = \beta_0 - \beta_1 + \beta_2 - \dots + (-1)^d \beta_d. \quad (35)$$

Yet, even the Betti numbers do not determine a manifold completely. Two topologically inequivalent manifolds may have equal Betti

numbers. One implication of this is that the set of d Betti numbers contain more topological information than is contained in the Euler characteristic. Hence, two manifolds may have the same Euler characteristic, yet be topologically distinctly different in terms of their Betti numbers. In the context of Gaussian random fields we will see that this finds its expression of power spectrum sensitivity: while the variation of the Euler characteristic as a function of density threshold of a superlevel set is independent of power spectrum, we find distinct sensitivities of Betti numbers on the power spectrum (see Section 7 and Park et al. 2013).

3.3.2 Meatball-like, Swiss-cheeselike, and Sponge-like topologies

The description of topology through connected components, tunnels, and voids has parallels in the earlier works related to the topological studies of cosmic mass distribution. Gott et al. (1986) introduced the terms *Meatball-like* and *Swiss-cheeselike* topologies to describe the dominance of either *islands* – connected components – and *voids*. As is apparent from the terms, *Meatball-like* topology refers to sets dominated by mainly isolated objects. Opposite to this are the *Swiss-cheeselike* topologies denoting a manifold composed of a single or a few components with the presence of fully enclosed cavities much like the inside of cheese. In other words, while a pattern with *Meatball-like* topology resembles that of black polka dots on a white background, the *Swiss-cheeselike* topology is that of white polka dots on a dark background (see Gott et al. 1986). These terminologies are intuitively meaningful, and present a clear picture in the mind of the reader. Formally, however, they are no more than a colourful way of indicating the dominant Betti number. Nevertheless, we will borrow these terms from Gott et al. (1986) to augment intuitive understanding for the reader.

The topological *Meatball-like* and *Swiss-cheeselike* configurations are characteristic for two extreme outcomes of different cosmological structure formation scenarios. The *Meatball-like* topology would involve the formation of high-density islands – dependent on scale galaxy haloes, clusters, or superclusters – in a low-density ocean. It was supposed to be the typical outcome of bottom-up hierarchical formation scenarios such as Cold Dark Matter cosmologies. The *Swiss-cheeselike* topologies were more characteristic of the top-down formation scenarios, which produce a texture in which low-density or empty void regions appear to be carved out on an otherwise higher density background. This would be the result of a formation scenario in which primordial perturbations over a narrow range of scales would assume a dominant role, manifesting itself with voids would occupy most of space (see e.g. van de Weygaert 2002).

Gott et al. (1986) and subsequent studies of the genus or Euler characteristic of the cosmic matter and galaxy distribution claimed that its topology is only manifestly *Meatball-like* at high-density thresholds, and *Swiss-cheeselike* at very low-density thresholds, while it is characteristically *Sponge-like* at the median density level. A *Sponge-like* topology points to a set with a percolating structure, which signifies the presence of a single or a few connected components, each marked by the presence of tunnels that percolate the structure. In this phase, tunnels are the dominant topological features. Strictly speaking, and usually interpreted as such in cosmology (see e.g. Gott et al. 1986, 2008), a sponge-like topology means that at median density level (which for the symmetric Gaussian fields corresponds to the mean density level $\nu = 0$), at which high- and low-density regions each take up 50 per cent of the volume, the high-density regions form one multiply connected

region while the low-density regions also form one connected region that is interlocking with the high-density region (Gott et al. 2008). In other words, in a pure *Sponge-like* topology there is only one underdense void region and only one overdense region, each of these evidently characterized by an irregular and indented surface and by numerous percolating alleys or tunnels. In other words, these claims suggest that *Sponge-like* topologies correspond to one where the Betti numbers $\beta_0 = 1$ and $\beta_1 = 1$ at the median density. We will soon see that the reality is slightly more complex.

For a visual appreciation of the different topological identities, Figure 1 presents the isodensity surfaces of a simulated Gaussian random field over a cubic region for three different density thresholds $\nu = \sqrt{3}$, 1, 0, and for two different Gaussian fields with a power-law power spectrum, namely the $n = 1$ and the $n = -2$ models. The left-hand column presents the contour surfaces for the $n = 1$ model, the right-hand column the contour surfaces for the $n = -2$ model. By means of enclosing translucent spheres we highlight a typical tunnel, and we highlight isolated objects by means of an enclosing green translucent sphere. The visualizations in Figure 1 immediately reveal the considerable contrast in topology between the different Gaussian field realizations, most evidently when assessed at around the mean density level $\nu = 0$. While both are *Sponge-like* at around this threshold, we do note some stark differences. For the $n = 1$ model, the topology is predominantly sponge-like, with a dominant presence of short loops, most of which are like indentations of a single, large connected surface. By contrast the topology of the $n = -2$ model is a visible mixture of loops and as well as isolated islands. In general, the overall topology consists of a mixture of the various topological components, with different mixing fractions for Gaussian fields with different power spectra.

It is at this point that we may appreciate the increased information content of Betti numbers, as opposed to the more limited topological characterization by the Euler characteristic or genus only. In the context of homology, we can directly relate terms like *Meatball-like*, *Swiss-cheeselike*, or *Sponge-like* topology to a more quantitative characterization in terms of the relative values of β_0 , β_1 and β_2 . The situation where the β_0 assumes the vast share of the topological signal is the *Meatball-like* topology of Gott et al. (1986). The opposite situation of a dominant β_2 signal is that of the *Swiss-cheeselike* topology, while a *Sponge-like* topology corresponds to the entire field divided into a low number of overdense and underdense regions, and thus low values for β_0 and β_2 , always in combination with a large value for β_1 , corresponding to the tunnels and loops that form indentations of these connected regions.

We refer to Section 7 for a considerably more quantitative evaluation of the relative contributions of topological features in terms of the corresponding Betti numbers β_0 , β_1 , and β_2 .

4 THE GAUSSIAN KINEMATIC FORMULA

As mentioned above, one of the main reasons that the Euler characteristic, genus, and the Minkowski functionals have played such a useful role in cosmology is that there are exact, analytic, formulae for their expected values, when the characteristics that are being computed are generated by the superlevel sets of Gaussian random fields. These formulae are old, going back to Doroshkevich (1970) for a simple 2D case, with the cosmological literature generally relying mainly on Adler (1981) and Bardeen et al. (1986) for full results. Over the last decade or so, major extensions of these formulae have been developed, going under the name of the *Gaussian kinematic formula*, or, hereafter, *GKF*. The GKF, in one compact formulae, gives the expected values of the Euler charac-

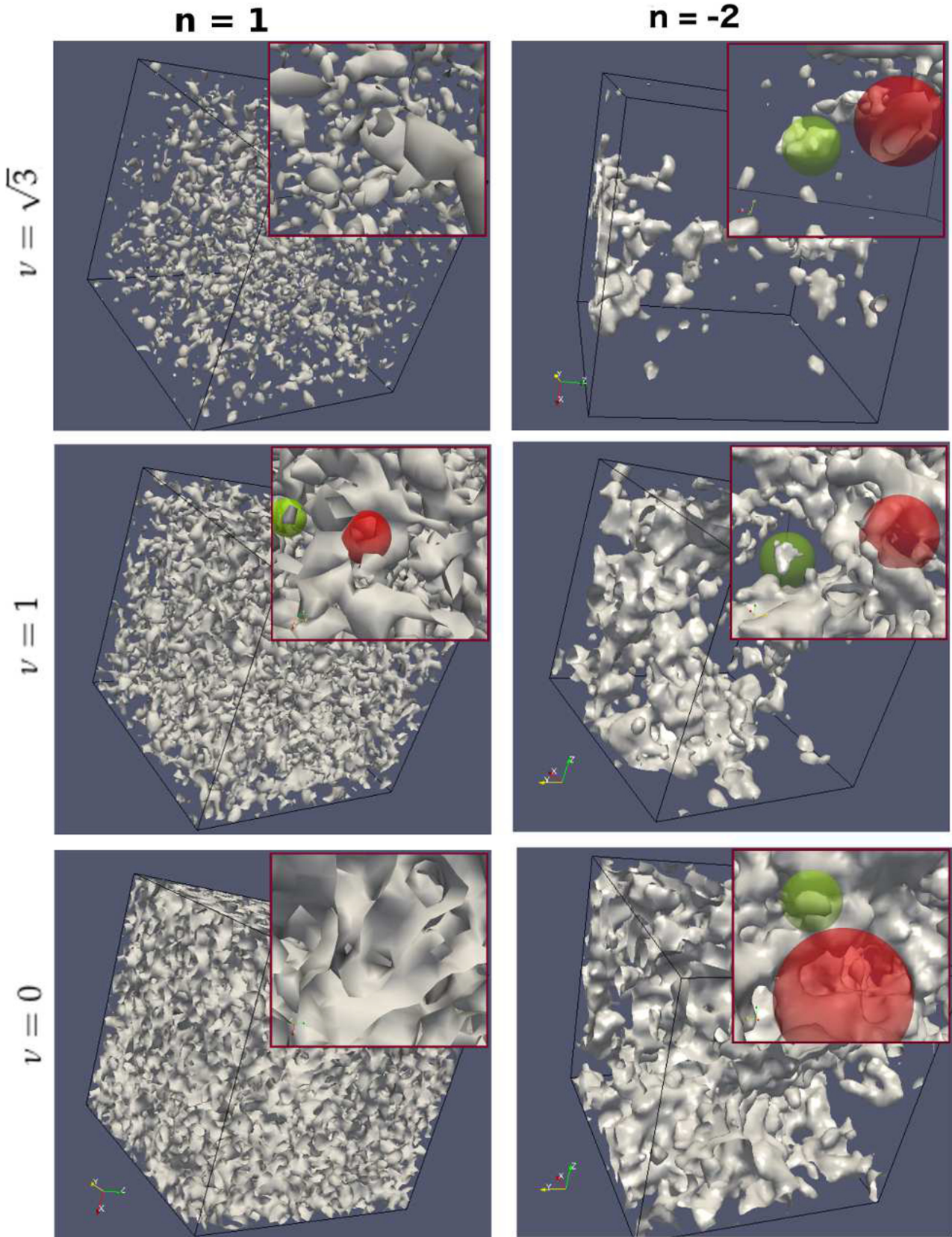


Figure 1. Isodensity surfaces denoting the structure of the field for three different density thresholds $v = \sqrt{3}$, 1, and 0, for the $n = 1$ and the $n = -2$ models. The left-hand column presents the isodensity surfaces for the $n = 1$ model and the right-hand column presents the contour surfaces for the $n = -2$ model. Examples of typical tunnels are enclosed in translucent red spheres; examples of typical isolated islands are enclosed in green spheres. The topology of the contour surfaces shows a dependence on the choice of the power spectrum, as well as the density threshold.

teristic (and so genus), all the Lipschitz–Killing curvatures (and so Minkowski functionals) described earlier as well as extensions of them, for the superlevel sets (and their generalizations in vector-valued cases) of a wide class of random fields, both Gaussian and only related somehow to Gaussian, and both homogeneous and non-homogeneous. The parameter sets of these random fields are also very general, and cover all examples required in cosmology, without any need to ignore boundary effects.

We do not actually use the GKF in this paper, since later on we shall be more concerned with Betti numbers than Euler characteristics or Minkowski functionals, and, unfortunately, these are not covered by the GKF. In fact, for reasons we shall explain later, there is no detailed statistical theory for them, which is why this paper is mainly computational. Nevertheless, since most of the literature around the GKF is highly technical differential topology, we take this opportunity to discuss the GKF in a language that should be more natural for cosmology. Our basic references are Adler & Taylor (2010) for all the details, and Adler & Taylor (2011) and Adler et al. (2018) for less detailed, but more user-friendly, treatments.

4.1 The GKF

The first component of the GKF is a D -dimensional parameter space \mathbb{M} , which is taken to be a C^2 Whitney stratified manifold. As mentioned earlier, this is a set made out of glued together pieces, each one of which is a submanifold of \mathbb{M} , along with rules about how to glue the pieces together. We group all the k -dimensional submanifolds together, and write the collection as $\partial\mathbb{M}_k$, $k = 0, \dots, D$. For example, if \mathbb{M} is a 3D cube, then $\partial\mathbb{M}_3$ is the interior of the cube, $\partial\mathbb{M}_2$ contains the interiors of its six sides, $\partial\mathbb{M}_1$ collects the interiors of the eight edges, and $\partial\mathbb{M}_0$ is the collection of the eight vertices. In general, we write

$$\mathbb{M} = \bigsqcup_{k=0}^D \partial\mathbb{M}_k, \quad (36)$$

where the union is of disjoint sets. The parameter space \mathbb{M} could be a subset of a Euclidean space, or a general, abstract, stratified manifold. To the best of our knowledge, the Euclidean setting is (so far) the only one used in cosmology.

The second component of the GKF is a twice differentiable, constant mean, Gaussian random field, $f : \mathbb{M} \rightarrow \mathbb{R}$, with constant variance. There is no requirement of stationarity or isotropy, only of constant mean and variance. For convenience, we take these to be 0 and 1, respectively. Changing them in the formulae to follow involves nothing more than addition, or multiplication, by constants. An extension of the second component, which is crucial for getting away from the purely Gaussian setting, is to take $d \geq 1$ independent copies, f_1, \dots, f_d of f , and we write $\vec{f} = (f_1, \dots, f_d)$ for the vector-valued random field made up of these as components.

The third, and final, component is a set $\mathcal{H} \subset \mathbb{R}^d$, called a *hitting set*. In most of the cases of interest to cosmology, $d = 1$ and $\mathcal{H} = [v, \infty)$ for some v .

The aim of the GKF is to give a formula for the expectations of geometric and topological measures of the *excursion sets*

$$A_{\mathcal{H}} \equiv A_{\mathcal{H}}(\vec{f}, \mathbb{M}) = \{x \in \mathbb{M} : \vec{f}(x) \in \mathcal{H}\}. \quad (37)$$

In the particular case that $d = 1$, so that f is real-valued, and \mathcal{H} is the set $[v, \infty)$, we are looking at super level sets of f , and write

$$A_v \equiv A_u(\vec{f}, \mathbb{M}) = \{x \in \mathbb{M} : f(x) \geq v\}. \quad (38)$$

In order to formulate the GKF, we need to revisit one definition and add an additional one. Recall the Lipschitz–Killing curvatures of (28), which, together with the Minkowski functionals, we chose to define via a tube volume formula. This definition is adequate for a Euclidean set, but the most general version of the GKF works on abstract stratified manifolds. In that case the most natural definition of the Lipschitz–Killing curvatures is not via a tube formula, but rather via curvature integrals akin to Equations (31)–(34). These curvatures will now involve the Riemannian curvatures and second fundamental forms of all the submanifolds in all the $\partial\mathbb{M}_k$, and the Riemannian metric underlying all these turns out to be one related to the covariance function of the random field. All of this is beyond the scope of this paper. Nevertheless, although we shall concentrate on stationary random fields on subsets of Euclidean spaces, for which the decomposition (Equation 36) will still be relevant, for the remainder of this paper, it is worthwhile remembering that this is but a small part of a much larger theory.

The remaining definition is of a Minkowski-like functional which, instead of measuring the size of objects, measures their (Gaussian) probability content. To define it, let \vec{X} be a vector of d independent, identically distributed, standard Gaussian random variables, and, for a nice subset (e.g. locally convex, stratified manifold) $\mathcal{H} \subset \mathbb{R}^d$, and sufficiently small $\rho > 0$, consider the Taylor series expansion

$$\Pr \left\{ X \in \left\{ x \in \mathbb{R}^d : \min_{y \in \mathcal{H}} \|y - x\| \right\} \leq \rho \right\} = \sum_{j=0}^{\infty} \frac{\rho^j}{j!} \mathcal{M}_j^d(\mathcal{H}). \quad (39)$$

The coefficients, $\mathcal{M}_j^d(\mathcal{H})$, in this expansion, due to Taylor (2006), are known as the *Gaussian Minkowski functionals* of \mathcal{H} , and play a similar role to the usual Minkowski functionals, with the exception that all measurements of size are now weighted with respect to probability content.

In dimension $d = 1$, with $\mathcal{H} = [v, \infty)$, the $\mathcal{M}_j^1(\mathcal{H})$ take a particularly simple form, and it is easy to check from a Taylor expansion of the Gaussian density that

$$\mathcal{M}_j^1([v, \infty)) = H_{j-1}(v) \frac{e^{-v^2/2}}{\sqrt{2\pi}}, \quad (40)$$

where, for $n \geq 0$, H_n is the n -th Hermite polynomial,

$$H_n(x) = n! \sum_{j=0}^{\lfloor n/2 \rfloor} \frac{(-1)^j x^{n-2j}}{j!(n-2j)!2^j},$$

and, for $n = -1$, we set

$$H_{-1}(x) = \sqrt{2\pi} e^{x^2/2} \Psi(x). \quad (41)$$

where

$$\Psi(x) = \frac{1}{\sqrt{2\pi}} \int_u^{\infty} e^{-x^2/2} dx \quad (42)$$

is the Gaussian tail probability.

We now have all we need to define the GKF, which is the result that, under all the conditions above, and some minor technical conditions for which Adler & Taylor (2010) is the best reference,

$$\langle \mathcal{L}_i(A_{\mathcal{H}}(f, \mathbb{M})) \rangle = \sum_{j=0}^{D-i} \begin{bmatrix} i+j \\ j \end{bmatrix} (2\pi)^{-j/2} \mathcal{L}_{i+j}(\mathbb{M}) \mathcal{M}_j^d(\mathcal{H}), \quad (43)$$

where the combinatorial ‘flag coefficients’ are defined by

$$\begin{bmatrix} n \\ j \end{bmatrix} = \binom{n}{j} \frac{\omega_n}{\omega_{n-j} \omega_j}, \quad (44)$$

where ω_m is the volume of the unit ball in \mathbb{R}^m :

$$\omega_m = \frac{\pi^{m/2}}{\Gamma(\frac{m}{2} + 1)}, \quad (45)$$

i.e. $\omega_1 = 2$, $\omega_2 = \pi$, and $\omega_3 = 4\pi/3$. (Note that all \mathcal{L}_j for $j > D$ are defined to be identically zero, so that the highest order Lipschitz–Killing curvature in Equation 43 is always $\mathcal{L}_D(\mathbb{M})$.)

All this is very general. The parameter space \mathbb{M} might be an abstract stratified manifold, and the Lipschitz–Killing curvatures on both sides of the GKF might be Riemannian curvature integrals. On the other hand, the Gaussian Minkowski functionals are independent of the structure of the random field, and dependent only on the structure of the hitting set \mathcal{H} . To see how this result works in simpler cases, we look at some more concrete examples.

4.2 Examples: rectangles, cubes, and spheres

To start, we will take f to be a mean zero Gaussian random field on D -dimensional Euclidean space and allow a little more generality, with possibly general variance

$$\langle f^2(x) \rangle = \sigma^2. \quad (46)$$

To make the formulae tidier, we will also assume that f has a mild form of isotropy, in that the covariance between two partial derivatives of f , in directions \vec{v}_1 and \vec{v}_2 , is equal to $\lambda^2(\vec{v}_1 \cdot \vec{v}_2)$; viz., it is proportional to the usual Euclidean product of the directions. This will be the case, for example, if f is homogeneous and covariance function has a Taylor series expansion at the origin of the form

$$\xi(x) = \sigma^2 - \frac{1}{2}\lambda^2\sigma^2\|x\|^2 + o(\|x\|^2). \quad (47)$$

Isotropy implies this, but we are actually assuming far less. This requirement implies that λ^2 is the variance of any partial derivative of f , and that this variance is independent of the direction in which the derivative is taken. In the homogeneous, isotropic case (see Equation 25 for the specific 3D case),

$$\lambda^2\sigma^2 = -\frac{1}{D} \sum_{j=1}^D \left. \frac{\partial^2 \xi(x)}{\partial x_j^2} \right|_{x=0} = \frac{\langle \|\vec{k}\|^2 \rangle}{D} \xi(0), \quad (48)$$

where the partial derivative can be taken in any of the D directions. Thus λ^2 can be found directly from the covariance function or, equivalently, as the second spectral moment.

For our first example, let \mathbb{M} be the D -dimensional rectangle $\mathbb{M}_{\text{Rec}} = \prod_{j=1}^D [0, m_j]$. The usual, Euclidean, Lipschitz–Killing curvatures of \mathbb{M} will then be

$$\mathcal{L}_j^E(\mathbb{M}_{\text{Rec}}) = \sum m_{i_1} \cdots m_{i_j}, \quad (49)$$

where the sum is taken over the $\binom{D}{j}$ different choices of subscripts i_1, \dots, i_j , and the additional superscript E is to emphasize the Euclidean nature of the Lipschitz–Killing curvatures. The corresponding Minkowski functionals are just products of reordered Lipschitz–Killing curvatures, as in Equation (27). The Riemannian Lipschitz–Killing curvatures needed for substitution in the GKF are then given by

$$\mathcal{L}_j(\mathbb{M}_{\text{Rec}}) = \lambda^j \mathcal{L}_j^E(\mathbb{M}_{\text{Rec}}). \quad (50)$$

Let \mathcal{O}_k denote the collection of all $\binom{D}{k}$ k -dimensional faces of \mathbb{M}_{Rec} which include the origin. The k -dimensional volume of a face $J \in \mathcal{O}_k$ is written as $|J|$. Then replacing the Riemannian Lipschitz–Killing curvatures in the GKF by the Euclidean ones, for this case

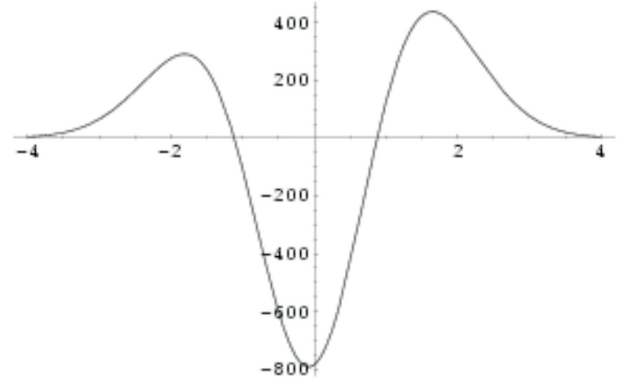


Figure 2. A mean Euler characteristic curve for a Gaussian field over a 3D cube of limited size. Notice the substantial difference with the conventionally known and expected symmetric curve (see Equation 29). The latter forms the asymptotic situation for a very large sample size T and a relatively ‘quiet’ field f within that volume. In a cosmological context this means that the symmetric curve can only be used as a reference for a cosmic volume that is sufficiently large and represents a fair sample of the cosmic mass distribution (see the text for details).

the GKF reads as follows.

$$\begin{aligned} \langle \mathcal{L}_i^E(A_\nu) \rangle &= e^{-\nu^2/2\sigma^2} \sum_{j=0}^{D-i} \binom{i+j}{j} \frac{\lambda^j}{(2\pi)^{(j+1)/2}} H_{j-1} \left(\frac{\nu}{\sigma} \right) \mathcal{L}_{i+j}^E(\mathbb{M}). \end{aligned} \quad (51)$$

It is easy to rewrite this in terms of Minkowski functionals, when it becomes the slightly less elegant formula

$$\begin{aligned} \langle Q_i(A_\nu) \rangle &= e^{-\nu^2/2\sigma^2} \sum_{j=0}^i \binom{D+j-i}{j} \binom{i}{j} \frac{\omega_j j! \lambda^j}{(2\pi)^{(j+1)/2}} H_{j-1} \left(\frac{\nu}{\sigma} \right) Q_{i-j}(\mathbb{M}). \end{aligned} \quad (52)$$

To get a better feel for this Equation, let us look the mean value of the Euler characteristic $\langle \chi(\mathbb{M}) \rangle$, i.e. of the zeroth Lipschitz–Killing curvature $\mathcal{L}_0(\mathbb{M})\mathbb{R}$, in the cases $D = 2$ and $D = 3$, taking \mathbb{M} to be a square or cube of side length T , and setting $\sigma^2 = 1$ for simplicity. In the 2D case, we obtain

$$\langle \chi(A_\nu) \rangle = \left[\frac{T^2 \lambda^2}{(2\pi)^{3/2}} \nu + \frac{2T\lambda}{2\pi} \right] e^{-\frac{\nu^2}{2}} + \Psi(\nu). \quad (53)$$

In 3D, for the mean Euler characteristic (Equation 51) yields, again for $\sigma^2 = 1$,

$$\langle \chi(A_\nu) \rangle = \left[\frac{T^3 \lambda^3}{(2\pi)^2} (\nu^2 - 1) + \frac{3T^2 \lambda^2}{(2\pi)^{3/2}} \nu + \frac{3T\lambda}{2\pi} \right] e^{-\frac{\nu^2}{2}} + \Psi(\nu). \quad (54)$$

Figure 2 gives an example, over the unit cube, with $\lambda = 880$ (see Equation 48). It is clear that the Euler characteristic curve in Figure 2 differs substantially from the more conventionally known symmetric curve specified by Equation (24). As may be inferred from Equation (54), the symmetric curve only represents a sufficiently valid asymptotic limit if the sample size T is large and the field within this volume is relatively ‘quiet’. In a cosmological context this means that the symmetric curve can only be used as reference for a cosmic volume that is sufficiently large and represents a fair sample of the cosmic mass distribution. This is still a relatively unknown fact in cosmological applications.

Similar expressions as Equation (54) hold for the mean values of all the Lipschitz–Killing curvatures and Minkowski functionals of excursion sets.

There is an important point that one should note about these formulae, which, while obvious in the simplest cases such as in Equation (51) are actually general phenomena. All of these formulae contain obvious, or sometimes hidden, power series expansions. In the simple case of Equation (51) there are three such series. The most obvious one is in the size of the cube, as expressed through the side length T . If T is large, then the first term, in T^3 , is dominant. The opposite is true if T is small. Overall, one can, correctly, relate to the coefficients of the powers of T as expressions affected by the behaviour of f in the interior of \mathbb{M} , then on its boundary, and so forth. There is also an expansion in the second spectral moment, λ^2 . The larger this moment, the rougher will be the field f , and this will lead to large Lipschitz–Killing curvatures and Minkowski functionals. In the case of the general GKF (43) in which the Lipschitz–Killing curvatures are all Riemannian quantities, the measurements of the various ‘sizes’ of \mathbb{M} involve a delicate combination of both the ‘physical’ size and shape of \mathbb{M} , along with the roughness of f in different regions. Nevertheless, the same general interpretation of these expansions still holds. The final expansion is in the height parameter ν . Clearly, as ν becomes large, the first term in the GKF – the one associated with the volume \mathcal{L}_D – is the dominant one.

The last two paragraphs are important for applications of the GKF. For example, while the formulae of this subsection will look vaguely familiar to integral geometers, they probably look unusually complicated to a reader familiar only with the cosmology literature. We will explain the differences in Section 4.5, but first briefly mention how to use the GKF for non-Gaussian random fields.

4.3 Gaussian related random fields and the GKF

Although the GKF is about Gaussian random fields, the way it is formulated, in terms of vector values fields and the general hitting set \mathcal{H} , allows it to also treat a certain class of non-Gaussian random fields as well. The class, while somewhat limited, turns out to be broad enough to cover many, if not most, statistical applications of random fields.

To be more precise, we shall call a random field $g : \mathbb{M} \rightarrow \mathbb{R}^d$ a *Gaussian related*, \mathbb{R}^d -valued, random field if we can find a vector-valued Gaussian random field, $\vec{f} : \mathbb{M} \rightarrow \mathbb{R}^D$, satisfying all the conditions of the GKF, and a function $F : \mathbb{R}^D \rightarrow \mathbb{R}^d$, such that \vec{g} has the same multivariate distributions as $F(\vec{f})$.

In the trivial case that $D = 1$, or, in general $D = d$ and F is invertible, then the corresponding Gaussian related process is not much harder to study than the original Gaussian one, since what happens at the level u for \vec{f} is precisely what happens at the uniquely defined level $F^{-1}(u)$ for \vec{g} . In the more interesting cases in which F is not invertible, $\vec{g} = F(\vec{f})$ can provide a process that is qualitatively different to \vec{f} . Three useful examples are given by the following three choices for F , where in the third we set $D = n + m$.

$$\sum_1^D x_i^2, \quad \frac{x_1 \sqrt{D-1}}{(\sum_2^D x_i^2)^{1/2}}, \quad \frac{m \sum_1^n x_i^2}{n \sum_{n+1}^{n+m} x_i^2}. \quad (55)$$

The corresponding random fields are known as χ^2 fields with D degrees of freedom, the T field with $D - 1$ degrees of freedom, and the F field with n and m degrees of freedom. These three random fields all have very different spatial behaviour, and each is as fundamental to the statistical applications of random field theory. In note of these three cases, as in general for a Gaussian related

random field, there is no simple point-wise transformation which will transform it to a real-valued Gaussian field.

Note that for a Gaussian-related field \vec{g} the excursion sets $A_{\mathcal{H}}$ can be rewritten as

$$A_{\mathcal{H}}(\vec{g}, \mathbb{M}) = A_{\mathcal{H}}(F(\vec{f}), \mathbb{M}) = A_{F^{-1}(\mathcal{H})}(\vec{f}, \mathbb{M}).$$

Thus, for example, the excursion set of a *real-valued* non-Gaussian $g = F(\vec{f})$ above a level u is equivalent to the excursion set for a *vector-valued* Gaussian \vec{f} in $F^{-1}([u, \infty)) \in \mathbb{R}^D$. Consequently, as long as F is smooth enough, expressions for the mean Lipschitz–Killing curvatures of \vec{g} follow immediately from the GKF, once one knows how to compute the corresponding Gaussian Minkowski functionals. This can be easy or hard depending on the form of F . Examples are given in Adler & Taylor (2010, 2011) and Adler et al. (2018).

4.4 Non-homogeneity

Before turning to the connections between the GKF and related geometric results in the cosmology literature, we add a brief comment about computing the Lipschitz–Killing curvatures in the non-homogeneous setting. As mentioned above, the Lipschitz–Killing curvatures, in general, implicitly incorporate information on the variance structure of the random field f . To see how this works, take \mathbb{M} to be a subset of \mathbb{R}^D , retain the assumptions of zero mean and constant unit variance, and write the (two-parameter) covariance function of f as

$$\xi(x, y) = \langle f(x)f(y) \rangle. \quad (56)$$

Define a matrix-valued function $\Lambda(x) = (\lambda_{ij}(x))_{i,j=1,\dots,D}$ of second-order spectral moments by

$$\lambda_{ij}(x) = \langle k_i k_j \rangle = - \frac{1}{\xi(0)} \left. \frac{\partial^2 \xi(x)}{\partial x_i \partial x_j} \right|_{x=0}. \quad (57)$$

In terms of the previous notation for the isotropic case, with second spectral moment λ^2 , we have $\lambda^2 = \lambda_{ii}(x)$, independent of i and x , and $\lambda_{ij} \equiv 0$ when $i \neq j$. In the homogeneous, but non-isotropic, case, the matrices $\Lambda(x)$ may be a general covariance matrix, but will be independent of x .

It turns out that this is all that one needs to compute the leading Lipschitz–Killing curvature in the general case, where we have

$$\mathcal{L}_D = \int_{\mathbb{M}} \sqrt{\det(\Lambda(x))} dx. \quad (58)$$

If \mathbb{M} has a smooth boundary, then the next Lipschitz–Killing curvature can be calculated as a surface integral of a (Riemannian) curvature function, although the integrating measure is a little complicated. An easy case is that of 2D \mathbb{M} , in which case if we first parametrize $\partial\mathbb{M}$ by a C^2 function $\gamma : [0, 1] \rightarrow \mathbb{R}^2$, we have

$$\mathcal{L}_1 = \frac{1}{2} \int_0^1 \sqrt{\left(\frac{d\gamma(t)}{dt} \right)^T \Lambda(\gamma(t)) \frac{d\gamma(t)}{dt}} dt. \quad (59)$$

For full details of the general case see Adler & Taylor (2010), and some specific worked cases in Adler, Subag & Taylor (2012); Adler et al. (2018).

In many cases, it is possible to avoid analytic computation of the Lipschitz–Killing curvatures, and simply estimate them from data. Differing approaches to this can be found in Adler et al. (2017); Schwartzman et al. (); Taylor & Worsley (2007).

4.5 Cosmology: approximations and boundaries

For the reader familiar with the cosmological literature on mean Euler characteristics and mean Minkowski functionals, much of the discussion will probably seem unfamiliar and perhaps unnecessarily complicated. There are three reasons for this. The first is that cosmology has typically worked under assumptions of homogeneity and isotropy, and we have already seen that in this case the Lipschitz–Killing curvatures are considerably simpler than in the general case. The second reason lies in the fact that there are only two main examples in cosmology: the 2D sphere, for CMB studies, and subsets of \mathbb{R}^3 , for the Megaparsec galaxy and matter density studies. Under the restrictions of homogeneity and isotropy for these two cases, a general theory seems superfluous.

The third reason, however, is not so obvious, and is relevant to both of these parameter spaces. The fact is that the CMB is *not* observed over the full sky, typically as a result of interference from bright foreground objects, such as our own galactic disc and bright point sources. Thus the parameter space \mathbb{M} in these cases is an, often complicated, subset of the sphere, with a convoluted boundary. Similarly, the data on the large-scale galaxy and matter density are estimable only over sectors of the 3D universe that have been covered by observational surveys. Nearly without exception these are limited in terms of sky coverage and include objects only out to a certain distance. Also, they tend to suffer from incompleteness, and usually involve similar foreground issues such as the obscuration by the gas and dust in the disc of our own Galaxy along the zone of avoidance. In this case, \mathbb{M} is a compact 3D region with a complicated boundary and which, in fact, may not even be connected.

In other words, the boundary terms, which even in the homogeneous, isotropic case, make the GKF so complicated, cannot be ignored in exact computations. A simple way out of this conundrum is to replace all the measures described above with dimensionless, ‘normalized’ measures. For example, rather than computing the total Euler characteristic $\chi(A_\nu(f, \mathbb{M}))$ of a superlevel set, one works with $|\mathbb{M}|^{-1}\chi(A_\nu(f, \mathbb{M}))$, where $\mathcal{L}_D(\mathbb{M}) = |\mathbb{M}|$ is the volume, or surface area, of \mathbb{M} , giving a ‘per unit volume’ notion of Euler characteristic. The effect of this normalization on the GKF is minimal. All terms, on both the right and left of the GKF, are similarly normalized. Working then on the implicit assumption that $\mathcal{L}_D(\mathbb{M})/\mathcal{L}_j(\mathbb{M})$ is small for large \mathbb{M} , the GKF of Equation (43) leads to the approximation

$$\left\langle \frac{1}{|\mathbb{M}|} \mathcal{L}_i(A_{\mathcal{H}}(f, \mathbb{M})) \right\rangle \approx \left[\begin{matrix} D \\ i \end{matrix} \right] (2\pi)^{-(D-i)/2} \mathcal{M}_{D-i}^d(\mathcal{H}), \quad (60)$$

while the simpler, Euclidean examples (51) and (52), in which f is real valued, become

$$\left\langle \frac{1}{|\mathbb{M}|} \mathcal{L}_i^E(A_\nu) \right\rangle \approx e^{-\nu^2/2\sigma^2} \left[\begin{matrix} D \\ i \end{matrix} \right] \frac{\lambda^{D-i}}{(2\pi)^{(D-i+1)/2}} H_{D-i-1} \left(\frac{\nu}{\sigma} \right) \quad (61)$$

and

$$\left\langle \frac{1}{|\mathbb{M}|} \mathcal{Q}_i(A_\nu) \right\rangle \approx e^{-\nu^2/2\sigma^2} \left[\begin{matrix} D \\ i \end{matrix} \right] \frac{\omega_i! \lambda^i}{(2\pi)^{(i+1)/2}} H_{i-1} \left(\frac{\nu}{\sigma} \right). \quad (62)$$

Up to unimportant factors of 2 and π due to slightly different definitions of the Minkowski functionals, the last of these approximations is equivalent to the formulae given as exact Equations in, for example, Tomita (1993) and Schmalzing & Buchert (1997), following a tradition of ignoring the contributions of boundary effects going back at least half a century, to Doroshkevich (1970).

Under the – key – assumption that the space \mathbb{M} on which the Minkowski functionals are measured is a smooth, closed, manifold, their expected values for Gaussian random fields, obtained from the evaluation of (31)–(34), are given by rather straightforward

analytical expressions. These then coincide with the expected values of the Minkowski functionals \tilde{Q}_m per unit volume for 3D manifolds \mathbb{M} defined as the excursion sets at normalized field levels $\nu = f\sigma$, found by Tomita (1993) and Schmalzing & Buchert (1997):

$$\langle \tilde{Q}_0(\nu) \rangle = \frac{1}{2} - \frac{1}{2} \Phi \left(\frac{1}{\sqrt{2}} \nu \right), \quad (63)$$

$$\langle \tilde{Q}_1(\nu) \rangle = \frac{\lambda}{3\pi} \exp \left(-\frac{1}{2} \nu^2 \right), \quad (64)$$

$$\langle \tilde{Q}_2(\nu) \rangle = \frac{2}{3} \frac{\lambda^2}{(2\pi)^{3/2}} \nu \exp \left(-\frac{1}{2} \nu^2 \right), \quad (65)$$

$$\langle \tilde{Q}_3(\nu) \rangle = \frac{\lambda^3}{4\pi^2} (\nu^2 - 1) \exp \left(-\frac{1}{2} \nu^2 \right), \quad (66)$$

where $\lambda^2 = -\xi''(0)/\xi(0)$, as defined in Equation (26), and

$$\Phi(x) = \int_0^x dt e^{-t^2} \quad (67)$$

is the standard error function. These Equations are equivalent to Equations (31)–(34).

4.6 On mean Betti numbers

Returning now to the main theme of this paper, which revolves around purely topological concepts such as homology and associated quantifiers such as Betti numbers, the question that arises naturally is whether or not there is a parallel to the GKF, which, with the exception of the Euler characteristic, is about geometric quantifiers, for Betti numbers.

Unfortunately, to date the answer is mainly negative, and all indications are that it will remain that way for a while (see e.g. Wintraecken & Vegter 2013). While there are some high level, asymptotic as $\nu \rightarrow \infty$ results about the Betti numbers of excursion sets of Gaussian excursion sets in the mathematical literature, these are a consequence of the simple structure of Gaussian fields at these levels, and so the information on Betti numbers is minimal and indirect (see e.g. Section 8). Perhaps most promising is the alternative approach forwarded in the recent study by Feldbrugge & van Engelen (2012) and Feldbrugge et al. (in preparation). On the basis of a graph theoretical approach to Morse theory, they derived path integral expressions for Betti numbers and additional homology measures, such as persistence diagrams. While it is not trivial to convert these into concise formulae such as entailed in the GKF, the numerically evaluated approximate expression for 2D Betti numbers turns out to be remarkably accurate.

From a mathematical point of view, the underlying problem is that while geometric quantities, such as the Lipschitz–Killing curvatures and Minkowski functionals, can be expressed as integrals of local functionals, the same is not true for purely topological quantities. However, even the briefest review of the derivation of the GKF in Adler & Taylor (2010), or any of its simpler variants over the past half century, shows that this localization is crucial to the calculations. The Euler characteristic is the exception that proves the rule here, since, while topological, Gauss’s Theorema Egregium expresses it via local characteristics.

Consequently, a study of the systematics and characteristics of Betti numbers of Gaussian fields cannot be based on insightful and versatile analytical formulae. Hence, we turn to a numerical study of their properties, assessing these on the basis of the

measurements and statistical processing of Betti numbers inferred from realizations of Gaussian fields. This involves the generation of a statistical sample of discrete realizations of Gaussian fields in finite computational (cubic) volumes, described in Section 2. Our investigations also involve the use of an efficient and sophisticated numerical machinery to extract the homology characteristics, and in particular Betti numbers. It is to this computational issue that we turn in the next section.

5 COMPUTATION

The formal definition of Betti numbers relate to a continuous field $f(\mathbb{R}^3) \rightarrow \mathbb{R}$. In most practical situations, including ours, the field or image is represented on a regular cubic grid. It results in a grid representation of the field by arrays of *voxels*, the cubic cells centred at the field sample points. In our study, we have generated the Gaussian field realizations on a 128^3 grid. For exploring the systematics of Betti numbers as a function of the Gaussian field properties, we need a large set of 3D Gaussian field realizations. To facilitate the computation of the topological characteristics of these, we have defined a procedure consisting of two complementary algorithms. The first algorithm, detailed in Bendich, Edelsbrunner & Kerber (2010), defines a formal procedure for computing all Betti numbers of a discretely sampled image on a cubic grid. While optimal and exact, it is computationally expensive. We use it to infer rigorously correct results. In addition, we use it to assure ourselves of the validity of the results obtained by our *Gaussian field optimization method* (Park et al. 2013), a considerably faster computational procedure that is strictly valid only for Gaussian fields and limits the calculation to two Betti numbers. The latter exploits the intrinsic symmetries of Gaussian fields, in conjunction with the unique circumstance of knowing the analytical expression for the genus of isodensity surfaces of a Gaussian field (Adler 1981; Bardeen et al. 1986; Weinberg, Gott & Melott 1987).

Specifically, first we compute the number of isolated islands by counting the number of isolated hot-spots (areas with positive contours as the boundary). Subsequently, we compute the Euler characteristic by evaluating the local curvature and invoking the Gauss–Bonnet theorem to relate it to the Euler characteristic. Finally, we note that the distribution of β_2 is symmetric to β_0 . Using this, we arrive at the value of the first Betti number by invoking the Euler–Poincaré formula, which states that the Euler characteristic is the alternating sum of Betti numbers. Since the zeroth and the second Betti number, and the Euler characteristic are known a-priori, finding the first Betti number reduces to a simple exercise of addition (subtraction). In contrast, in this work, we provide for methods to compute them in a more generic situation from first principles. This will be particularly useful in scenarios where the fields are not symmetric, and little known about their distribution.

5.1 The algorithm

5.1.1 Regular grids and triangulation

The central idea of the algorithm for the homology computation of Betti numbers of a field ρ sampled on a regular cubical grid is to construct a triangulation on the sample voxels. The geometric components of a triangulation – vertices, edges, faces, and tetrahedra – define a simplicial complex whose topological characteristics are equivalent to that of the sampled field. For homology calculations on the basis of such simplicial complexes, one has access to a range of efficient algorithms (see e.g. Morozov 2005).

It is not possible to construct a unique triangulation K from a regular cubical grid of sample voxels. This is because such a cubical grid suffers from various degeneracies: the corners are shared by eight voxels, the edges by four and faces by two. The algorithm solves this by slightly perturbing the regularly spaced grid points along the space diagonal. It leads to a deformed grid where the corners are shared by four voxels, the edges by three, and the faces by two. This transformation defines the elements of the dual triangulation uniquely – the vertices of this triangulation are defined by voxel centres, the edges defined by the centres of the voxels that share a common face, the triangles by the centres of the voxels that share a common edge, and the tetrahedra by the centres of the voxels that share a common corner.

5.1.2 Piece-wise linear interpolation

In a second step of the algorithm, the field values at the vertices in the triangulation are used to interpolate the values on the higher dimensional simplices, much akin to that used in the DTFE formalism developed by van de Weygaert & Schaap (Schaap & van de Weygaert 2000; van de Weygaert & Schaap 2009; Cautun & van de Weygaert 2011). This results in a continuous simplicial field – i.e. a field defined on the edges, faces, and tetrahedra of the resulting simplicial complex – that preserves the topology of the original density field. Of crucial importance is the fact that the choice of interpolation – linear, or constant – has no effect on topology. In this paper we use a piecewise constant interpolation: if $\tau_k (k = 1, \dots, i)$ are the simplices on the boundary of σ , then $\rho(\sigma) = \max[\rho(\tau_1), \rho(\tau_2), \dots, \rho(\tau_i)]$. This yields field values on the edges, faces, and throughout the tetrahedral volumes of the triangulation K .

5.1.3 (Upper star) filtration

For the topology calculation, we assess the homology of a filtration of superlevel sets of the piecewise linear density field. A filtration is a nested sequence of subspaces S^i of the field sample volume $S \subseteq \mathbb{R}^3$, such that $i \leq j$ implies $S^i \subseteq S^j$. This leads to a nested sequence of subspaces

$$\emptyset = S^0 \subseteq S^1 \subseteq S^2 \subseteq \dots \subseteq S^m = S. \quad (68)$$

While m can take infinitely many values, we constrain it to a finite number of values by noting that, according to Morse theory, the superlevel set does not change topology as long as the density level v does not pass a critical point. The critical points of the density function are the minima, maxima, and saddle points. It suffices to compute homology of any one value of the level set between two critical points. This is equally true for a smooth field as for the simplicial linear piecewise field that approximates it, except that one need to slightly adjust the concept of a critical point in the latter case. In the study reported here, the subspaces correspond to the regions where the density value is in excess of the corresponding density threshold v_m .

The Betti numbers are computed for a range of superlevel sets. Computationally, this is achieved by constructing the *upper star* filtration of the simplicial complex. Note that the upper star filtration, defined for piecewise continuous fields, is the discrete version of superlevel sets of the corresponding smooth continuous field. Consider a vertex v_i , and the simplices $\sigma_k (i = 1, \dots, p)$ incident to it. The incident simplices σ_k define the *star* of the vertex. The *upper star* of this vertex v_i consists of all the simplices that

have v_i as their lowest vertex

$$\text{St}^+(v_i) = \{\sigma \in \text{St}_- v_i | x \in \sigma \Rightarrow \rho(x) \geq \rho(v_i)\}. \quad (69)$$

Computing homology of the superlevel set defined by a particular field value ν corresponds to computing the homology of the union of upper stars of all vertices whose field value is greater than or equal to ν .

5.1.4 Boundary matrix and its reduction

To compute the Betti numbers corresponding to a superlevel set, the algorithm subsequently proceeds by constructing the boundary matrix of the union of the upper-star filtration of the vertices whose value is higher or equal to the superlevel set value ν . A p -dimensional boundary matrix is a representation where the columns correspond to p -dimensional simplices and the rows to $(p - 1)$ dimensional simplices. The (i, j) th element of the matrix is 1 if the i th simplex belongs to the boundary of the j th simplex. All other entries are uniformly 0. The boundary matrix is reduced to its Smith normal form, with a part of the matrix in diagonalized form, and the rest of it with empty elements.

5.1.5 Betti numbers: rank of the reduced boundary matrix

The p th Betti number is then given by

$$\beta_p = \text{rank}(\mathbb{Z}_p) - \text{rank}(\mathbb{B}_p), \quad (70)$$

where \mathbb{Z}_p is the null part of the p th boundary matrix and \mathbb{B}_p is the non-zero diagonalized part of the $(p + 1)$ th boundary matrix. The Betti numbers for subsequent superlevel sets are computed by incremental addition of simplices in the upper star of the newly introduced vertices, and updating the boundary matrix as we lower the density threshold. Finally, a reader inclined to gain a deeper understanding of these concepts, may refer to Pranav et al. (2017), where we present the concepts in a greater detail with examples.

6 MODELS

From now on we concentrate on Gaussian random fields over \mathbb{R}^3 , since these are the ones important for the cosmological mass distribution. In order to see how different spectra impact on the topological behaviour of these fields, we consider a number of specific spectra common in cosmological modelling. The first class of examples are those with power-law spectra.

6.1 Power-law spectra

The power-law power spectra are a generic class of spectra, specified by the spectral index n , and given by

$$P(k) = A_n k^n. \quad (71)$$

We will treat the cases $n = 1, 0, -1$, and -2 . In case when $n = 1$, the Harrison–Zel’dovich spectrum is the conventionally expected spectrum for the primordial density perturbations (Harrison 1970; Peebles & Yu 1970; Zeldovich 1972). The measured spectrum of the primordial perturbations is very close to this, with $n \sim 0.96$ (Dunkley et al. 2009; Komatsu et al. 2011; Planck Collaboration XIII 2016). In a cosmological context, we assume that the amplitude of fluctuations at high frequencies is higher than that at low frequencies, which means that $n > -3$. This implies hierarchical

evolution of the subsequently evolving mass distribution, with small-scale perturbations growing faster than the large-scale ones.

To facilitate comparison between the field realizations we have normalized our spectra by equating the spectral amplitude at one particular scale of $8 h^{-1}$ Mpc, corresponding to a frequency of $k_c \approx 0.785 h \text{ Mpc}^{-1}$. Hence, all spectra are set such that all power-law spectra realizations have

$$P(k_c) = A_n k_c^n = A_0 = 1. \quad (72)$$

For a visual appreciation of the impact of these spectra on the behaviour of the corresponding random field, we turn to the visualizations in Figure 3. The figure displays panels showing Gaussian field realizations in thin 2D slices, for power-law spectra with power-law index ranging from $n = 1$ to $n = -2$. Each of the random field realization has been constructed in a simulation box of side $128 h^{-1}$ Mpc with a grid resolution of $1 h^{-1}$ Mpc. The panels in the left-hand column are smoothed with a Gaussian kernel of scale $R_f = 2 h^{-1}$ Mpc, and in the right-hand column with a Gaussian kernel of scale $R_f = 4 h^{-1}$ Mpc. The panels clearly show the increasing dominance of small-scale fluctuations for realizations for higher spectral indices, while the amplitude of large-scale features increases towards progressively negative spectral indices. As the images nicely illustrate, this results in a growing spatial coherence for fields with a more negative spectral index.

The power spectra themselves are shown in Figure 4. Note that the spectra shown are the ones measured from the field realizations. The top left-hand panel shows a realization of the LCDM power spectrum. The remaining panels show realizations of power-law power spectra. For these models, there is relatively more power at the small scales for a higher spectral index in comparison to a lower spectral index. As a result, the field fluctuates rapidly for high spectral indices. As the spectral index decreases, the power shifts towards larger scales. This results in a smoother field with structures at larger scales.

6.2 LCDM spectrum

The LCDM power spectrum stems from the standard concordance model of cosmology. It fits the measured power spectrum of the CMB as well as the power spectrum measured in the nearby large-scale Universe to high accuracy. The shape of the power spectrum can be inferred by evaluating the evolving processes through the epoch of recombination through the Boltzmann Equation (Seljak & Zaldarriaga 1999). A good numerical fit is given by (Bardeen et al. 1986; Eisenstein & Hu 1999; Hu & Eisenstein 1999)

$$P_{\text{CDM}}(k) \propto \frac{k^n}{[1 + 3.89q + (16.1q)^2 + (5.46q)^3 + (6.71q)^4]^{1/2}} \times \frac{[\ln(1 + 2.34q)]^2}{(2.34q)^2}, \quad (73)$$

where

$$q = k/\Gamma, \quad \Gamma = \Omega_m h \exp \left\{ -\Omega_b - \frac{\Omega_b}{\Omega_m} \right\}, \quad (74)$$

Ω_m and Ω_b are the total matter density and baryonic matter density, respectively, and Γ is referred to as the shape parameter. We have used the value $\Gamma \sim 0.21$, which forms a reasonable approximation for the currently best estimates for Ω_b and Ω_m as obtained from the Planck CMB observations (Planck Collaboration XIII 2016). In our study, the power spectrum of the LCDM Gaussian field realizations is normalized by means of $\sigma_8 = 1.0$.

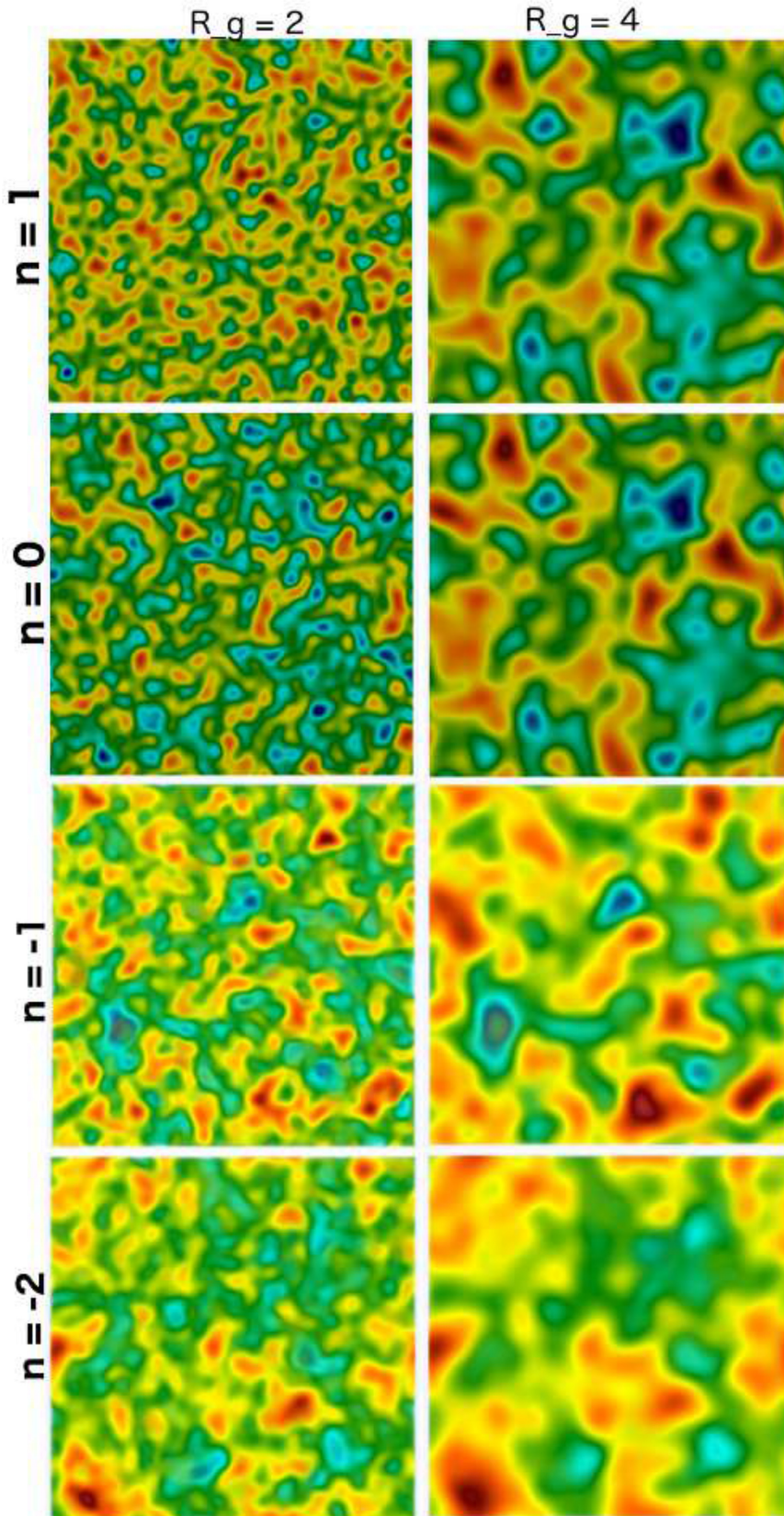


Figure 3. 2D slices of a single realization of 3D Gaussian random field models investigated in this study. The models are constructed in a simulation box of side $128 h^{-1}$ Mpc with a grid resolution of $1 h^{-1}$ Mpc. Subsequently, they are smoothed with a Gaussian kernel of scale $R_f = 2 h^{-1}$ Mpc. The panels in the left-hand column show realizations of power-law power spectra with spectral indices $n = 1, 0, -1$, and -2 , smoothed at $2 h^{-1}$ Mpc. As we go from positive to progressively negative spectral indices, the amplitude of large-scale fluctuations grows, resulting in structures of larger spatial coherence. The panels in the right-hand column show the same realizations smoothed at $4 h^{-1}$ Mpc.

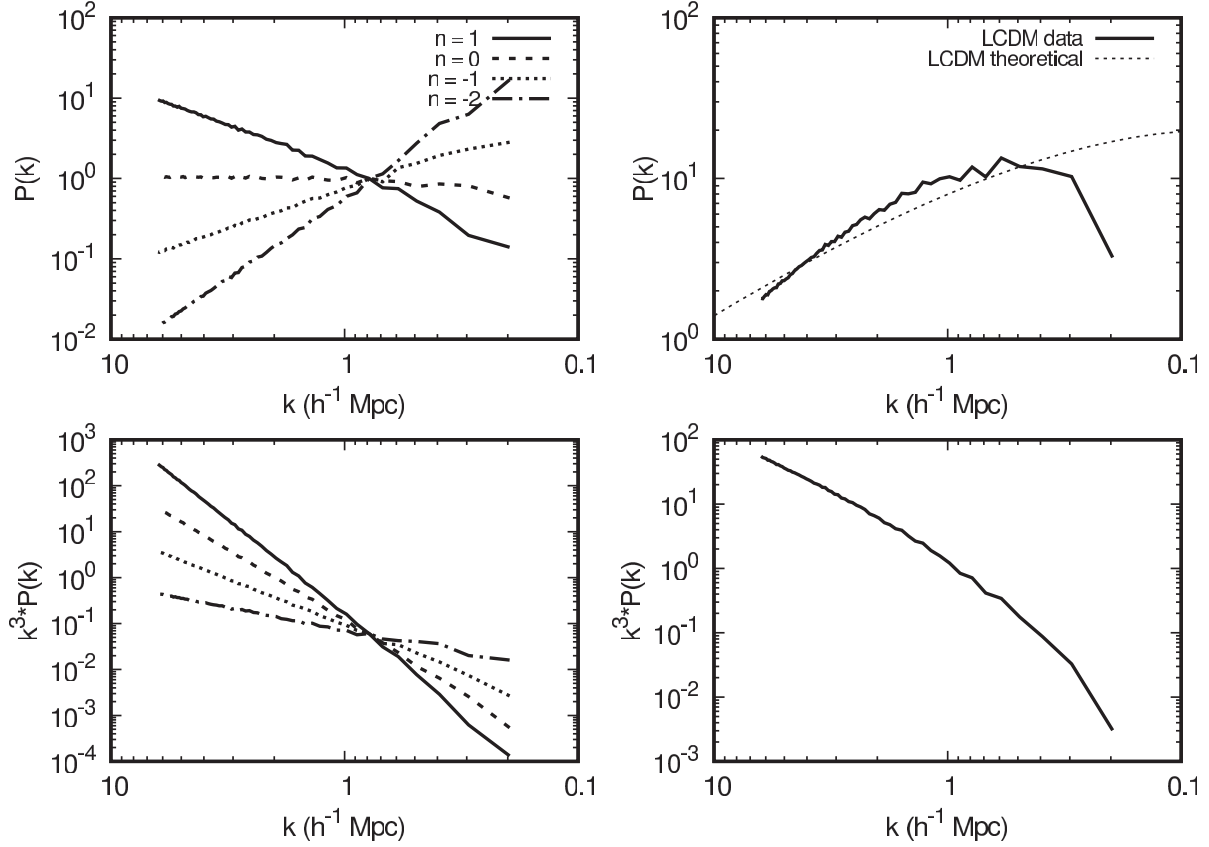


Figure 4. The power spectrum $P(k)$, as well as power spectrum per unit logarithmic bin $k^3 P(k)$. Graphs are presented for the different spectral indices of the power-law model (left-hand column), as well as the LCDM model (right-hand column). The power-law spectra are scaled such that different models have the same variance of the density fluctuations, when filtered with a top hat filter of radius $8 h^{-1}$ Mpc.

Locally, the spectrum resembles a power law, with spectral index $n_{\text{eff}}(k)$, showing a dependence on the scale k , through the relation

$$n_{\text{eff}}(k) = \frac{d \ln P(k)}{d \ln k}. \quad (75)$$

In the asymptotic limit of small and large k , the limits of $n_{\text{eff}}(k)$ are well defined. At very large scales, its behaviour tends towards a power law with index $n = 1$, as can be seen in the plot. At small scales, the LCDM power spectrum behaves like a power-law power spectrum with index $n = -3$. The effective index of the model varies steeply between $n_{\text{eff}} \sim -0.5$ to $n_{\text{eff}} \sim -2.5$ for our models. At the lower limit, the Nyquist mode of the box corresponds to the scale of galaxies of the size of the Milky Way. At the other end the fundamental mode of the box corresponds to scales well beyond which the Universe appears homogeneous.

6.3 Model realizations and data sets

The samples of Gaussian field realizations are generated in a cubic volume on a finite grid, with periodic boundaries, achieved by identifying and gluing opposite sides, transforming a finite \mathbb{R}^3 domain to \mathbb{T}^3 . It concerns field realizations on a grid with $N = 128^3$ grid points. The fields are generated by our (constrained) initial conditions code (van de Weygaert & Bertschinger 1996). It involves the generation of 128^3 independent Gaussian distributed Fourier field components $\hat{f}(\vec{k}_i)$, and the subsequent inverse FFT transform to yield the corresponding density field. The FFT automatically assures a cubic volume field realization with periodic boundary

conditions. Table 1 lists the relevant parameters of the sample of Gaussian field realizations used in our study.

In effect, the field realizations have the specified power spectrum amplitude (Equation 71) between the fundamental mode and Nyquist mode of the grid, while they are zero for lower and higher frequencies. Effectively, the realized spectrum is therefore a block spectrum. For the power-law spectra this circumvents the divergences that beset pure power-law spectra. The cubic sample volumes have a side of $128 h^{-1}$ Mpc with a grid resolution of $1 h^{-1}$ Mpc, corresponding to a fundamental mode of $k_{\text{fund}} = 2\pi/128 h \text{ Mpc}^{-1} \approx 0.049 h \text{ Mpc}^{-1}$ and an Nyquist frequency $k_{\text{Nyq}} = 2\pi/2 h \text{ Mpc}^{-1} \approx 3.14 h \text{ Mpc}^{-1}$.

The statistical results that we obtain in our numerical study of homology and Betti numbers are based on 100 different field realizations for each tested power spectrum. For each realization we evaluate Betti numbers, Euler characteristic, and Minkowski functionals. Subsequently, we average over these 100 realizations. It is these averages that form the data set which we will subsequently analyse in Sections 7 until 10.

7 BETTI NUMBER ANALYSIS: 3D GAUSSIAN RANDOM FIELDS

In this section, we analyse the topological characteristics of the models in terms of the Betti numbers on the basis of our numerical study of the homology of our sample of Gaussian field realizations. The discussion is based on the statistical evaluation of these results.

Table 1. Parameters Gaussian field realization data set. The columns specify: (1) class number, (2) name power spectrum, (3) index power spectrum, (4) number of grid points, (5) number of field realizations, (6) normalization power spectrum, and (7) normalization wavenumber k_c .

Number	Power spectrum	Index n	# grid point	# field realizations	Normal	k_c ($h \text{ Mpc}^{-1}$)
1	ΛCDM	–	128 ³	100	$\sigma_8 = 1.0$	–
2	Power law	– 2.0	128 ³	100	$\sigma_8 = 1.0$	0.785
3	Power law	– 1.0	128 ³	100	$\sigma_8 = 1.0$	0.785
4	Power law	– 0.0	128 ³	100	$\sigma_8 = 1.0$	0.785
5	Power law	1.0	128 ³	100	$\sigma_8 = 1.0$	0.785

The intention of the analysis is an evaluation of the generic properties of Betti numbers as a function of field power spectrum and to compare the properties of Betti numbers with the topological behaviour in terms of the Euler characteristic. To this end, the three Betti numbers β_0 , β_1 , and β_2 are computed for superlevel sets of the (filtered) Gaussian fields, defined by dimensionless density threshold $\nu = f/\sigma$. The variation of the Betti numbers as a function of the threshold ν forms the principal resource for our investigation of the topological properties of Gaussian random fields. An important thing to note is that we perform our analyses on periodic cubes, or equivalently, the manifold is \mathbb{T}^3 , which is without boundary. An important consequence is that the Euler characteristic curve (and hence the Betti numbers also), are symmetrized due to the absence of boundary terms; see Section 4.5 for an explanation on how the boundary terms affect the Euler characteristic computation.

In an earlier article, we presented a brief investigation of Betti numbers of Gaussian fields, focusing on their important features with respect to a comparison with genus statistics (Park et al. 2013).

7.1 Gaussian Betti characteristics: general properties

Figure 5 presents the Betti number curves for a typical realization of a Gaussian field. For Gaussian fields, β_0 and β_2 appear to mirror each other about $\nu = 0$. The number of independent tunnels, in terms of β_1 , appears symmetric to itself under reflection about $\nu = 0$. The symmetries observed in the Betti number curves are a reflection of the underlying symmetry in the field itself. Because of their symmetry, an analysis with respect to the islands is also indicative of the properties of voids.

At $\nu = \pm\sqrt{3}$, the number of isolated islands and voids attain their maximum. At $\nu = 0$, the number of isolated islands equals the number of isolated voids, i.e. $\beta_0 = \beta_2$. It is an interesting observation that these numbers are *not* equal to unity, as should have been the case for a pure *Sponge-like* topology. This is evident from the inset where we zoom into the median density threshold region where β_0 and β_2 overlap, resulting in small but non-unity numbers for both islands and voids. At the same threshold, we see that the number of tunnels/loops reaches a maximum. It signifies a morphology in which several large interconnected overdense island and void regions are interspersed with a complex anatomy of percolating tunnels, a result of the complex mutual intertwining of these manifolds.

To appreciate the topological characterization, the Betti numbers clearly provide crucial new insights. By evaluating β_0 and β_2 at a given density level, we may assess what the contributions of the overdense islands and underdense cavities are to the genus characterization, and in how far tunnels through, and in these features contribute to the definition of a complex topology. The symmetric and relatively simple nature of Gaussian fields is helpful

in identifying the connection between Betti numbers, genus, and overall topological character.

One of the principal topological characteristics of Gaussian fields is their relative simplicity, in that the three Betti numbers dominate the topology at different density ranges. In this sense, Gaussian field are rather unique. In the case of most complex patterns encountered in nature, the density range over which all three Betti numbers have significant non-zero values is far larger than that in Gaussian fields. In this sense, we may consider Gaussian fields to have a comparatively simple topological structure. Both Figs 5 and 6 reveal this circumstance.

The left-hand panel of Figure 6 plots the sum of the Betti numbers in dot-dashed curves, alongside the different Betti numbers themselves (solid curves). It is clear that for $|\nu| \gtrsim 2\sigma$, β_0 and β_2 dominate the topology for the positive and the negative thresholds, respectively. In between $|\nu| \lesssim 1\sigma$, β_1 is the dominating component. Similar information can also be gleaned from the right-hand panel, where we present the fractional Betti numbers, denoting the ratio of a particular Betti number to the sum of all Betti numbers as a function of the density threshold. It is evident that the three Betti numbers dominate different density regimes, albeit with a substantial range of overlap for $|\nu| \lesssim 2\sigma$.

Characteristic therefore for Gaussian fields is that the topology at extreme density values is dominated by a single class of features, cavities, or islands. At very high density levels the topology is entirely dominated by the islands and thus fully specified by β_0 . The topology is predominantly *Meatball-like*, marked by the presence of isolated components (or islands). The same is true at very low density levels, where the topology is entirely specified by β_2 and thus exclusively dominated by cavities, i.e. the central region of voids. Here the topology is distinctly *Swiss-cheeselike*.

At more moderate levels, for $|\nu| \lesssim 2$, the topology attains an increasingly *Sponge-like* character. In these regimes at least two Betti numbers are needed to describe the topology of the superlevel manifolds. On the lower density side, the topology is dominated by β_2 and β_1 . It reflects a pattern of isolated cavities indicating agglomerates of density troughs, interspersed by tunnels and loops. On the higher density side, the topological signal consists mostly of β_0 and β_1 . The corresponding spatial pattern is that of an agglomerate of isolated islands, infused and punctured by numerous tunnels. In a relatively narrow density range around the mean density, for $|\nu| \lesssim 0.1 - 0.2$, we even observe the simultaneous existence of all three topological features, cavities, islands, and tunnels. In that regime, all three Betti numbers are needed to quantify the Gaussian field topology.

An interesting aspect of the Gaussian field topology concerns the role of tunnels. Starting at high-density values and proceeding towards lower density values, the number of disconnected islands reaches a maximum at threshold $\nu = \sqrt{3}$. At a slightly higher

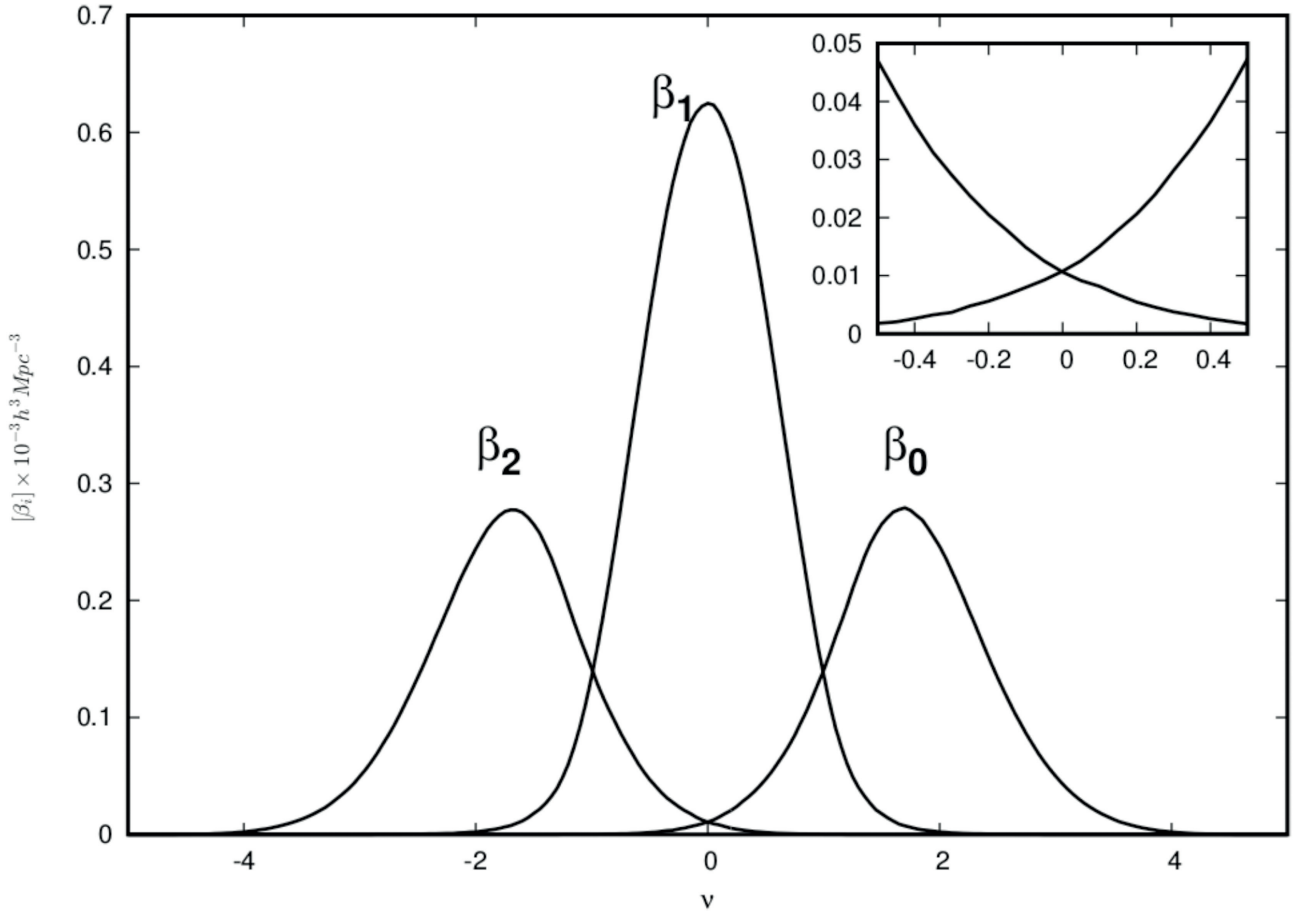


Figure 5. The Betti numbers for the $n = -1$ model. It is evident that the different Betti numbers dominate the topology in the different density thresholds regions, and also the Euler characteristic curve. For high thresholds, β_0 is the dominant topological feature. For intermediate thresholds, β_1 dominates, while for low thresholds β_2 is the dominant topological entity. Inset: The zone of overlap between β_0 and β_2 curves, at the median density threshold. Both the quantities are non-unity, indicating that the manifold is not a single connected surface, and hence does not exhibit pure *Sponge-like* topology.

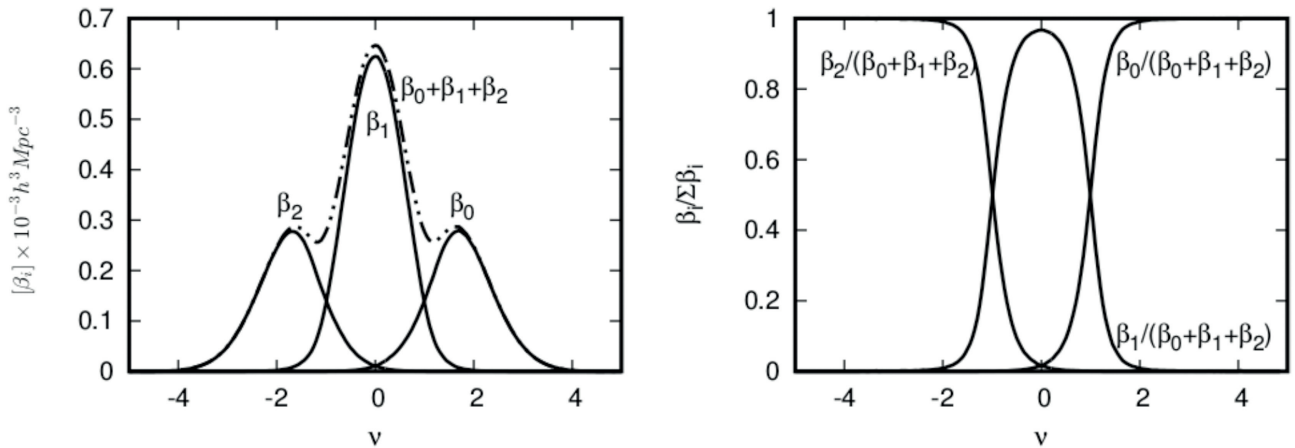


Figure 6. Figure illustrating the dominance of different Betti numbers in the different density threshold regions. The left-hand panel plots the sum of Betti numbers for the different thresholds, along side the individual Betti numbers. The right-hand panel presents the ratio of the individual Betti numbers to their sum as a function of the density threshold.

threshold, $\nu \approx 2$, we start to see the rapid increase of the β_1 curve. This is the result of the formation of ever larger island complexes by the merger of higher density objects, along with the emergence of tunnels that permeate their interior and surface.

At intermediate thresholds, $|\nu| \lesssim 1$, tunnels become the most populous topological feature. They gradually attain their maximum presence at the median density threshold, as nearly all high-density components have merged into one huge percolating and irregularly

shaped complex. The surface and interior of the complex is marked by the presence of a large number of these permeating tunnels. To follow the entire process in detail, we refer to our description and discussion of the corresponding persistence diagrams in the upcoming accompanying paper (Pranav et al., in preparation).

A similar role of tunnels and loops is seen on the low-density side of the Gaussian field. Starting at the very low densities, from the β_2 curve we note the dominant presence of underdense troughs and enclosed cavities. The number of independent cavities reaches a maximum at threshold $\nu = -\sqrt{3}$. Proceeding towards higher density values, an increasing number of cavities that were isolated, start to connect and merge, forming ever larger ‘oceans’. By density level $\nu = -2$, the merged ocean complexes are accompanied by a strongly growing presence of loops, signifying a complex topology. The steep rise of the β_1 curve reflects this quantitatively. Approaching median density levels, nearly all cavities have been absorbed in one large ocean, whose irregular shape and surface is reflected in the β_1 curve reaching its maximum value.

It is also interesting to assess the topological identity at the median density level, $\nu = 0$. At that level, we see the presence of an equal number of islands and cavities. That is, β_0 and β_2 are equal at $\nu = 0$. Conventionally in the literature, for Gaussian fields, it is assumed that all overdense regions have merged into one percolating complex at the median density threshold, interlocked with one equivalent interlocking underdense ocean. This would define a pure *Sponge-like* topology. This has been assumed on the basis of the analyses of genus curves, e.g. Gott et al. (1986, 1989). However, it remains to be seen whether indeed such an ideal sponge-like topology exists, even in the case of Gaussian random fields. Below we will find that, in general, this is not true, with the topology at median levels determined by a few – disconnected – overdense complexes, intertwined with a few underdense ones. The dissection of the genus curve into the contributing Betti curves reveals this phenomenon, shedding new insights on to this issue.

7.2 Betti number characteristics: dependence on power spectrum

Having established the generic behaviour of the Betti curves of Gaussian fields, we investigate their systematic trends and dependence on the power spectrum of the field realizations. One of the findings that we earlier reported in Park et al. (2013) is that Betti numbers depend on the shape of the power spectrum. The top panel of Figure 7 shows the unscaled Betti number curves for the various power-law models. The bottom-left and the bottom-right panels plot enlargements of the regions of overlap between (β_0, β_2) and (β_0, β_1) , respectively.

The first direct observation is that there is a steep increase of all three Betti curves, over the entire density range, as the power spectrum index n increases. That is, the number of topological features – islands, cavities, and tunnels – is steeply increasing as the small-scale fluctuations in the density field are more prominent and have a higher amplitude. This is in line with what would be expected for Gaussian fields.

For all power spectra, we find that the β_0 curve reaches its maximum at the characteristic density threshold $\nu = \sqrt{3}$, while the β_2 reaches its maximum at $\nu = -\sqrt{3}$, and β_1 at the mean density level $\nu = 0$. Also, for all power spectra we find that at $\nu = 0$, the number of overdense islands is the same as underdense cavities, i.e. $\beta_0 = \beta_2$. Furthermore, there is an overlap of the different Betti numbers in determining the topological identity of the manifold at different density thresholds. The bottom two panels of Figure 7

substantiate this claim. The number of isolated islands is equal to the number of isolated voids at $\nu = 0$, and the number of isolated islands (voids) is equal to the number of isolated tunnels at $\nu = 1(-1)$. This symmetry is related to the fact that the simulations are realized on the 3-torus, implying that the manifold is without boundary.

The corresponding scaled Betti curves are shown in Figure 8. The top panel plots Betti numbers, where each β_i of a model is normalized by the β_1 corresponding to that model. The bottom panel plots the Betti numbers, where each β_i is normalized by the amplitude of β_i of $n = 0$ model. Interestingly, both the figures present identical shapes for the curves, even though differing in the normalization procedure (see the vertical axes for values and units). The amplitudes of β_0 (β_2) curves compared to that of β_1 are also different for the different normalization procedure. The top-left and the top-right panels of Figure 9 presents the enlargements of the relevant regions of overlap between the different scaled Betti number curves.

7.2.1 Overlap of Betti curves: topological identity

The scaled Betti number curves provide supplementary information on systematic trends with respect to the relative importance and prevalence of the various topological features. It allows us to investigate in how far the observed changes in Betti number curves affect the range over which we can speak of *Meatball-like* and *Swiss-cheeselike* topology. It also allows us to assess in how far the *Sponge-like* appearance at median density range is affected.

All models retain the exclusive *Meatball-like* topology at high-density thresholds $\nu \gg \sqrt{3}$, i.e. an almost exclusive presence of isolated islands, and a similar exclusive dominance by cavities for $\nu \ll -\sqrt{3}$, outlining a typical *Swiss-cheeselike* topology. At intermediate density range, we notice a few interesting trends as the spectral index n decreases and large-scale fluctuations attain a larger prominence in the Gaussian fields. We see a systematically growing overlap between the various Betti curves.

The β_0 and β_2 curves become less skewed and hence more symmetric as the value of n decreases. It means that the number of these features at $|\nu| < \sqrt{3}$ is more comparable to that at the higher density levels. Instead of a steep falloff of β_0 and β_2 for $|\nu| < \sqrt{3}$ due to the rapid merging of objects and cavities into a single percolating island and ocean, a relatively large number of them remain intact over a wider density range. It implies that the presence of stronger large-scale perturbations goes along with a – relatively – higher number of disconnected objects and cavities at medium density values and that these characteristically large-scale objects and cavities remain independent down to lower density levels. It is most likely a manifestation of the lower level of clustering in Gaussian fields with a lower spectral index n .

Also interesting is the fact that as the index n decreases, we start to see an increasing range of overlap between β_0 and β_2 . In other words, at $|\nu| < \sqrt{3}$ we not only see a relatively larger number of islands or cavities, there is also the presence – in absolute numbers – of an increasing number of these that even remain below the mean density value $\nu = 0$. In terms of β_0 , from Figure 8, and zoom-ins in the concerned overlapping regions in Figure 9, we see there are isolated islands living in large underdense regions. The presence of a progressively larger number of isolated islands at density levels below the mean can also be inferred from the fractional Betti number plots in Figure 10. For the $n = -2$ model, we find a non-zero β_0 for thresholds as low as -2σ . In a sense, it is reminiscent of the

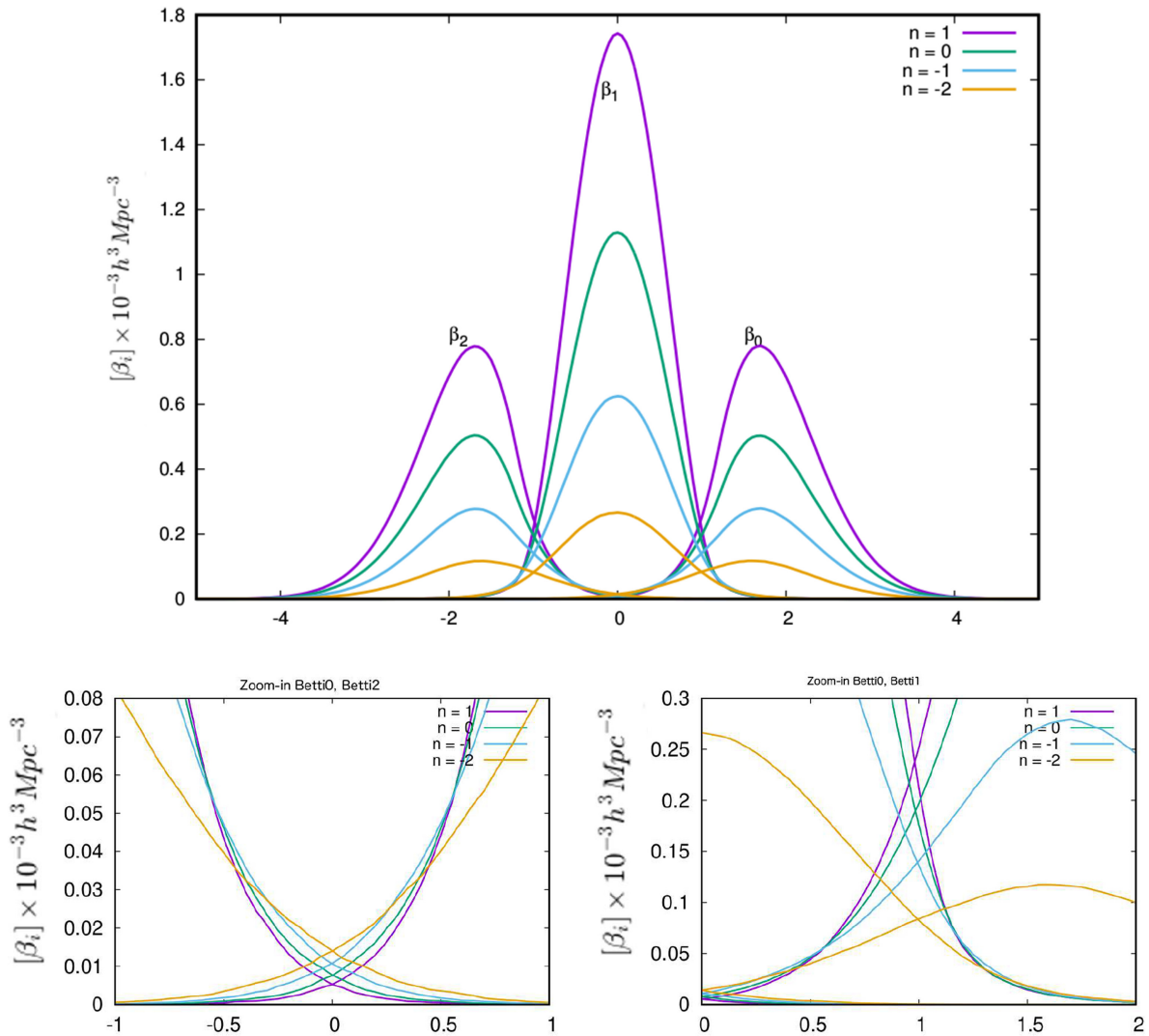


Figure 7. Top: Unscaled Betti number curves of Gaussian random fields for the power-law models. The curves are drawn for spectral index $n = 1, 0, -1,$ and -2 , as a function of the dimensionless density threshold ν . β_0 and β_2 curves are symmetric to each other with respect to the median density threshold, but exhibit visible skewness, increasing with increasing spectral index. β_1 curve is symmetric to itself with respect to $\nu = 0$, and exhibits no skewness. Bottom-left: Zoom-in into the region around median density threshold of the top panel shows the small but non-zero contributions from β_0 and β_2 , more for lower spectral indices. The manifold is not strictly *Sponge-like* in general, but consists of multiple isolated objects as well as enclosed cavities, as opposed to the expectation of a single percolating overdense region intertwined with a single percolating underdense network of tunnels, for all the models examined. Bottom-right: Zoom-in into the region of overlap for β_0 and β_1 .

cloud-in-void process identified by Sheth & van de Weygaert (2004) in their description of the formation of voids in the cosmic mass distribution. One aspect of this is existence of overdense isolated haloes (islands) in an overall underdense void region, which would emanate from precisely the primordial configuration identified here by the β_0 Betti number curve being non-zero at negative density values ν . The opposite process, *void-in-cloud*, is reflected in the increasing presence of β_2 at positive density thresholds while the spectral index n is lower. Such cavities still existing at positive densities ν may be compared to lakes in a mountain range.

The presence of tunnels also changes as a function of the power spectrum. Relatively speaking, for decreasing spectral index n , there is a lower number of tunnels per object at the lower density levels $|\nu| < 1$ (Figure 10). As tunnels are often forming along with the merging of islands, the lower number of tunnels may be a consequence of the relatively large number of islands – and cavities – that did not yet

connect up at these density levels. Interestingly, at higher density levels of $|\nu| > 1$, there appear to be more tunnels per island or cavity for lower spectral indices n . At lower density levels, a sizeable number of these tunnels appear to have filled up and disappeared. The bottom-left and the bottom-right panels of Figure 9 plot the value A_{eq} at which the overlap occurs, and the numbers for the concerned topological identities are equal, as a function of $(n + 3)$, where n is the spectral index, in absolute and log units, respectively.

Finally, we may answer the question in how far we can still describe the topology around the mean density threshold as *Sponge-like*. Clearly, as the spectral index n decreases, we see an increasing presence of islands and cavities at the mean density, going along with a decreased presence of tunnels. Instead of one connected and percolating overdense region intertwined with a similarly connected underdense region, the topological identity of the density field at median density is one in which more than one disconnected

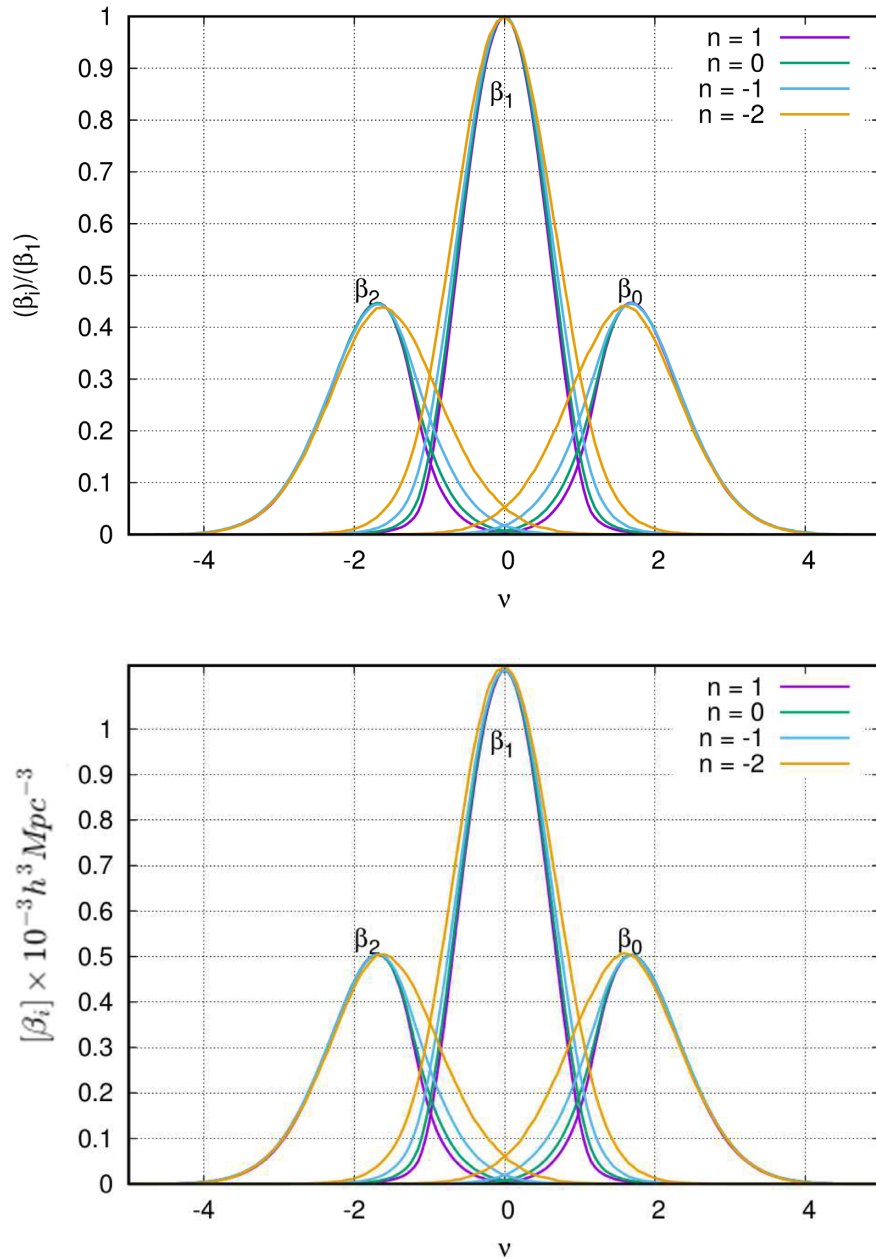


Figure 8. Scaled Betti number curves of Gaussian random fields. The top panel plots Betti numbers, where each β_i of a model is normalized by the β_1 corresponding to that model (also cf. Park et al. 2013). The bottom panel plots the Betti numbers, where each β_i is normalized by the amplitude of β_i of the $n = 0$ model.

overdense region is filling up space with several similarly shaped underdense regions. These regions are also marked by irregular, intricately shaped boundaries, marking a complex intertwining of each other, involving a large number of tunnels and loops. The number of disjunct overdense and underdense complexes increases with decreasing spectral index n . Strictly speaking this is not a *Sponge-like* topology, although practically speaking it shares a similar morphology of a complex convoluted structural pattern. See Figure 1 for a visualization of the contour surfaces for different density thresholds for the $n = 1$ and $n = -2$ models.

7.3 Spectral scaling properties of Betti numbers

Given the clear dependence of the Betti number curves on the power spectrum of the Gaussian field, it would be insightful to evaluate the scaling of descriptive parameters of the Betti curves. We find that the systematic changes are entirely equivalent for the β_0 and β_2 curves. Two aspects that we investigate are the amplitude and shapes of the Betti number curves. The shapes are investigated in terms of the skewness and kurtosis of the curves.

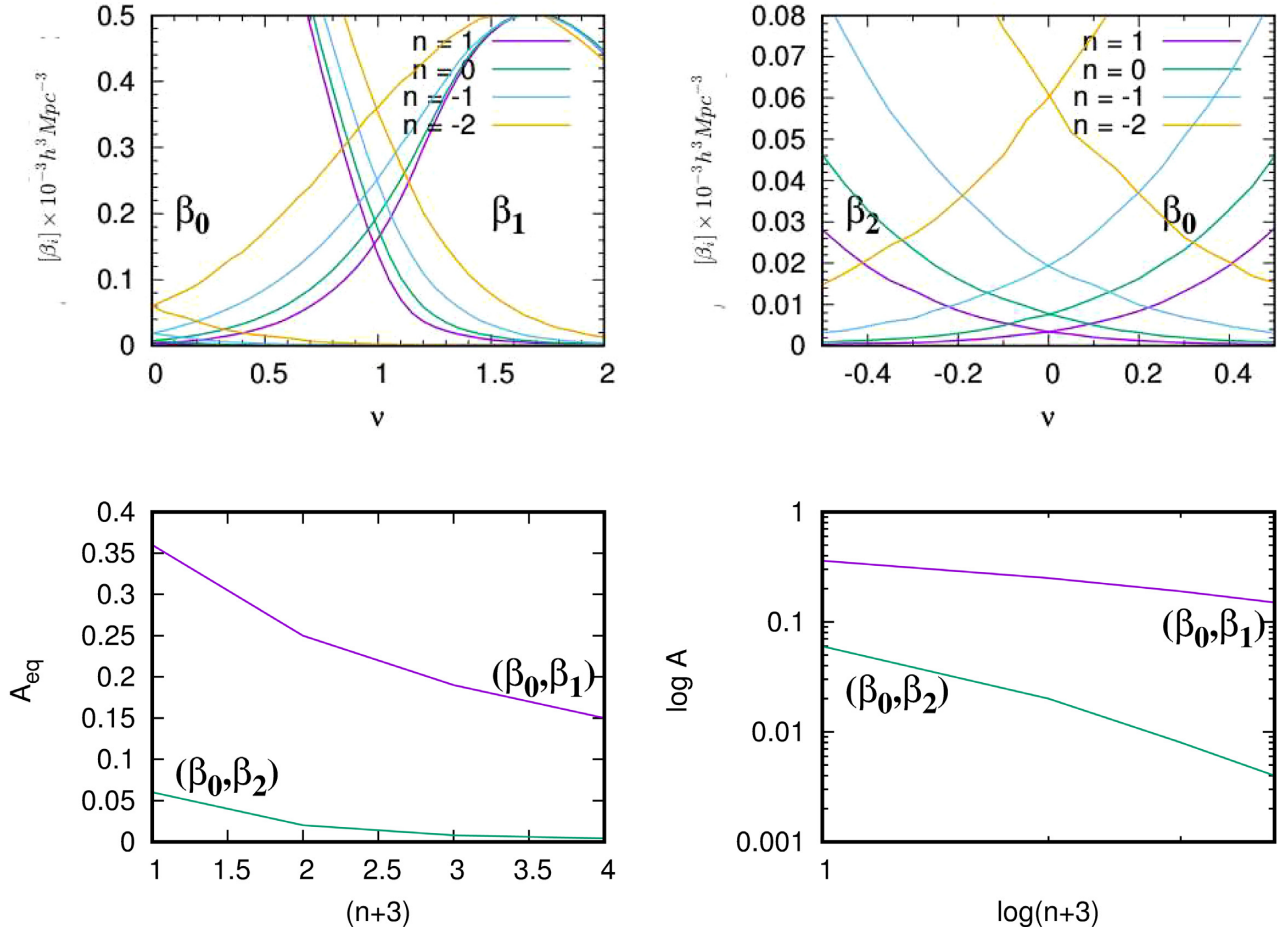


Figure 9. The top-left and the top-right panels present the enlargements of the density range where scaled Betti number curves of Gaussian random fields overlap. The curves are drawn for the power-law models as a function of the dimensionless density threshold ν . The bottom-left and bottom-right panels plot the value of ν at which the overlap occurs as a function of $(n+3)$, where n is the spectral index, in absolute and log units, respectively.

7.3.1 Scaling of Betti number amplitude with spectral index

The amplitudes of the unscaled Betti numbers depend on the value of the spectral index n . The trend of the dependence of the maximum of the Betti number curves on the value of the spectral index is shown in Figure 11. The amplitude of the Betti numbers, defined as the maximum of the Betti number curves, approximately follows an exponential. By fitting

$$f(n) = A_0 \exp\left\{\frac{n}{\tau}\right\}, \quad (76)$$

we find a decay parameter $\tau \approx 2$. Amongst others, it implies that the amplitude of the Betti number curves decreases roughly exponentially as the value of spectral index n decreases.

7.3.2 Shape of the Betti curves: skewness and kurtosis

The shape of the Betti number curves show a dependence on the choice of the power spectrum: the Betti number curves become broader as n decreases, the β_0 and β_2 curves also appear more symmetric. To appreciate this optimally, we scale the Betti number curves. Figure 8 nicely illustrates the systematic changes in width and asymmetry of the curves as a function of n . The figure also shows that changes of the Betti number curves on n are nearly exclusively confined to the range $|\nu| \leq \sqrt{3}$.

Quantities that characterize the shape of the Betti number curves are the skewness μ_3 and kurtosis μ_4 , quantifying properties such as asymmetry and narrowness of the curves. The systematic relation between these quantities and power-law index is presented in Table 2. All the quantities exhibit non-zero skewness. Interestingly, this is also the case for β_1 , even though examining by eye they look symmetric for all the models. This is perhaps due to the influence of the tail of the distribution, where, even though, the numbers are small, they are not the same for positive and negative thresholds.

7.3.3 Scaling of Betti number amplitude with Gaussian filter radius R_g

Figure 12 presents the graphs of the Betti number curves for the various power-law models, where they are smoothed by a Gaussian filter radius $R_g = 2, 3, 4,$ and $5 h^{-1}$ Mpc. Panels (a) to (d) present the curves for $n = 1, 0, -1,$ and -2 models, respectively. Within each panel, the different colours of the curves represent the different smoothing radii. Panel (e) shows the graph of the amplitude of the Betti curves as a function of smoothing radius. Curves with the same colours represent the same model. The dotted curves are for β_1 , while the solid and the dashed curves represent β_0 and β_2 , respectively. The curves for β_0 and β_2 coincide with each other, indicating that their amplitudes are identical. Panel

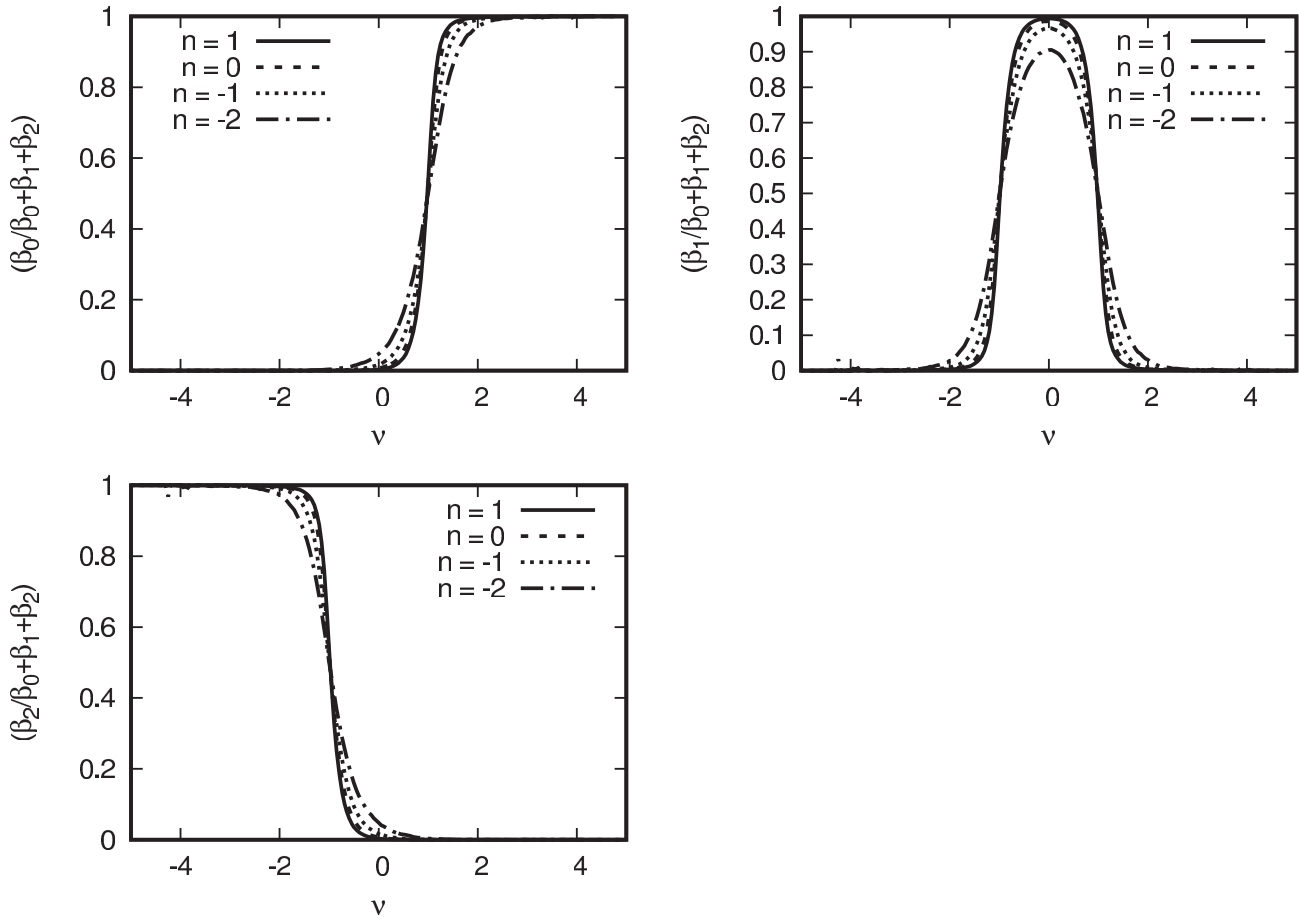


Figure 10. The fractional contribution of islands, tunnels, and voids to the sum of Betti numbers in all three dimensions for rms threshold range between $(-5\sigma; 5\sigma)$ for the different power-law models. Top-left: $\beta_0/(\beta_0 + \beta_1 + \beta_2)$ – fractional contribution of islands to the total sum of Betti numbers. Top-right: $\beta_1/(\beta_0 + \beta_1 + \beta_2)$ – fractional contribution of tunnels to the total sum of Betti numbers. Bottom-left: $\beta_2/(\beta_0 + \beta_1 + \beta_2)$ – fractional contribution of voids to the total sum of Betti numbers.

(f) presents the same curves as panel (e), but on a logarithmic scale.

The amplitudes for β_0 , β_1 , and β_2 scale the same as a function of the smoothing length R_g . We fit the maximum of the peaks to the function $\beta_i^{max} = A_0 R_g^{-\tau}$. The value of the power-law index of the fit is $\tau = 3$, irrespective of the model.

7.4 Betti numbers and Euler characteristic

The top panel of the Figure 13 presents the Betti curves for the $n = -1$ model. The bottom panel of the same Figure presents the Euler characteristic. The extrema of the three 3D Betti numbers correspond to the three extrema of the Euler characteristic curve. Only for large thresholds $|\nu| > 3$, β_0 and β_2 are almost equal to $-\chi$. This is because the absolute value of the Euler characteristic is very close to the number of excursion sets or peaks in the asymptotic limit of high-density thresholds (Adler 1981; Bardeen et al. 1986; Park et al. 2013). For thresholds as large as $\nu \sim 2$, there is a significant contribution from β_1 to χ .

The left-hand panel of the Figure 14 presents the Betti numbers as well as the Euler characteristic for the different power-law models. Note that the different Betti numbers dominate different regions of the Euler characteristic curve. The magnitude of the amplitude of the Euler characteristic curve is lower in general compared to the

Betti curves; as an example, for the $n = -2$ model, this is even as large as 10–15 per cent. This can be confirmed independently from the right-hand panel of Figure 10. Similarly, in the right-hand panel of Figure 14 we see that the amplitude of χ is lower than the amplitude of β_1 . The difference becomes larger as the spectral index decreases. It is an indication of the presence of a significant number of islands and voids at $\nu = 0$ for lower spectral indices.

The above observations can be related to the nature of the density fluctuation field as a function of spectral index. For higher spectral indices, there is significant power only at smaller scales. This results in high-density peaks connected by low-density saddles, giving the field a distinctly spiky appearance. These peaks get connected before they start forming tunnels and voids, resulting in a clear cut demarcation of *Meatball-like*, *Sponge-like*, or *Swiss-cheeselike* topology. As the spectral index decreases, the demarcation diffuses. As the spectral index decreases, progressively more and more isolated islands contain additional topological holes of higher dimensions, at thresholds well before the manifold becomes a singly connected entity. This is reflected in the broadening and increased overlap of the Betti number curves, indicating an increase in the mixture of topology as the spectral index decreases. In contrast, the Euler characteristic curve does not have this dependence. As a result, this additional information about the inherent differences

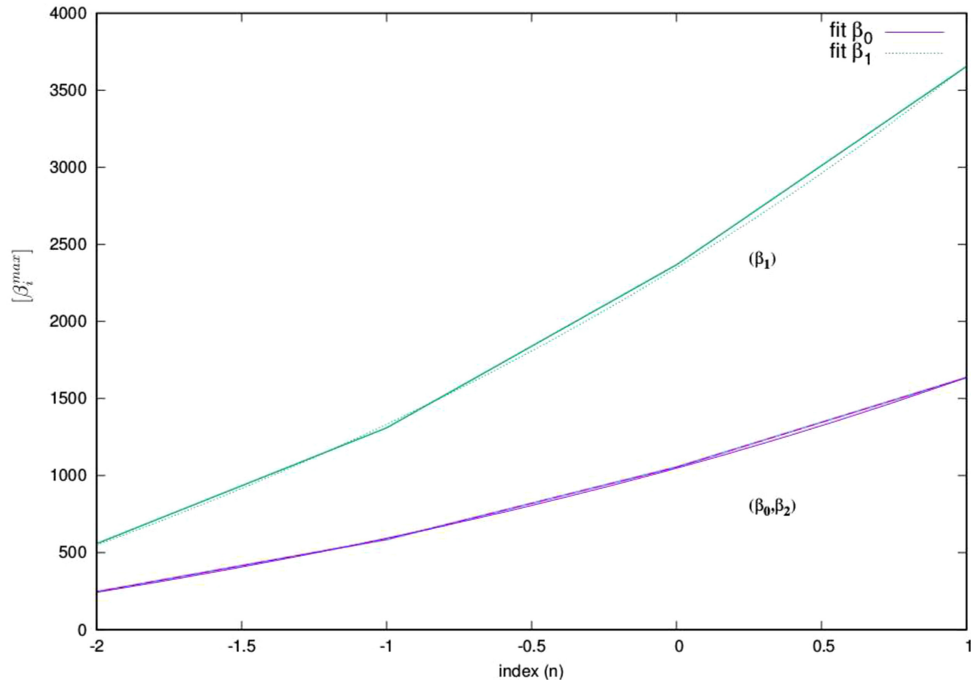


Figure 11. Amplitude of Betti numbers as a function of the spectral index (also cf. Park et al. 2013). The curves are fit to an exponential of the form $A_0 \cdot \exp n/\tau$, with $\tau = 2 \pm 0.19$.

Table 2. Table listing the skewness and kurtosis values for the Betti curves of the various models.

Model	Skewness			Kurtosis		
	β_0	β_1	β_2	β_0	β_1	β_2
$n = 1$	-4.583	$5.727e-05$	4.584	9.134	0.047	9.136
$n = 0$	-4.737	$-7.33e-05$	4.736	9.546	0.055	9.541
$n = -1$	-4.977	$-2.117e-05$	4.974	10.260	0.090	10.260
$n = -2$	-5.015	$-3.789e-05$	5.029	10.764	0.280	10.803

in the topological structure of the various power-law models is not available from the Euler characteristic curves.

The left-hand panel of Figure 15 shows the unscaled Euler characteristic curves for the power-law models. The right-hand panel presents the scaled Euler characteristic curves for the same models. The scaled curves fall on top of each other, indicating that the shape of the Euler characteristic curve is insensitive to the choice of power spectrum. This is unlike the Betti numbers, whose shapes show a characteristic dependence on the choice of the power spectrum. The dependence of Euler characteristic on the choice of the power spectrum is restricted to the expression for amplitude through the variance term.

The above remarks lead us to conclude the following. In general, only for positive spectral indices, it is feasible to describe the topology of the field as either *Meatball-like*, or *Sponge-like* or *Swiss-cheeselike*. For negative spectral indices, the demarcation is not clear, except near the tails of the density distribution. The topology is an increasing mixture of the three types as the spectral index decreases. It is clear that the Betti numbers add extra information to the description of topology than that by the Euler characteristic.

7.5 β - and ζ -tracks

Another means of gleaning the topological information content from the Betti numbers is to visualize them assuming they define

coordinates in a 3D space of $(\beta_0, \beta_1, \beta_2)$. The left-hand panel of Figure 16 presents such *Betti tracks* for a typical Gaussian field realization. There are more ways to exploit the additional information content of the Betti numbers. Since the Euler characteristic is the alternating sum of Betti numbers, $\chi = \beta_0 - \beta_1 + \beta_2$, this can be interpreted as the projection of $(\beta_0, \beta_1, \beta_2)$ on to the line in direction $(1, -1, 1)$. Following this geometrical interpretation, we may identify combinations of the Betti numbers that are orthogonal to the line $(1, -1, 1)$, and thus provide independent additional topological information to the Euler characteristic:

$$\begin{aligned} \zeta_1 &= \beta_0 - \beta_2 \\ \zeta_2 &= \beta_0 + 2\beta_1 + \beta_2 \\ &= (\beta_0 + \beta_1) + (\beta_1 + \beta_2), \end{aligned} \quad (77)$$

i.e. the vectors $(1, 0, -1)$, $(1, 2, 1)$, and $(1, -1, 1)$ form an orthogonal system. By looking at the distribution of (ζ_1, ζ_2) (ζ -tracks from now on) in the plane defined by axes $(1, 0, -1)$ and $(1, 2, 1)$ we get an appreciation for the supplementary topological information yielded by Betti numbers, in addition to the Euler characteristic. The right-hand panel of Figure 16 presents the curves for ζ -track for a typical field realization. We notice that for high-density thresholds up to $\nu \sim 2$, ζ_1 and ζ_2 coincide with each other, but show different trends for lower thresholds. Note that the β - and the ζ -tracks may provide additional tools when model discrimination is the primary focus.

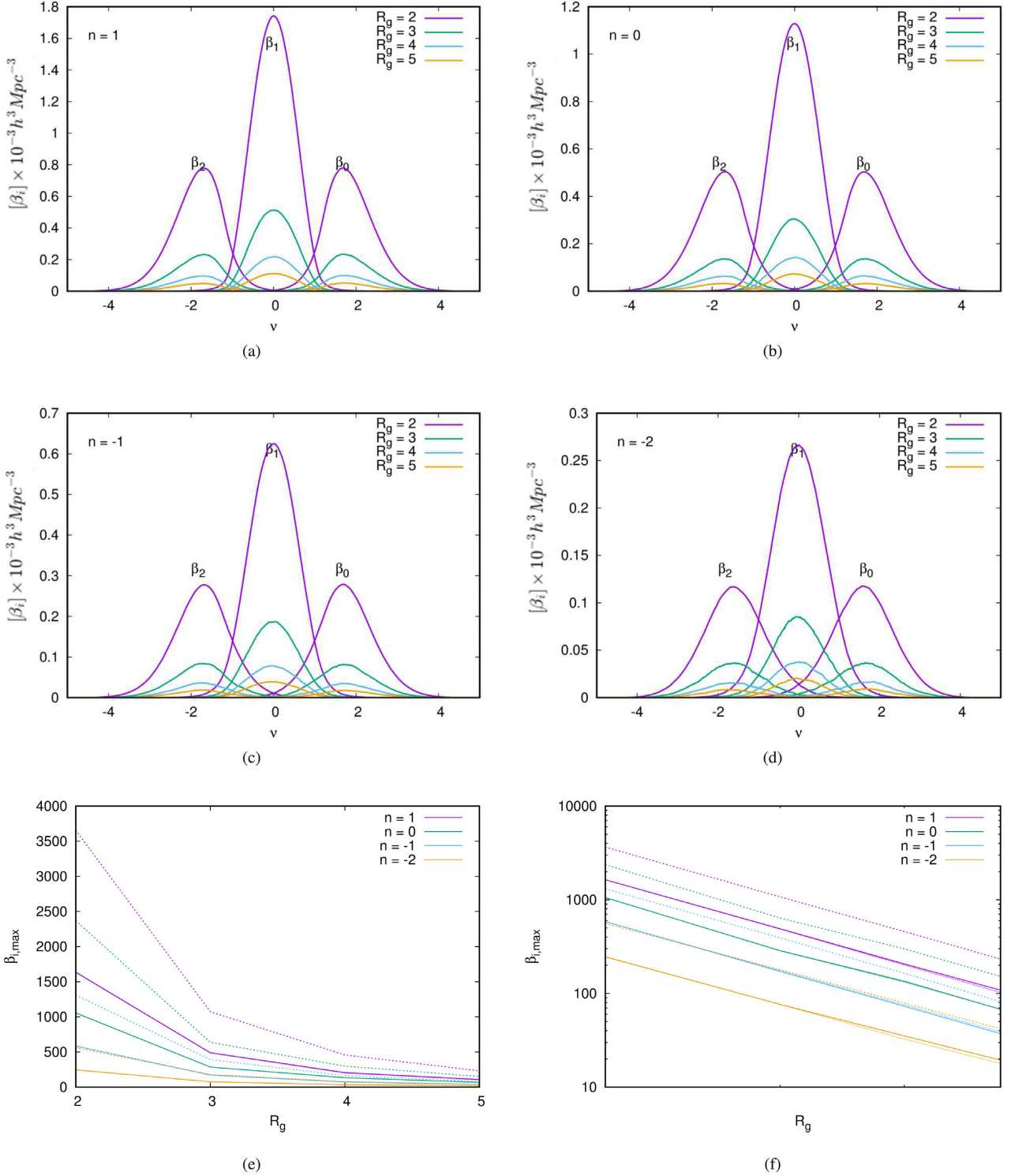


Figure 12. Dependence of the amplitude of Betti number curves on the filter radius R_g . Panels (a) to (d): Betti number curves for the $n = 1, 0, -1$, and -2 , respectively, where for each model, the field is smoothed by a Gaussian kernel of varying radii $R_g = 2, 3, 4$, and 5 . Panel (e): Graph presenting the amplitude of the Betti curves as a function of smoothing radius. Curves with the same colours represent the same model. The dotted curves are for β_1 , while the solid and the dashed curves represent β_0 and β_2 , respectively. Panel (f): Same as panel (e), but on a logarithmic scale.

7.5.1 Spectral dependence of β - and ζ -tracks

Figure 17 presents the β - and ζ -tracks for the various models. The left-hand panel plots the β -tracks and the right-hand panel

plots the ζ -tracks for the models. Recall that the β -tracks trace the quantity $(\beta_0, \beta_1, \beta_2)$ in a coordinate where the axis represent the individual Betti numbers. Similarly, ζ_1 and ζ_2 (see Section 7.5 for definitions) are various combinations of the Betti numbers and pro-

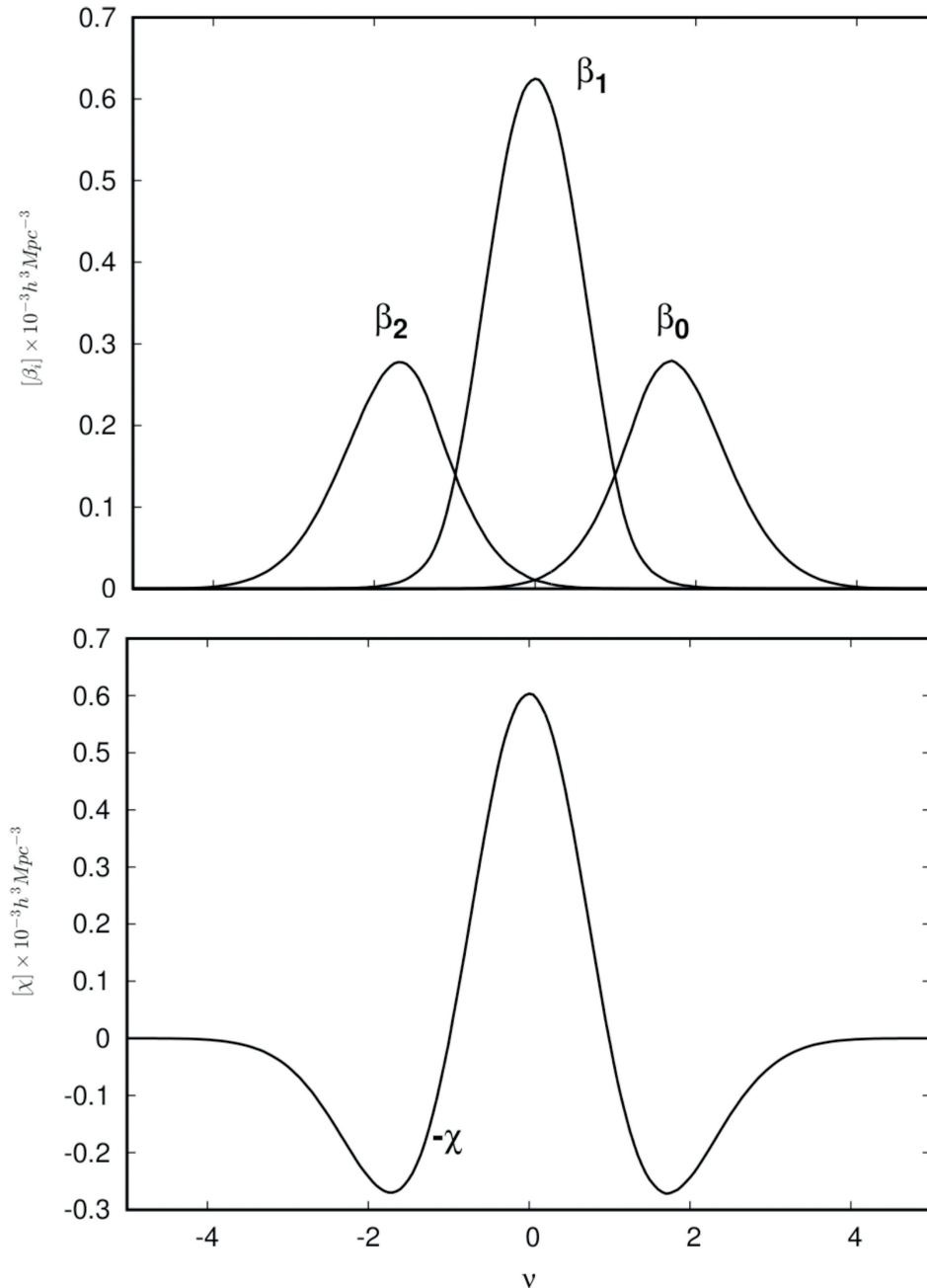


Figure 13. Betti numbers and Euler characteristic for a single model. Different topological entities dominate the different density threshold ranges in the Euler characteristic curve.

vide orthogonal information compared to the Euler characteristic. It is evident from the left-hand and the right-hand panels of the figure that both the quantities show a dependence on the spectral index.

8 PEAKS VERSUS ISLANDS

There is a telling distinction between *peaks* such as described by Bardeen et al. (1986), and the *islands* of our definition. A peak is the location of a local maximum of the function. An island is a single connected object. In general, an island may be marked by many peaks. However, at the higher density thresholds, when no

saddle points have yet been introduced in the manifold, there will be necessarily one peak per island. As the threshold is lowered, the number of peaks per island increases. As this happens, the manifold starts developing complex connectivity. This happens because the peaks merge through saddles, such that they are a part of a single connected component. As the density threshold lowers still further, such a connected component may exhibit more topological features, like a hole.

Figure 18 illustrates the above-mentioned phenomenon in 2D. The left-hand panel illustrates two separate peaks. They are composed of a single maximum. However, since they are trivially connected and isolated objects, they can also be classified as islands.

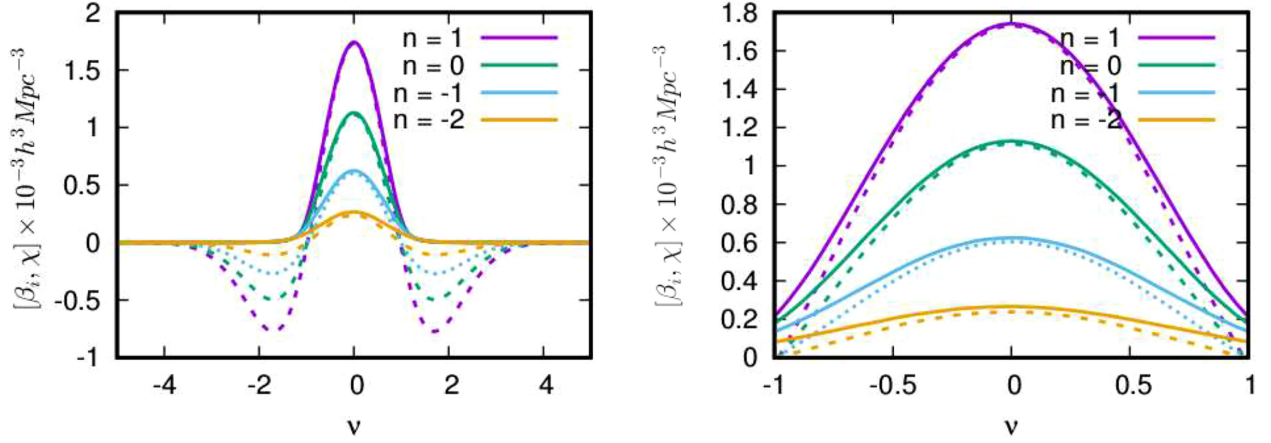


Figure 14. Comparison of relative contributions of β_1 versus Euler characteristic. As the spectral index lowers, the peak of the Euler characteristic has progressively lower amplitude compared to the β_1 curve.

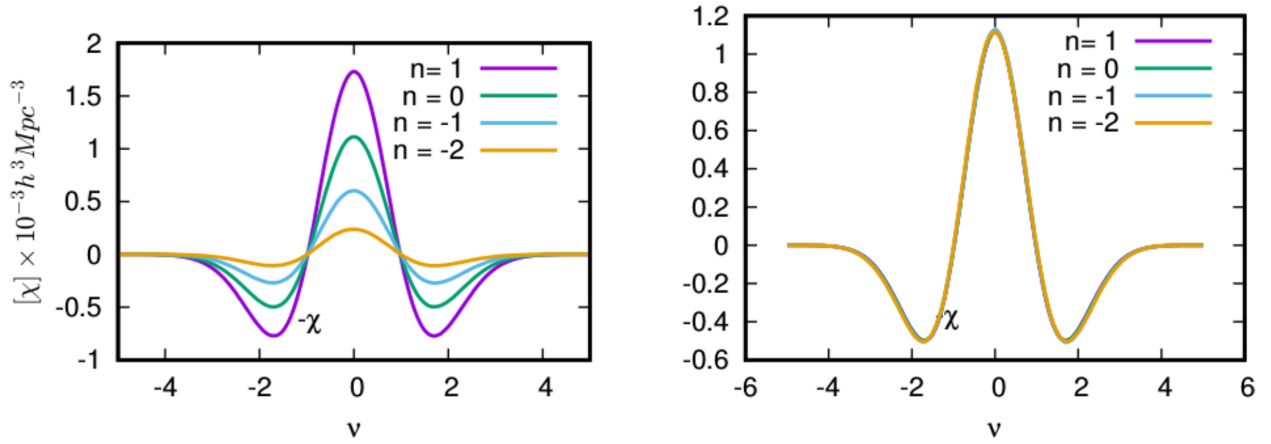


Figure 15. Scaling behaviour of the Euler characteristic curves for the power-law models. Left-hand panel: unscaled Euler characteristic curves for the power-law models. Right-hand panel: scaled curves for the same. The curves for the different models are scaled so that their amplitudes coincide. The scaled curves are indistinguishable from each other.

The middle and the right-hand panels illustrate islands with a more complex topology. In the middle panel, the island is a connected object and contains many peaks. This is due to the fact that as the density threshold lowers, saddle points are also introduced in the manifold, which connect two disjoint maxima to form a single connected component. In general, at sufficiently low thresholds, one may identify islands composed of multiple maxima and saddles, as is the case in the middle panel. In this context, we point out that the number of peaks per island, as a function of the density threshold, is a topological quantification of the strength of clustering of a model.

In the right-hand panel, the island encloses a loop as well. This is due to the introduction of a saddle point that connects the boundary of an already connected component forming a closed loop. Below, we investigate the model-dependent variation of the number of peaks and islands for the 3D Gaussian field models.

8.1 Peaks versus islands: the Gaussian case

As we noted earlier, *peaks* and *islands* (see definition above) are related yet different topological entities. In particular, peaks are a submanifold of islands. The former are the local maxima, while the latter grow depending on the density threshold ν . An island

may contain multiple peaks. In fact, as an island grows it might get arbitrarily complicated, acquiring tunnels and even voids, while always staying connected. But in the asymptotic limit of high ν , every island will contain only one peak. In this connection, it is instructive to examine the number distribution of critical points in general, and peaks in particular.

8.1.1 Number distribution of peaks (critical points)

Bardeen et al. (1986) derive the differential number distribution of peaks for Gaussian random fields as a function of the dimensionless density threshold ν (see appendix A for details):

$$\mathbb{N}_{pk}(\nu) d\nu = \frac{1}{(2\pi)^2 R_*^3} e^{-\nu^2} G(\gamma, \gamma\nu). \quad (78)$$

The function $G(\gamma, \gamma\nu)$ depends on the spectral parameter γ and height ν of the peaks. Bardeen et al. (1986) derived and specified a highly accurate fitting function for $G(\gamma, \gamma\nu)$, whose details are specified in appendix A. The parameters γ and R_* are combinations of several moments σ_j of the (filtered) power spectrum $P_s(k)$ (see appendix A). The spectral scale R_* is proportional to the smoothing scale R_s of the field, i.e. $R_* \propto R_s$. For power-law power spectra, γ and R_*/R_s depend on the spectral index n (see appendix A).

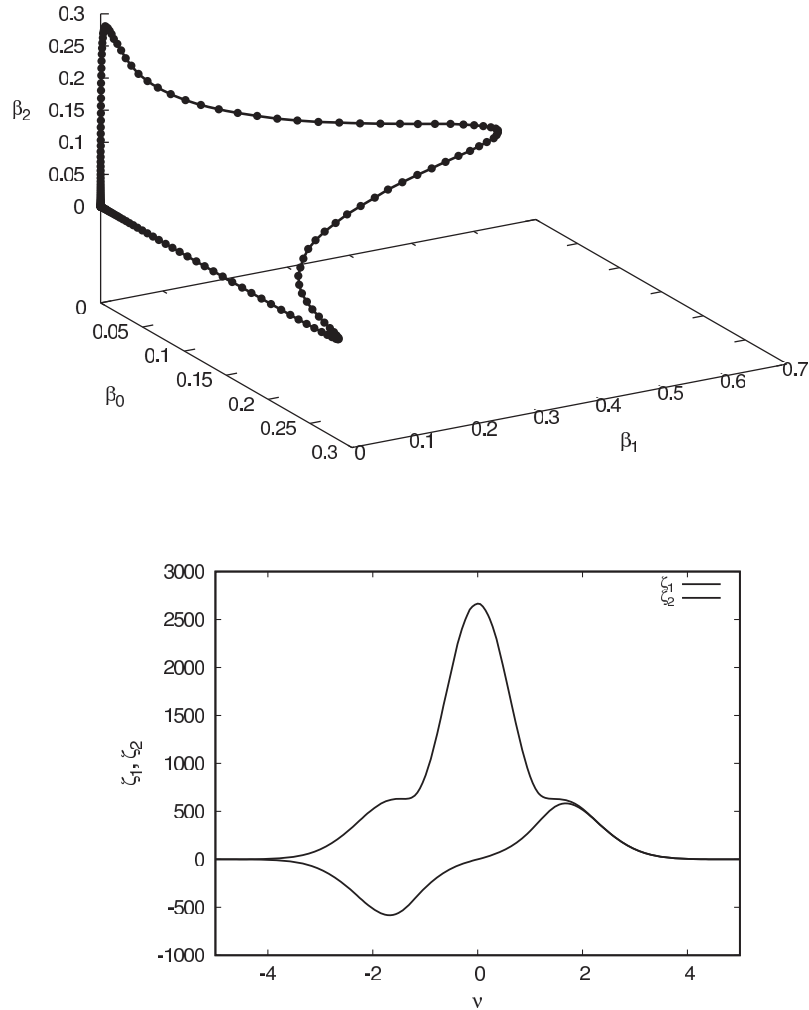


Figure 16. β -track (top) and ζ -track (bottom) for a typical Gaussian field model. They represent orthogonal information to the Euler characteristic, see the text for details.

For the total number of peaks $n_{pk}(\nu)$ in excess of a density threshold ν in the smoothed density field, we may compute the cumulative peak density,

$$n_{pk}(\nu) = \int_{\nu}^{\infty} \mathbb{N}_{pk}(\nu) d\nu. \quad (79)$$

From this, we may infer – analytically – that the total density of peaks $n_{pk}(-\infty)$ is given by

$$n_{pk} = 0.016 R_{\star}^{-3}. \quad (80)$$

In other words, in a Gaussian field one expects in total some 62 to 63 peaks per cubic volume R_{\star}^3 .

Figure 19 plots the number distribution of the critical points for the $n = -1$ model as computed from a single realization. One may notice that the distribution is symmetric about the mean density threshold. In particular, the distribution of maxima is symmetric with respect to the minima. Similarly, the distribution of the 2-saddles is symmetric with respect to the 1-saddles. To arrive at the expressions for the spatial density of all critical points – maxima, minima, and saddle points – one may follow a similar calculation as that for maxima (peaks). Along these lines, Pogosyan et al. (2009) arrives at approximations for the distribution function of the critical points, while Codis et al. (2013) even managed to obtain

expressions for mildly non-Gaussian fields. More recently, Cheng & Schwartzman (2015) specified the exact formula for the number distribution of critical points for the Gaussian case.

Figure 20 presents the distribution of critical points for the different power-law models. The left-hand panel plots the curves for maxima/minima, and the right-hand panel plots the curves for 2-saddles/1-saddles. As the spectral index decreases, the amplitude of the curves drop, accompanied by a broadening of the curves. This indicates that, as the spectral index decreases, there is a bigger overlap between the distribution of the various critical points as a function of the density threshold. The lower amplitude of the curves can be seen as the effect of a generally smoother field, as the spectral index decreases, which results in lesser number of critical points in the same given volume. As we will see shortly, these characteristics of the critical point distribution have a repercussion on the overall distribution of peaks and islands as well as their ratio.

8.1.2 Asymptotic behaviour of peaks and islands

For very high values of rms density threshold, as long as the peaks do not start merging, we expect the cumulative number density of peaks to be equal to the number density of islands. This is confirmed in Figure 21 where we present the cumulative

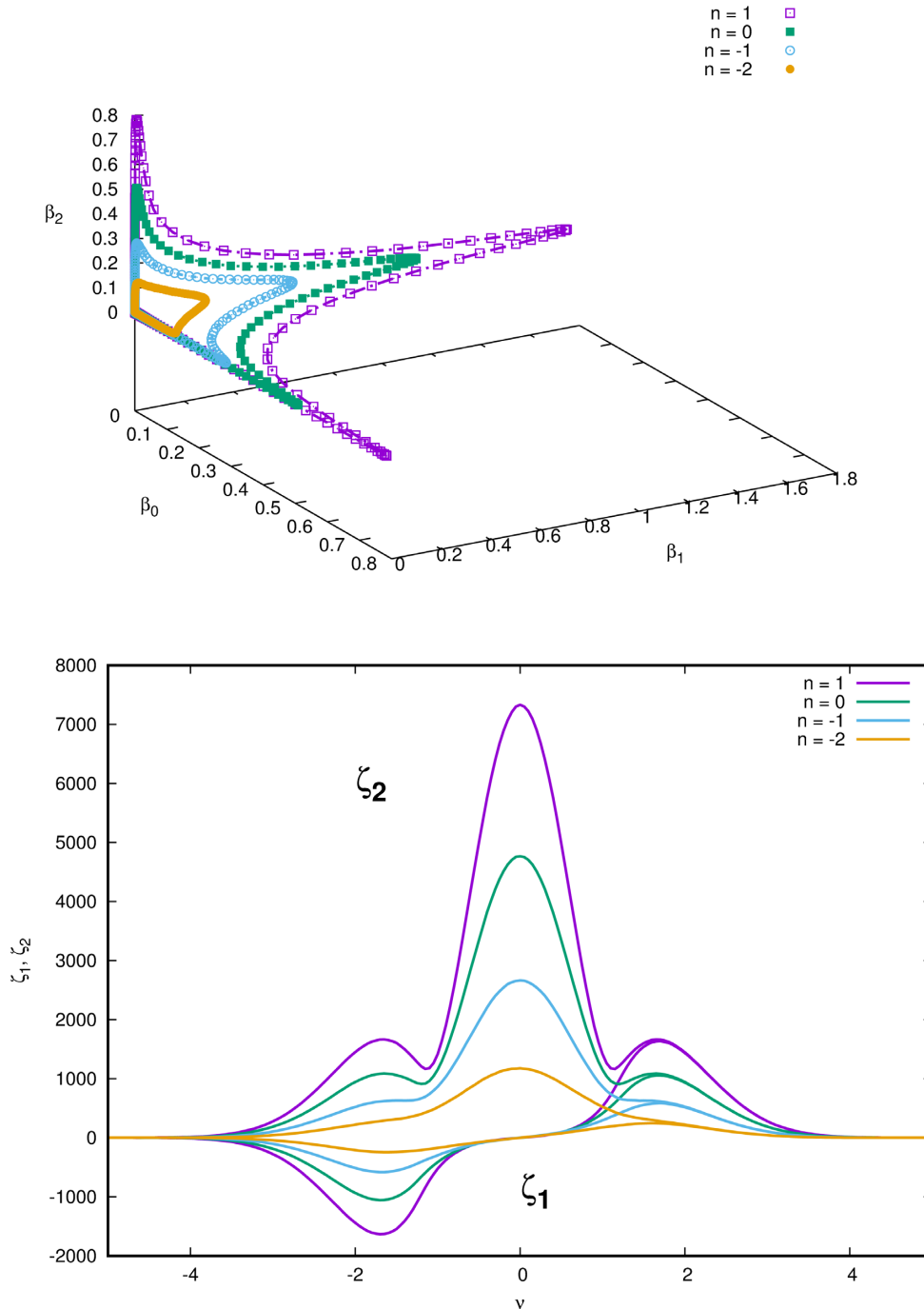


Figure 17. Betti tracks and (ζ_1, ζ_2) for the various power-law models as a function of the spectral index. There is a clear dependence on the power spectrum for the quantities.

number density of peaks n_{pk} and the number density of islands β_0 per unit volume, as a function of ν , for the $n = 0$ and $n = 2$ models in the left-hand and the right-hand panels, respectively. The cumulative number density of peaks equals the number density of islands asymptotically for very large rms density thresholds. The equivalence starts breaking down rapidly at thresholds even as high as $\nu \sim 4$. This is attributed to the fact that for high thresholds all the peaks represent disconnected regions almost surely (Bardeen et al. 1986), while they start connecting up and forming complex

topology as the threshold decreases. In general, one can also notice from both the panels that the distribution of peaks and islands show a characteristic dependence on the choice of the power spectrum.

For high values of spectral index, the small scales are dominant. In terms of the structures in the density fluctuation field, this means that the number of small scale peaks of high amplitude is large. They are also separated by low-density saddles. There is no discernible large-scale feature in the density field. As the index of the power spectrum decreases, the power shifts to large scales. The small-

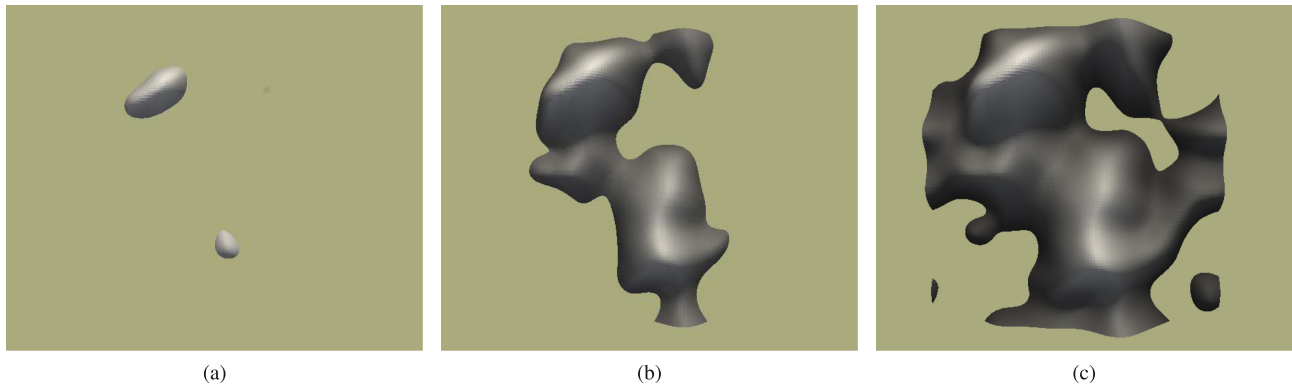


Figure 18. Figure illustrating the difference between peaks and islands. The left-hand panel illustrates two peaks. They are composed of a single maximum. However, since they are also trivially connected and isolated objects, they double up as islands also. The middle and the right-hand panels illustrate islands with a more complex topology. In the middle panel the island is a connected object and contains many peaks. In the right-hand panel, the island encloses a loop as well.

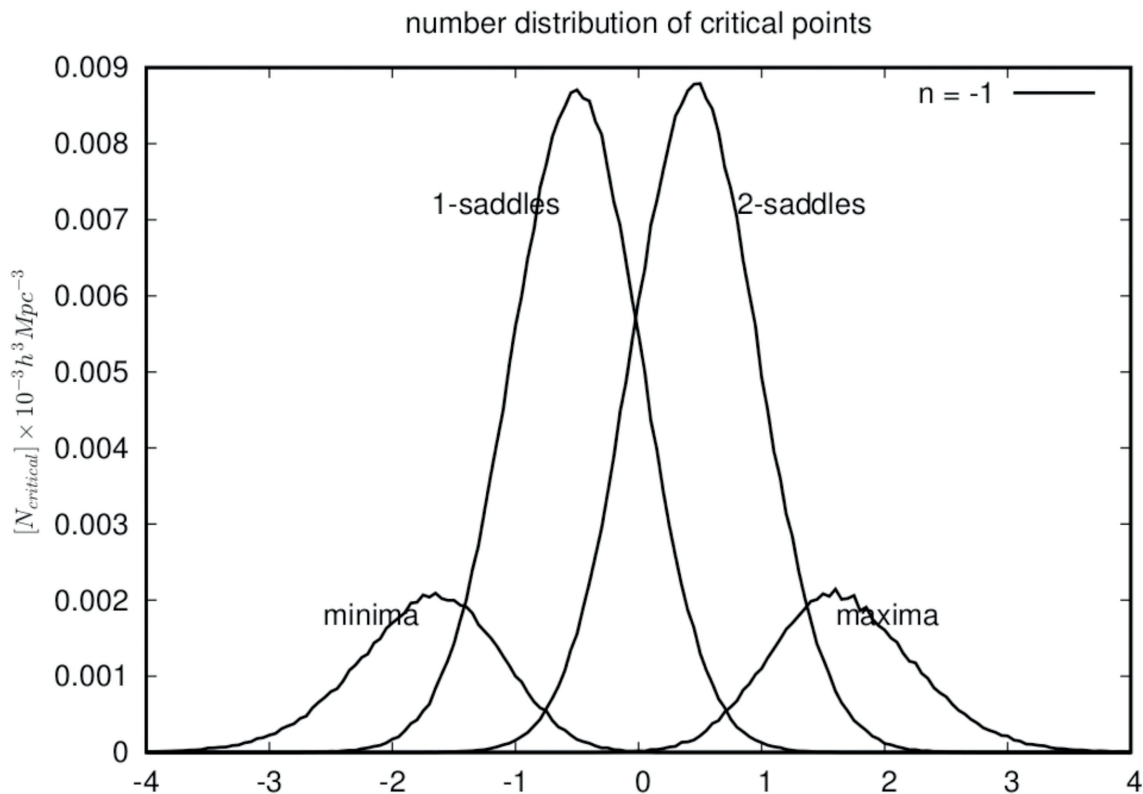


Figure 19. Number distribution of critical points for the $n = -1$ model. Critical points with different indices are dominant over different ranges, but there is a strong overlap between them as a function of the density threshold.

scale peaks are separated by saddles occurring at relatively high-density thresholds. It is also accompanied by a decrease in the amplitude of the global maximum of the field. As noted earlier, this is because the variance of the density field in the box decreases with decreasing spectral index: $\sigma_0 \propto R^{-(n+3)}$. This phenomenon is reflected in the curves of the number distribution of peaks in the top-left panel and top-right panels of the Figure 22. For a larger n , the number distribution of peaks attains its maximum at a higher density threshold compared to a smaller n . For the $n = 1$ model, the maxima is located as high as $\nu = 2$. In contrast, for the $n = -2$ model, the maximum is located at $\nu \sim 1$, and there are significant number of peaks even below $\nu = 0$. As noted earlier, this is a direct reflection

of the fact that there are progressively more number of peaks for lower thresholds, as the spectral index decreases (Bardeen et al. 1986). In contrast, in the same figure, the location of the maxima of β_0 curves shows a negligible dependence on the value of spectral index.

8.2 Distribution of peaks and islands: a comparison

The top left-hand and top right-hand panels of Figure 22 plots the number distribution of peaks and the Betti numbers for the 3D Gaussian fields. The left-hand and the right-hand panels plot the specific number distribution of peaks and the zeroth Betti number

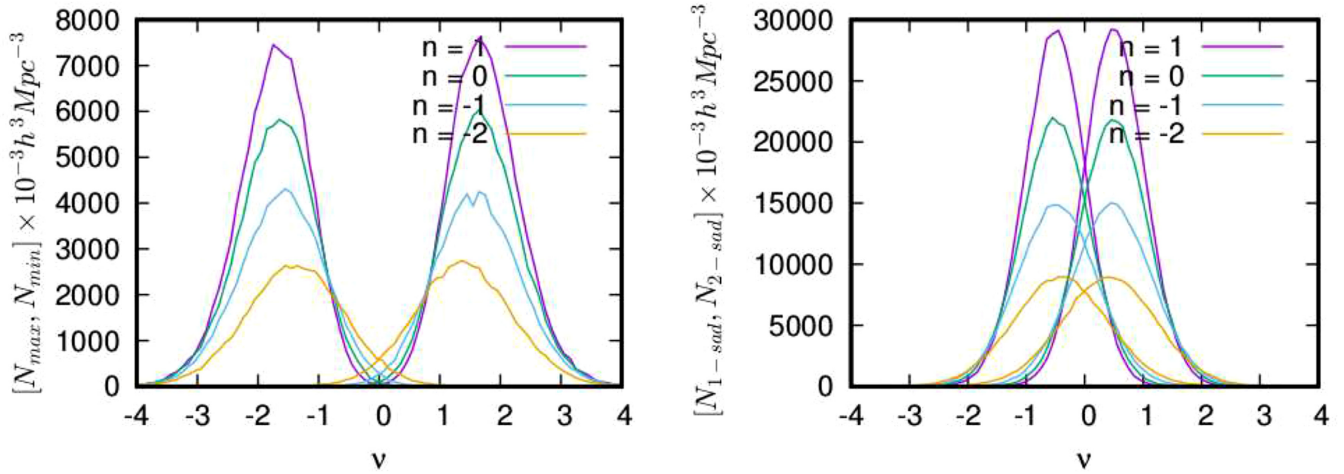


Figure 20. Number distribution of critical points as a function of the spectral index. The left-hand panel plots the distribution of the maxima/minima as a function of the spectral index and density threshold. The right-hand panel plots the same for 1- and 2-saddles.

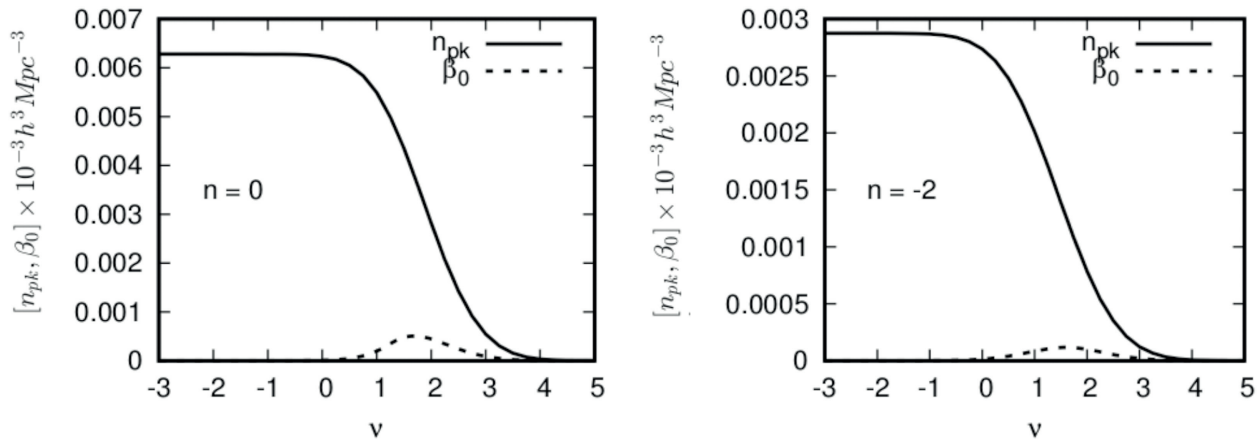


Figure 21. Cumulative number distribution of peaks and the distribution of islands (zeroth Betti number) for comparison as a function of density threshold. The left-hand panel presents the graphs for the $n = 0$ model, and the right-hand panel plots it for the $n = -2$ model.

β_0 , respectively. The curves show the behaviour of these quantities as a function of the dimensionless density threshold ν . The curves for both quantities reveal a largely similar behaviour as a function of the density threshold ν , and in their dependence on the spectral index of the power spectrum.

Nonetheless, we identify subtle properties that manifest themselves in distinct differences when we assess the number of peaks – or saddles and minima – that populate a given island complex. From the top panels of Figure 22, it is evident that as the spectral index decreases, the location of peaks shifts towards lower density thresholds for both the quantities as the spectral index decreases. This effect is strong for the cumulative distribution of peaks, but small for β_0 . We also note a substantial difference in amplitudes of the distribution functions. The (cumulative) number density of peaks therefore differs substantially from that for the zeroth Betti number, indicating that they measure different features associated with the topology of the density distribution.

The bottom left-hand panel of Figure 22 presents the cumulative number density of peaks for the different models. The bottom right-hand panel plots the ratio of the cumulative peak density and the number of islands β_0 . This quantity is an indicator of the

average number of peaks of height ν and higher, which populate an island at ν . The average number of peaks per island shows a characteristic dependence on the power spectrum. As expected, for high-density thresholds the number of peaks per island approaches unity. While the density thresholds have a positive value, lower spectral indices correspond to a higher number of peaks per island. A major reason for this is that Gaussian fields with a lower spectral index contain larger coherent features. Net, this lower number of large islands contains a higher number of peaks (and other singularities).

In this context, we may also identify a subtle complementary effect. The interior structure of each island is marked and largely determined by the spatial distribution of peaks and 2-saddles. In general, the number density of these behave differently (Bardeen et al. 1986; Pogossyan et al. 2009). This can be immediately inferred from their distribution functions in Figure 20. Not all 2-saddles at a given density threshold are therefore responsible for bridging two previously disconnected peaks. Moreover, the fraction of 2-saddles that join two isolated objects is, in general, a function of the density threshold (also see Feldbrugge & van Engelen 2012 for a semi-analytic approximation describing this). At low

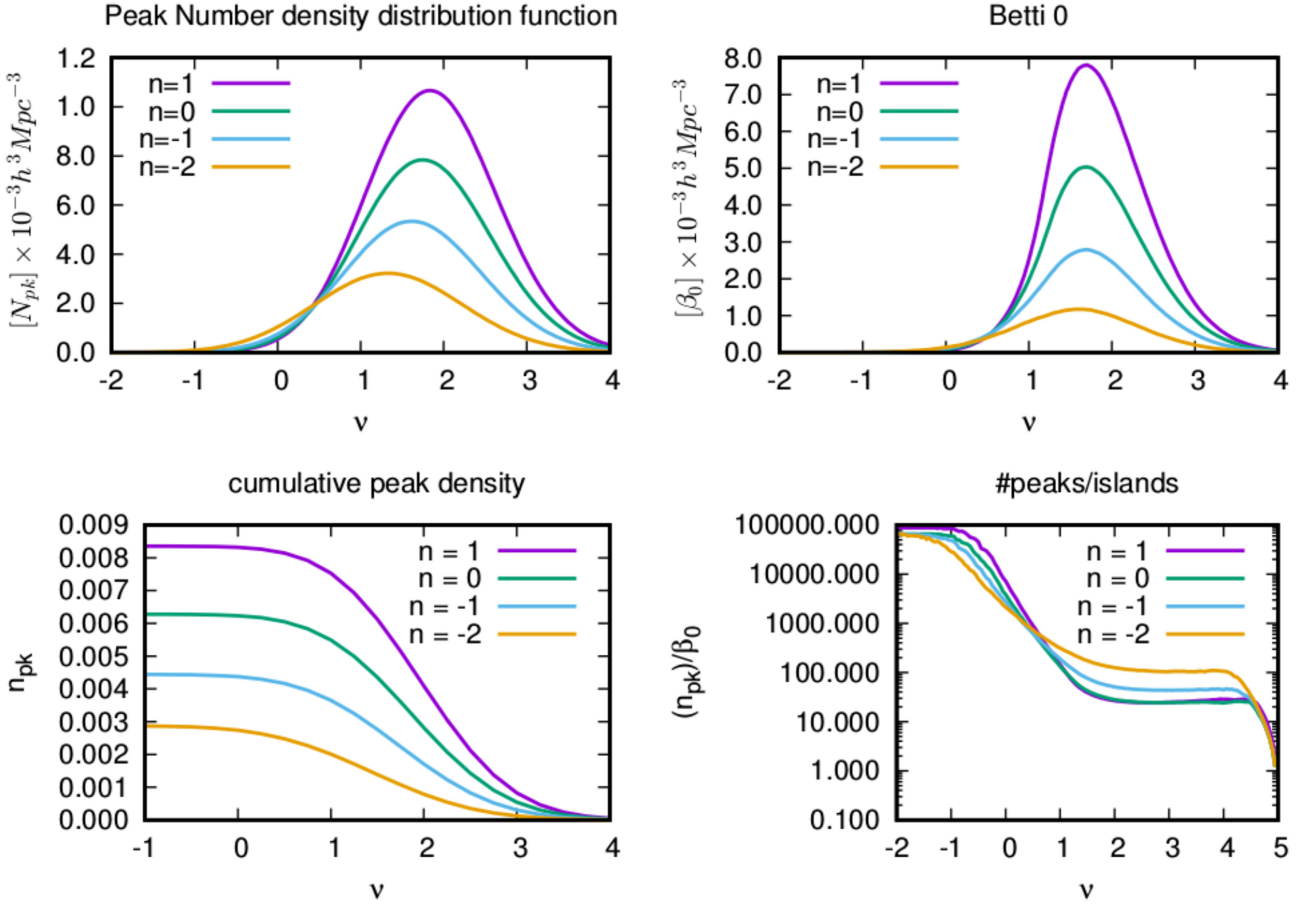


Figure 22. Figure illustrating the relation between peaks and islands. The top left-hand panel plots the number distribution of peaks, N_{pk} . The top right-hand panel plots the number of independent islands as denoted by β_0 . The zeroth Betti number counts the number of isolated islands at a particular density threshold. The curves for both the quantities show a characteristic dependence on the index of the power spectrum. The location of the maximum shifts towards lower density thresholds considerably for the number distribution of peaks as the spectral index decreases. The location of the maximum for the β_0 curve remains unaffected as the spectral index changes. The bottom left-hand panel plots the cumulative number density of peaks as a function of the spectral index. It increases with increasing spectral index, which is related to the fact that as the power shifts to smaller scales for larger spectral index, it is accompanied by larger number small-scale peaks packed in a given volume. The bottom-right panel plots the cumulative number of peaks per island as a function of power spectrum and density threshold v . For very large values of v there is one peak per island irrespective of the spectral index. As the density threshold decreases, this number has a characteristic dependence on the spectral index.

densities we therefore see an increasing fraction of them involved in establishing connections between two or more already connected peaks, thereby forming loops or tunnels (Edelsbrunner & Harer 2010; Pranav et al. 2017), and the cracked appearance of the island.

The spectral dependence of the peak population of islands reverses at median and low field densities. As borne out by Figure 22 at underdense field values we observe a steep rise in the number of peaks per island as the density decreases. It reflects the merging of an increasingly larger fraction of the volume into an ever larger connected and percolating complex as individual disconnected overdense islands start to connect. They merge into a single or a few volume percolating regions, leading to a field topology attaining a *Sponge-like* character (see Section 3.3.2). As we descend to lower densities, we therefore see the absorption of the remaining peaks into the remaining percolating region(s). It results in the observed steep rise of the number of peaks per island.

As we described extensively in Section 7.2, Gaussian fields with a lower spectral index retain a slightly higher number of disconnected islands at low-density thresholds than those with higher spectral index (also see Figure 7). Meanwhile, as a consequence of the

dominance of high frequency modes in high spectral index Gaussian fields, they are marked by a considerably higher number of peaks (see Figure 22, lower left-hand panel). It translates into the steeper rise of the ratio n_{pk}/β_0 for Gaussian fields that have a higher spectral index seen in Figure 22 (right-hand panel).

9 MINKOWSKI FUNCTIONALS OF THE MODELS

The left-hand column of Figure 23 presents the unnormalized (original) graph of the Minkowski functionals for the power-law models. The graphs are averaged over 100 realizations. The quantities are plotted as a function of the density threshold v . The fractional volume Q_0 is invariant with respect to the choice of the power spectrum. This is to be expected, because the first Minkowski functional simply takes the form of the error function. All the other functionals show a systematic dependence on the choice of the power spectrum. The amplitude of the graphs of the area functional, the integrated mean curvature functional, and the

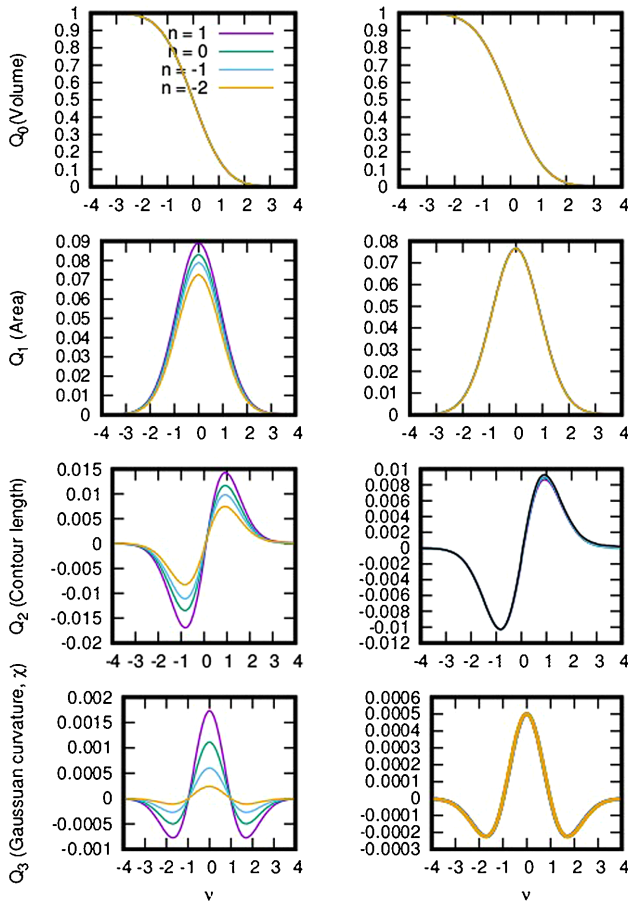


Figure 23. Minkowski functionals of the power-law models. From the top to the bottom, we present the volume, area, integrated curvature, and Gaussian curvature, or the Euler characteristic. The left-hand column presents the unscaled version, while the right-hand panel presents the scaled version. All the functionals are normalized by the total volume of the simulation box. The volume functional is invariant with respect to the choice of the power spectrum. The amplitude of the area, contour length, and Euler characteristic show a dependence on the choice of the power spectrum. The shape of the scaled curves is indistinguishable across the models. This implies the shape of the Minkowski functionals has no dependence on the spectral index.

Euler characteristic decreases monotonically with the decrease in the index of the power spectrum.

The right-hand column of the Figure 23 presents the rescaled Minkowski functional curves. The graphs for the rest of the power-law models have been scaled to the amplitude of the curve of the $n = 0$ model. The shape of the rescaled graphs falls neatly on top of each other. This indicates that the shape of the Minkowski functional curves is independent of the choice of the power spectrum. This observation is in line with Equation (66). The dependence on the choice of the power spectrum comes in only through the amplitude term. This dependence is parametrized in terms of λ , which is a function of the correlation function, or equivalently, the power spectrum.

That the shape of the Minkowski functional curves is independent of the choice of the power spectrum is an important observation, when seen in comparison to the shape of the Betti number curves, which show a characteristic dependence on the choice of the power spectrum. We present a detailed analysis of the Betti numbers with respect to the Euler characteristic in Section 7. This indicates that

the Betti numbers are potentially more discriminatory than the Minkowski functionals, an observation we have already established in Park et al. (2013).

9.1 Minkowski functionals as shapefinders

Recall that the ratio of the Minkowski functionals are simplistic indicator of the morphological properties of manifold, given by (Sahni et al. 1998; Sheth et al. 2003; Shandarin, Sheth & Sahni 2004) (also see Schmalzing et al. (1999) for the relation to isoperimetric inequalities and Blaschke diagrams):

$$H_1 = Q_0/Q_1; \quad H_2 = Q_1/Q_2; \quad H_3 = Q_2. \quad (81)$$

For example, a high surface area to volume ratio indicates a more pancake like morphology of structures. The reverse indicates a more filamentary morphology. Figure 24 presents the shapefinders for the models in the top panel, and their inverse quantities in the bottom panel. In the left-hand column, we present H_1 and H_1^{-1} , in the top and the bottom panels, respectively. The middle and the right-hand columns present $H_2(H_2^{-1})$, and $H_3(H_3^{-1})$, respectively. The curves are drawn with respect to the dimensionless density threshold ν .

All three quantities show a characteristic dependence on the choice of the power spectrum, more clearly in the inverse quantities for H_1 and H_2 , and directly for H_3 . The curves for the lower power spectra increase more steeply towards the extremes of the density threshold, and flatten out as the threshold moves to further extremes. For all the models, the surface area to volume ratio is high for high-density thresholds. It indicates that the structures are more flattened for high thresholds. Interesting is the sharp rise in the value for the negative spectra. This indicates that at very high thresholds, the structures in the $n = -2$ model are the most flat. This ties in with the observation that for the $n = -2$ model, the large-scale structures have significant power, giving rise to the overall flattened characteristics of the density field. The large structures are a consequence of significant powers at those scales.

In summary, the Minkowski functionals characterize the geometric properties of the manifold predominantly. The connection to topology comes through the Euler characteristic. Hence, the Minkowski functionals maybe seen as complimentary to the topological descriptors such as the Betti numbers. The Minkowski functionals, together with the information on the homology of a manifold, provide a richer and more comprehensive morphological and topological information about the manifold.

9.2 Betti numbers versus Minkowski functionals

As we learnt in the previous sections, the Betti numbers are topological quantities. They measure topology by assessing the number of independent holes in the different dimensions. On the other hand, the Minkowski functionals are primarily morphological measures, the exception being the Minkowski functional Q_3 , or the Euler characteristic, χ . The first three Minkowski functionals are associated with the volume (Q_0), surface area (Q_1), and the integrated mean curvature length (Q_2) of the manifold. However, an important question one may ask is if the Betti numbers and the Minkowski functionals convey different information about the manifold characteristics. With a view to investigate this, we assess the correspondence between the Betti numbers and the Minkowski functionals.

Figure 25 presents the Betti numbers plotted against the various Minkowski functionals. The top left-hand panel of the figure plots β_0 on the vertical axis against Q_0 on the horizontal axis, and

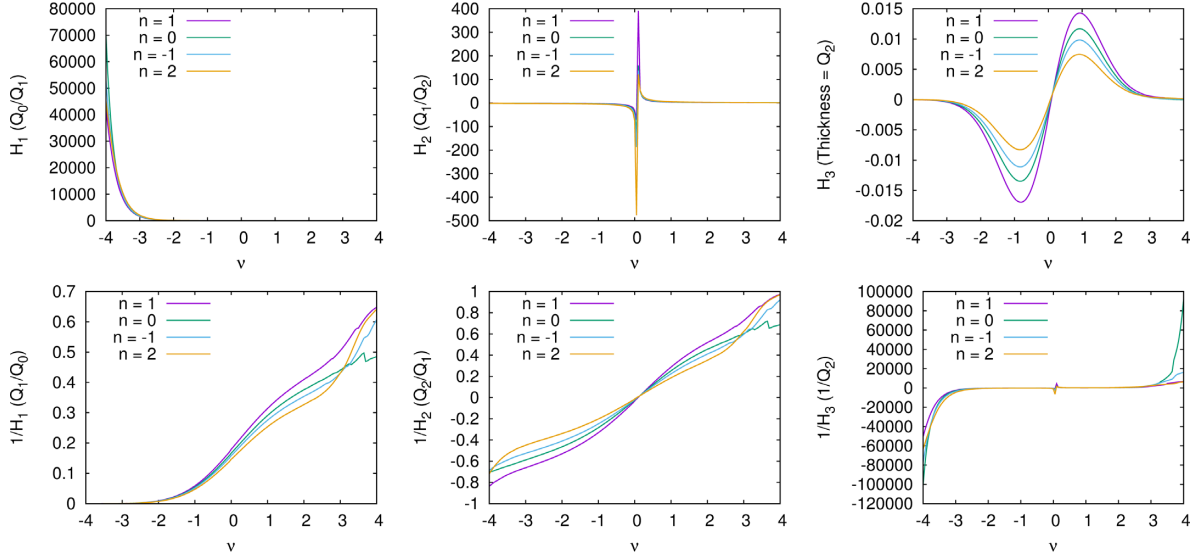


Figure 24. Ratios of Minkowski functionals. Left-hand panel: The ratio Q_1/Q_0 denoting the ratio between the total occupied volume and the total surface area corresponding to the occupied volume. Middle: The ratio Q_2/Q_1 denoting the ratio between the total length of contours and the total surface area. Right-hand panel: The ratio Q_2/Q_0 denoting the total length of contours per unit volume occupied. The curves are drawn with respect to the dimensionless density threshold ν . For the bottom row, the numbers for high-density thresholds, are not reliable, due to division by small numbers.

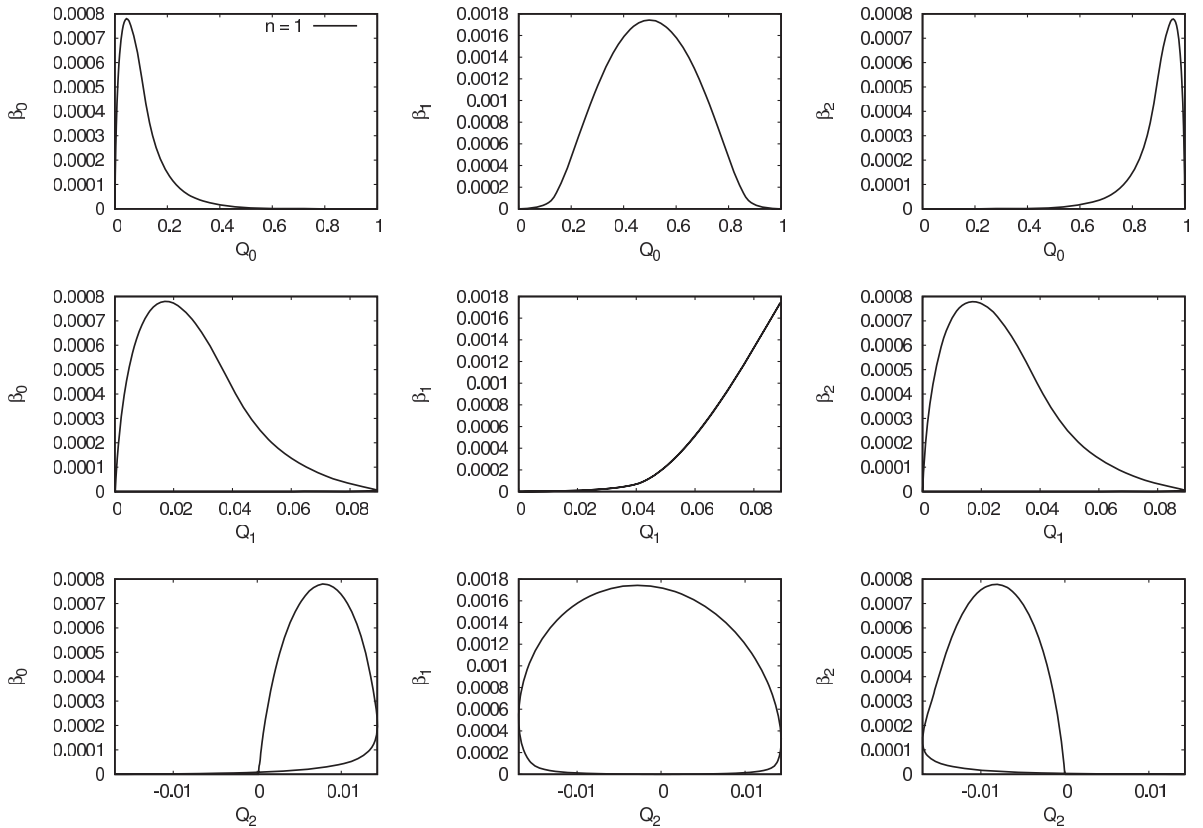


Figure 25. Betti numbers versus the Minkowski functionals.

so on. We notice that almost all the pairs of quantities exhibit a degeneracy. For example, in the top left-hand panel, we notice that there are two values of Q_0 for which the value of β_0 is the same. The exception is the peak of the curve, at which β_0 is associated with a unique value of Q_0 . The only exception to this trend of

degeneracy is the middle panel of the middle row, where we plot β_1 against Q_1 . The curve is monotonic indicating that β_1 and Q_1 behave in a similar fashion. In general, a monotonic curve between any two plotted quantities indicates a similar behaviour of the quantities.

The ratio of the Betti numbers to the Minkowski functionals is another interesting quantity to analyse, particularly in certain cases, where they can be readily associated with a particular features of the manifold. For example, the ratio β_0/Q_0 represents the number of isolated objects per unit occupied volume. Note that the occupied volume is different from the total volume of the manifold. The total volume is a constant, while the occupied volume is a function of the density threshold. Similarly, the ratio β_1/Q_1 indicates the number of independent tunnels per unit surface area. This may be regarded equivalent to the information on the genus density of the manifold.

Figure 26 presents the ratio of the various Betti numbers to the various Minkowski functionals as a function of the density threshold ν . The plots are presented for the different power-law models. We notice a dependence of the quantities on the choice of the spectral index. It is important to note that a constant, or a monotonically increasing or decreasing curve indicates that quantities have a simple dependence on each other. We notice that none of the pair of quantities exhibit a monotonic ratio. This indicates crudely that the Betti numbers and the Minkowski functionals behave differently from each other in general.

10 TOPOLOGY OF THE LCDM MODEL

In this section, we briefly discuss the topology of the LCDM model. This is pertinent, since the LCDM model is the standard model of cosmology. However, recall that the LCDM model is also characterized in terms of a spectral index, which is a running function of the wavelength. This is unlike the power-law models, where the spectral index is constant. Due to a corresponding description through the index of the power spectrum, for both the LCDM and the power-law models, it makes sense to compare the characteristics of the power law and the LCDM models.

Figure 27 presents the Betti curves for the LCDM model (drawn in black). We also present the curves for the power-law models with spectral index $n = 0, -1, \text{ and } -2$ models. Here we compare the spectra at a scale of $R_f = 2 h^{-1}$ Mpc, with an effective index $n_{\text{eff}} \approx -2$. Our topological analysis appears to yield Betti number curves that lie in between those for power-law spectra with $n = -1$ and $n = -2$, tending more towards the first.

For a complete comparison, we need to take into account that over the range of the simulation box, the LCDM spectrum is represented by frequencies running from Nyquist frequency to fundamental frequency (see Figure 4, Section 6.2). Hence, the effective index at the frequencies resampled in the realized LCDM Gaussian density fluctuation field varies from $n_{\text{eff}} \sim -2.5$ to $n_{\text{eff}} \sim -0.5$. The combination of these fluctuations appear to lead to a Betti number topology that resembles best that of a power-law power spectrum close to $n = -1$. In order to get more insight in how these topological synergy between different modes works, we need to invoke the concept of persistence. For this we refer to the upcoming accompanying study Pranav et al. (in preparation).

11 DISCUSSION AND SUMMARY

In this study we present a largely numerical study of the topology of Gaussian random fields on the basis of homology, specifically in terms of Betti numbers. Homology describes the topological structure of a manifold in terms of the topological features – or topological holes – it contains, whereby it concentrates on their boundaries. These and other concepts from algebraic topology provide a fundamental and rich framework for a quantitative

characterization of the shapes and connectivity of structures in the cosmological mass distribution. An important aspect is the intimate relationship with the Euler characteristic, which is equal to the alternating sum of the Betti numbers. Their individual assessment therefore enables us to understand the role and contribution of the various structural components in establishing the overall topology of the cosmic mass distribution encapsulated in the Euler characteristic. This can be obtained from the decomposition of the well-known curve for the genus or Euler characteristic, as a function of superlevel threshold, into separate curves for the individual Betti numbers.

The topology of Gaussian random fields functions as key reference against which topological measures of the cosmic mass and galaxy distribution in more advanced evolutionary stages should be assessed. In cosmology, the topological and geometric structure of 2D and 3D Gaussian random fields has been extensively analysed in terms of genus, the Euler characteristic, and Minkowski functionals. An aspect of importance for the use of Gaussian random fields as reference point is the existence of closed analytical expressions for the statistical distribution of their Euler characteristic and Minkowski functionals (Adler 1981; Bardeen et al. 1986; Weinberg et al. 1987; Tomita 1993; Schmalzing & Buchert 1997). In fact, the analytic expressions for the mean of the Euler characteristic and Minkowski functionals of Gaussian random fields belong to an extensive family of such formulae, all emanating from the so-called *Gaussian kinematic formula* or GKF (Adler & Taylor 2010, 2011; Adler et al. 2018). While hardly known in the cosmological literature, given its central role for our assessment and understanding of the topology and morphology of Gaussian fields, we devote an extensive discussion on its formulation and ramifications in Section 4. Most relevant for our purpose is the observation that it is not possible via this GKF route to establish similar closed analytical expressions for Betti numbers and persistence. While other routes might be feasible, it establishes the principal motivation for the numerical approach used here.

This study is part of a series of papers that seeks to extend this to the richer language of homology, with the second part (Pranav et al. 2018) discussing the description of the multiscale topological aspects of Gaussian fields in terms of persistence (Edelsbrunner & Harer 2010; Robins 2013; Robins 2015; Pranav et al. 2017). An accompanying upcoming article (Feldbrugge et al., in preparation) contains a mathematical analysis and formalism for the description of Gaussian random field homology.

11.1 Gaussian field Betti numbers: properties

Our statistical study of 3D Gaussian field homology consists of Betti number curves $\beta_0, \beta_1, \text{ and } \beta_2$ as a function of density field threshold ν of the corresponding superlevel set of a Gaussian field realization. The curves are averaged over 100 field realizations for each separate power spectrum.

In Section 5 we computed the Betti numbers using the Bendich et al. (2010) algorithm, an optimal and exact algorithm for computing all Betti numbers of a discretely sampled image on a cubic grid. It starts with a slight deformation of the grid, the calculation of the corresponding unique simplicial complex defined by the grid-point distribution, and the subsequent computation of Betti numbers of superlevel sets of the field – for a range of density thresholds – via the construction and simplification of a boundary matrix of the simplicial elements.

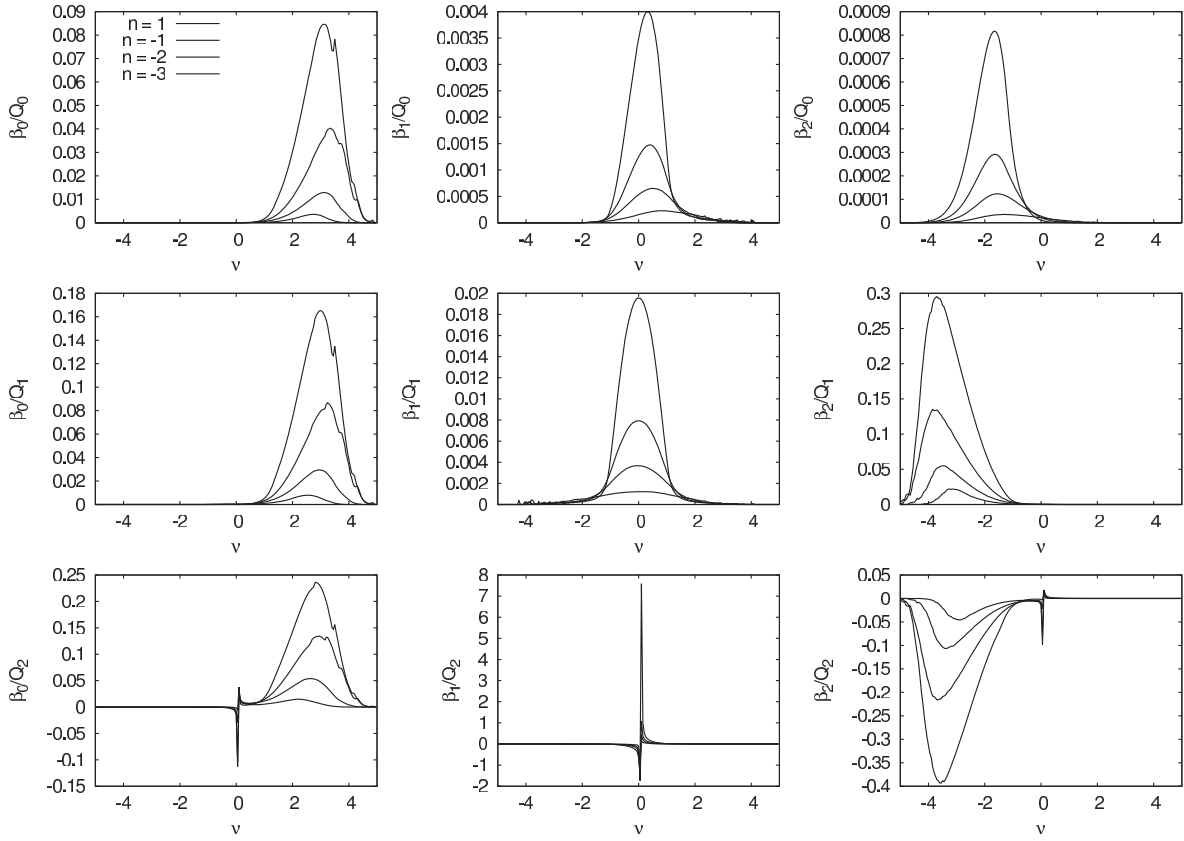


Figure 26. Ratio of Betti numbers to the various Minkowski functionals. The graphs as plotted for a range of density threshold.

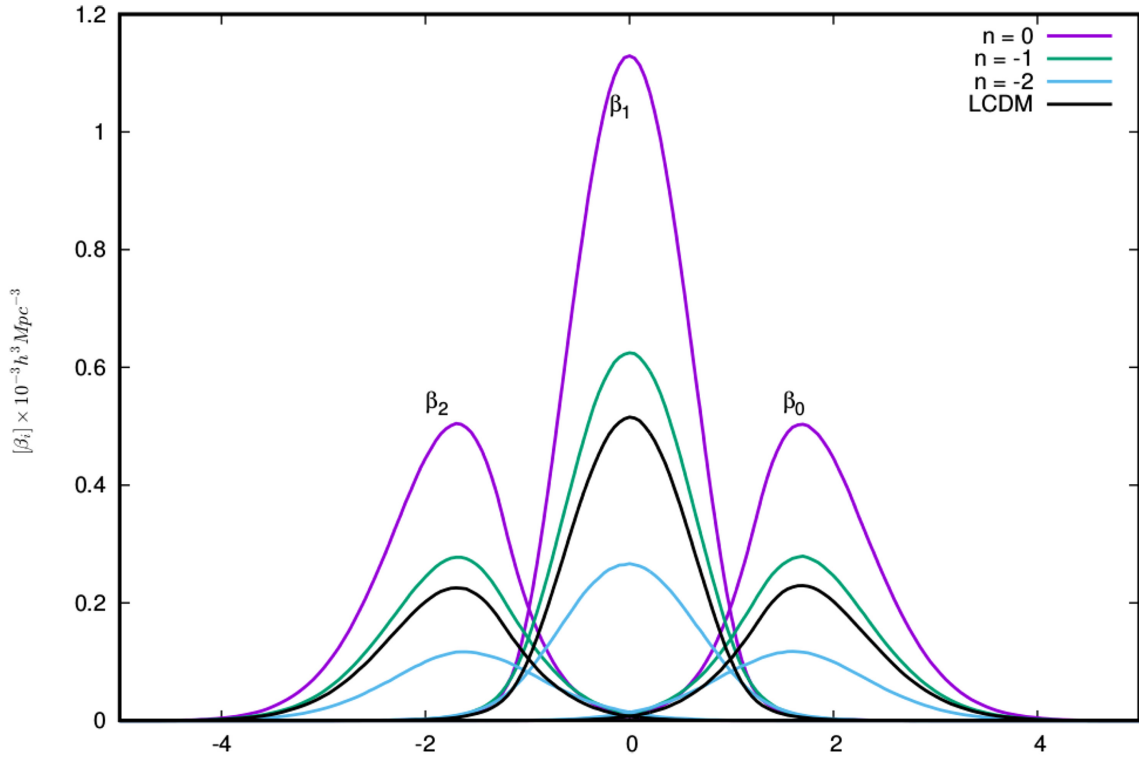


Figure 27. Betti numbers of the LCDM model (in black). Alongside are plotted the curves for the power-law models, $n = 0, -1,$ and -2 . The curves for the LCDM model are closest to the $n = -1$ model.

The Gaussian fields for which we evaluate the homology measures are 3D in nature and consist of two classes. The first family of realizations is a series of pure power-law power spectra, with the intention to assess systematic trends as the power shifts from dominant high frequency modes to low frequency modes. We also measure the Betti numbers in Gaussian fields with an LCDM power spectrum.

11.1.1 Gaussian fields: topological components

At extreme low- and high-density values, the topology of Gaussian fields is dominated by a single class of features. At very high density levels these are islands and thus fully specified by β_0 , defining a predominantly *Meatball-like* topology. The same is true at very low density levels, where the topology is distinctly *Swiss-cheeselike*, exclusively dominated by cavities and thus entirely specified by β_2 .

At more moderate levels, for $|\nu| \lesssim 2$, the topology attains an increasingly *Sponge-like* character. In these regimes at least two Betti numbers are needed to describe the topology of the superlevel manifolds. On the lower density side, the topology is dominated by β_2 and β_1 . It reflects a pattern of isolated cavities and agglomerates of density troughs interspersed by tunnels and loops. On the higher density side, the topological signal consists mostly of β_0 and β_1 .

The corresponding spatial pattern is that of isolated islands and large agglomerates of islands, connected by bridges/loops, and infused and punctured by numerous tunnels. In a relatively narrow density range around the mean density, for $|\nu| \lesssim 0.1 - 0.2$, we even observe the simultaneous existence of all three topological features, cavities, islands, and tunnels. In that regime, all three Betti numbers are needed to quantify the Gaussian field topology.

Also interesting is the finding that the topological identity at the median density level, at $\nu = 0$ for Gaussian fields, is not exactly – i.e. ideally – sponge-like. At that level, we see the presence of an equal number of islands and cavities as $\beta_0 = \beta_2$ at $\nu = 0$. Conventionally, it is assumed that all overdense regions have merged into one percolating complex, interlocking with an one equivalent underdense ‘ocean’. While this is the definition for a pure sponge-like topology, we find that in general this is not even the case for Gaussian fields. The topology at median levels is determined by a few – disconnected – overdense complexes, intertwined with a few underdense ones. The dissection of the genus curve into the contributing Betti curves leads to new insights on to this issue.

11.1.2 Betti numbers versus power spectrum

An important aspect of Betti numbers of Gaussian fields is that they are sensitive to their power spectra. In other words, they reflect the nature of Gaussian random fields. The shifting prominence from large wavelength modes to that of short wavelength modes has a significant impact on the resulting topology. This is entirely different from the behaviour of the Euler characteristic, whose curve is known to be entirely independent of the nature of the underlying power spectrum (see Equation 24) (Adler 1981; Bardeen et al. 1986; Weinberg et al. 1987).

This aspect of Gaussian field topology is most clearly revealed in the scaled Betti number curves – scaled with respect to the maximum of the β_1 curves, i.e. with respect to the maximum number of tunnels. While the spectral insensitivity of the Euler characteristic makes it a highly robust measure for testing the level of Gaussianity of a field, it also implies that it yields only a rather limited amount of topological information. This concerns key aspects such as the

topological composition of the cosmic mass distribution and the connectivity of the various topological elements. The implication is that considering homology, in terms of Betti numbers and even more that of topological persistence (Pranav et al. 2017) represent a major advance in understanding Gaussian fields.

The Betti number curves reveal a systematic dependence of relative populations of isolated mass concentrations, tunnels, and enclosed voids as a function of the power spectrum of a Gaussian random field. Our study finds a monotonic increase of the width of the β_1 curves as the power spectrum index n decreases: the number of tunnels increases steeply as the large-scale wavelength modes become more prominent. In addition, we find that there is a considerably larger density range over which the topology resembles a sponge-like morphology. In other words, configurations marked by the simultaneous presence of tunnels and cavities at the low-density regime, and of tunnels and islands at the high-density regime, exist over a wider density range as the spectral index n is lower. This also concerns the narrow density regime around the median density where all three topological features exist simultaneously.

The implications for the topology of the resulting spatial pattern of the evolved mass distribution are substantial. Gravitational evolution amplifies the topological differences in the initial conditions. A sponge-like topology evolves into a mass distribution resembling a connected network, while one that only involves isolated islands would merely produce a field of isolated collapsed density clumps. Given that primordial Betti numbers already elucidate and highlight such fundamental topological differences, suggests they have the potential of quantifying crucial aspects of the connectivity of the evolved cosmic matter distribution.

For true insight into the hierarchical evolution and development of the topology of the mass field, we will need to characterize in more detail how the various features connect up with each other. This is the subject of the second part of our investigation, to be reported in (Pranav et al., in preparation), where we will present and discuss the persistent homology of Gaussian fields.

11.1.3 Singularities and Betti numbers

As a prelude to our study of the persistent topology of Gaussian random fields (Pranav et al., in preparation), we also evaluate the relation between minima, saddle points, and maxima in the density field and Betti numbers. We focused in particular on the relationship between the zeroth Betti number and the number of maxima, i.e. peaks, in the density field. Assisted by the useful analytical expressions for the number density of peaks and minima (Bardeen et al. 1986) as consistency check, we have subsequently assessed the growth of peak number per density island in Gaussian fields. It reveals the subtle dependence of number of peaks per island as a function of power spectrum. While the number of islands and peaks are similar at very high density levels, we see that the convergence towards unity of the ratio of peaks to islands is very slow. This shifts strongly and systematically towards higher density levels as the index n decreases.

11.1.4 Betti numbers and Minkowski functionals

We also study in detail the extent to which Betti numbers contain topological information that is complementary to Minkowski functionals. One immediate observation is that of the power spectrum dependence of Betti numbers, which is a fundamental difference

with the power spectrum independence of the Minkowski functional curves.

One major difference concerns the power spectrum dependence of Betti numbers. By contrast, the shape of Minkowski functional curves, i.e. the value of Minkowski functionals as a function of density level ν , is independent of the Gaussian field's power spectrum. Nonetheless, ratios of Minkowski functionals do reveal a dependence on power spectrum, a fact that was exploited in a series of studies by Sahni and collaborators (see e.g. Sahni et al. 1998; Sheth et al. 2003; Shandarin et al. 2004) in the morphological analysis of structural Megaparsec features in evolved cosmic density fields. As we show here, it manifests itself in features in the primordial Gaussian field having a more flattened shape as the spectral index is lower.

We present a comprehensive visual assessment of the differences between Minkowski functionals and Betti numbers. In combination with the difference in power spectrum dependence, the systematic comparison demonstrates that Betti numbers, and persistence (Pranav et al., in preparation), contain a considerable amount of topological information that is complementary to that contained in Minkowski functionals.

11.2 Homology and cosmology: potential

The potential for exploiting the rich topological language of homology to the observational reality of the Universe is substantial. It opens the path towards a richer, more powerful, and insightful analysis of the connectivity and organization characteristics of emerging cosmic mass distribution in the form of the topologically complex and intricate structure of the cosmic web. Also, it allows a better understanding of structural aspects of the Gaussian primordial density field, and might even shed new light on the nature of the primordial CMB perturbations.

One particular intriguing example where topological signatures might reveal yet unknown cosmological features concerns the detection of possible non-Gaussianities in the primordial perturbation field. The discovery of such primordial non-Gaussianities in the temperature fluctuations in the CMB would provide unique insights on the physical processes that determined the nature of our Universe during the inflationary epoch (Bartolo et al. 2004; Baumann 2009; Chen 2010).

Even while the Planck satellite has set stringent upper limits on the amplitude of primordial non-Gaussian fluctuations, one may not exclude that these had a more intricate and elusive character than suggested by most multifield inflation theories. It may reflect itself in subtle topological markings for which the rich language of homology, in terms of Betti numbers and even more so of topological persistence, may provide a means of uncovering. There are theoretical indications, such as those presented by Feldbrugge et al. (in preparation), that demonstrate the potential of persistence to find non-Gaussian signatures. Even only Betti numbers have the ability to detect non-Gaussian signatures, as was discussed in considerable detail by Chingangbam et al. (2012) (for a recent contribution, see also Cole & Shiu 2018). In fact, the recent study by Pranav et al. (2018) of the homology of CMB measurements by the *Planck* satellite have uncovered some interesting effects, when comparing the observed CMB maps with respect to simulations based on Gaussian prescriptions. However, it remains to be ascertained if these signals are a genuine cosmological signal, and not arising from yet unknown data systematic or foregrounds.

Notwithstanding such uncertainties, as this study has argued in detail, homology considerably enriches the language for exploring

the nature and describing the spatial patterns of cosmological structures.

ACKNOWLEDGEMENTS

We are indebted to Herbert Edelsbrunner for encouragement, numerous discussions, and incisive comments. We also thank Keimpe Nevenzeel, Matti van Engelen, and Mathijs Wintraecken for many discussions and insights.

Parts of this work have been supported by the 7th Framework Programme for Research of the European Commission, under FET-Open grant number 255827 (CGL Computational Geometry Learning), European Research Council advanced grant URSAT (Understanding Random Systems via Algebraic Topology, PI: Robert Adler) number 320422, and European Research Council advanced grant ARTHUS (Advances in the research on Theories of the Dark Universe; PI: Thomas Buchert), number 740021. RvdW also acknowledges support from the New Frontiers of Astronomy and Cosmology program at the Sir John Templeton Foundation.

REFERENCES

- Adler R.J., 1981, *The Geometry of Random Fields: Classics in Applied Mathematics*. SIAM, Philadelphia
- Adler R. J., Agami S., Pranav P., 2017, *Proc. Natl. Acad. Sci. USA*, 114, 11878
- Adler R. J., Bartz K., Kou S. C., Monod A., 2017, preprint ([arXiv:1704.08562](https://arxiv.org/abs/1704.08562))
- Adler R.J., Bobrowski O., Borman M., Subag E., Weinberger S., 2010, *Borrowing Strength: Theory Powering Applications—A Festschrift for Lawrence D. Brown*. Inst. Math. Stat., Beachwood, OH, p. 124
- Adler R. J., Subag E., Taylor J. E., 2012, *Ann. Stat.*, 40, 2910
- Adler R.J., Taylor J., 2010, *Random Fields and Geometry*: Springer Monographs in Mathematics. Springer, Berlin
- Adler R.J., Taylor J., 2011, *Topological Complexity of Smooth Random Functions*. Vol. 2019 of *Lecture Notes in Mathematics*. Springer, Heidelberg
- Adler R.J., Taylor J., Worsley K., 2018, *Applications of Random Fields and Geometry: Foundations and Case Studies*, The Pennsylvania State University, Pennsylvania.
- Aghanim N., et al., 2018, preprint ([arXiv:1807.06209](https://arxiv.org/abs/1807.06209))
- Appleby S., Chingangbam P., Park C., Yogendran K. P., Joby P. K., 2018, *ApJ*, 863, 200
- Bardeen J. M., Bond J. R., Kaiser N., Szalay A. S., 1986, *ApJ*, 304, 15
- Bardeen J. M., Steinhardt P. J., Turner M. S., 1983, *Phys. Rev. D*, 28, 679
- Bartolo N., Komatsu E., Matarrese S., Riotto A., 2004, *Phys. Rep.*, 402, 103
- Baumann D., 2009, preprint ([arXiv:0907.5424](https://arxiv.org/abs/0907.5424))
- Beisbart C., Buchert T., Wagner H., 2001, *Physica A Stat. Mech. Appl.*, 293, 592
- Bendich P., Edelsbrunner H., Kerber M., 2010, *IEEE Trans. Visual. Comput. Graph.*, 16, 1251
- Bennett C. L. et al., 2003, *ApJS*, 148, 1
- Bertschinger E., 1987, *ApJ*, 323, L103
- Betti E., 1871, *Ann. Mat. Pura Appl.*, 2, 140
- Bobrowski O., 2012, *Algebraic Topology of Random Fields and Complexes*, PhD thesis, Technion
- Bobrowski O., Borman M. S., 2012, *J. Topol. Anal.*, 4, 49
- Bobrowski O., Kahle M., 2018, *Journal of applied and Computational Topology*, 1, 331
- Buchert T., France M. J., Steiner F., 2017, *Class. Quantum Gravity*, 34, 094002
- Canavezes A., Efstathiou G., 2004, *Astrophys. Space Sci.*, 290, 215
- Canavezes A. et al., 1998, *MNRAS*, 297, 777
- Cautun M. C., van de Weygaert R., 2011, preprint ([arXiv:1105.0370](https://arxiv.org/abs/1105.0370))
- Cheng D., Schwartzman A., 2018, *Bernoulli*, 24, 3422
- Chen X., 2010, *Adv. Astron.*, 2010, 638979

- Chen Y.-C., Ho S., Freeman P. E., Genovese C. R., Wasserman L., 2015, *MNRAS*, 454, 1140
- Chingangbam P., Park C., Yogendran K. P., van de Weygaert R., 2012, *ApJ*, 755, 122
- Chingangbam P., Yogendran K. P., Joby P. K., Ganesan V., Appleby S., Park C., 2017, *J. Cosmol. Astropart. Phys.*, 12, 023
- Choi Y.-Y., Park C., Kim J., Gott J. R., III, Weinberg D. H., Vogeley M. S., Kim S. S., SDSS Collaboration, 2010, *ApJS*, 190, 181
- Codis S., Pichon C., Pogosyan D., Bernardeau F., Matsubara T., 2013, *MNRAS*, 435, 531
- Codis S., Pogosyan D., Pichon C., 2018, *MNRAS*, 479, 973
- Cole A., Shiu G., 2018, *J. Cosmol. Astropart. Phys.*, 3, 025
- Doroshkevich A. G., 1970, *Astrophysics*, 6, 320
- Dunkley J. et al., 2009, *ApJS*, 180, 306
- Edelsbrunner H., Harer J., 2010, *Computational Topology: An Introduction*. Applied mathematics. Am. Math. Soc., Rhode Island
- Eisenstein D. J., Hu W., 1999, *ApJ*, 511, 5
- Elbers W., van de Weygaert R., 2018, preprint ([arXiv:1812.00462](https://arxiv.org/abs/1812.00462))
- Euler L., 1758, *Novi Commentarii academiae scientiarum Petropolitanae*, 4, 140
- Feldbrugge J., van Engelen M., 2012, *Analysis of Betti Numbers and Persistence Diagrams of 2-dimensional Gaussian Random Fields*, BSc. thesis, University of Groningen, Groningen
- Ganesan V., Chingangbam P., 2017, *J. Cosmol. Astro-Particle Phys.*, 2017, 023
- Gott J. R., III, Dickinson M., Melott A. L., 1986, *ApJ*, 306, 341
- Gott J. R., III et al., 1989, *ApJ*, 340, 625
- Gott J. R., III et al., 2008, *ApJ*, 675, 16
- Guth A. H., 1981, *Phys. Rev. D*, 23, 347
- Guth A. H., Pi S.-Y., 1982, *Phys. Rev. Lett.*, 49, 1110
- Hamilton A. J. S., Gott J. R., III, Weinberg D., 1986, *ApJ*, 309, 1
- Harrison E. R., 1970, *Phys. Rev. D*, 1, 2726
- Hikage C. et al., 2003, *PASJ*, 55, 911
- Hu W., Eisenstein D. J., 1999, *Phys. Rev. D*, 59, 083509
- Joby P.K., Chingangbam P., Ghosh T., Ganesan V., Ravikumar C.D., 2019, *Journal of Cosmology and Astroparticle Physics*, 2019, 009
- Jones B. J. T., 2017, *Precision Cosmology: The First Half Million Years*. Cambridge Univ. Press, Cambridge
- Kahle M., 2014, *Contemp. Math.*, Vol. 620, *Algebraic Topology: Applications and New Directions*. Amer. Math. Soc., Providence, RI, p. 201
- Kerscher M., 2000, in Mecke K. R., Stoyan D., eds, *Statistical Physics and Spatial Statistics. The Art of Analyzing and Modeling Spatial Structures and Pattern Formation* Vol. 554 of *Lecture Notes in Physics, Statistical Analysis of Large-Scale Structure in the Universe*. Springer Verlag, Berlin, p. 36
- Kerscher M., Mecke K., Schmalzing J., Beisbart C., Buchert T., Wagner H., 2001, *A&A*, 373, 1
- Kerscher M., Pons-Bordería M. J., Schmalzing J., Trasarti-Battistoni R., Buchert T., Martínez V. J., Valdarnini R., 1999, *ApJ*, 513, 543
- Kerscher M., Schmalzing J., Buchert T., Wagner H., 1997, in Bender R., Buchert T., Schneider P., von Feilitzsch F., eds, *Research in Particle-Astrophysics: The Significance of the Fluctuations in the IRAS 1.2 Jy Galaxy Catalogue*. Ringberg Castle, Tegernsee, p. 83
- Kerscher M., Schmalzing J., Buchert T., Wagner H., 1998, *A&A*, 333, 1
- Kolb E. W., Salopek D. S., Turner M. S., 1990, *Phys. Rev. D*, 42, 3925
- Komatsu E. et al., 2011, *ApJS*, 192, 18
- Liddle A. R., Lyth D. H., 2000, *Cosmological Inflation and Large-Scale Structure*, Cambridge Univ. Press, Cambridge
- Linde A. D., 1981, *Phys. Lett. B*, 100, 37
- Makarenko I., Bushby P., Fletcher A., Henderson R., Makarenko N., Shukurov A., 2018, *J. Plasma Phys.*, 84, 047303
- Makarenko I., Shukurov A., Henderson R., Rodrigues L. F. S., Bushby P., Fletcher A., 2018, *MNRAS*, 475, 1843
- Matsubara T., 2010, *Phys. Rev. D*, 81, 083505
- Mecke K. R., Buchert T., Wagner H., 1994, *A&A*, 288, 697
- Mecke K. R., Wagner H., 1991, *J. Stat. Phys.*, 64, 843
- Morozov D., 2005, *BioGeometry News*. Duke Univ, North Carolina
- Mukhanov V. F., Chibisov G. V., 1981, *ZhETF Pisma Redaktsiiu*, 33, 549
- Munkres J., 1984, *Elements of Algebraic Topology*. Advanced Book Classics. Perseus Books, New York
- Okabe A., 2000, *Spatial Tessellations: Concepts and Applications of Voronoi Diagrams*. Wiley Series in Probability and Statistics: Applied Probability and Statistics. Wiley, Hoboken, NJ
- Park C., Kim Y.-R., 2010, *ApJ*, 715, L185
- Park C. et al., 2013, *J. Korean Astron. Soc.*, 46, 125
- Patania A., Vaccarino F., Petri G., 2017, *EPJ Data Science*, 6, 7
- Peebles P., 1980, *The Large-scale Structure of the Universe*. Princeton series in physics. Princeton Univ. Press, Princeton
- Peebles P. J. E., Yu J. T., 1970, *ApJ*, 162, 815
- Planck Collaboration XIII, 2016, *A&A*, 594, A13
- Planck Collaboration XIII, 2016, *A&A*, 594, A17
- Pogosyan D., Gay C., Pichon C., 2009, *Phys. Rev. D*, 80, 081301
- Pranav P., 2015, *Persistent Holes in the Universe: A Hierarchical Topology of the Cosmic Mass Distribution*. PhD thesis. University of Groningen, Groningen
- Pranav P., Adler R. J., Buchert T., Edelsbrunner H., Jones B. J. T., Schwartzman A., Wagner H., van de Weygaert R., 2018, preprint ([arXiv:1812.07678](https://arxiv.org/abs/1812.07678))
- Pranav P., Edelsbrunner H., van de Weygaert R., Vegter G., Kerber M., Jones B. J. T., Wintraecken M., 2017, *MNRAS*, 465, 4281
- Robins V., 2006, *Phys. Rev. E*, 74, 061107
- Robins V., 2013, preprint ([arXiv:1304.7846](https://arxiv.org/abs/1304.7846))
- Robins V., 2015, *Algebraic Topology, in Digital Encyclopedia of Applied Physics*. Wiley, Hoboken, NJ, p. 1
- Rote G., Vegter G., 2006, *Computational Topology: An Introduction*. Springer, Berlin, Heidelberg, p. 277
- Sahni V., Sathyaprakash B., Shandarin S., 1998, *ApJ*, 507, L109
- Scaramella R., Vittorio N., 1991, *ApJ*, 375, 439
- Schaap W. E., van de Weygaert R., 2000, *A&A*, 363, L29
- Schmalzing J., Buchert T., 1997, *ApJ*, 482, L1 +
- Schmalzing J., Buchert T., Melott A., Sahni V., Sathyaprakash B., Shandarin S., 1999, *ApJ*, 526, 568
- Seljak U., Zaldarriaga M., 1999, *Astrophys. J. Suppl.*, 129, 431
- Shandarin S. F., Sheth J. V., Sahni V., 2004, *MNRAS*, 353, 162
- Sheth J. V., Sahni V., Shandarin S. F., Sathyaprakash B. S., 2003, *MNRAS*, 343, 22
- Sheth R. K., van de Weygaert R., 2004, *MNRAS*, 350, 517
- Shivashankar N., Pranav P., Natarajan V. v. d., Weygaert R., Bos E. G. P., Rieder S., 2016, *IEEE Trans. Visual. Comput. Graph.*, 22, 1745
- Smoot G. F. et al., 1992, *ApJ*, 396, L1
- Sousbie T., 2011, *MNRAS*, 414, 350
- Sousbie T., Pichon C., Kawahara H., 2011, *MNRAS*, 414, 384
- Spergel D. N. et al., 2007, *ApJS*, 170, 377
- Starobinsky A. A., 1982, *Phys. Lett. B*, 117, 175
- Taylor J., 2006, *Ann. Probab.*, 34, 122
- Taylor J. E., Worsley K. J., 2007, *J. Am. Stat. Assoc.*, 102, 913
- Tomita H., 1993, in Kawasaki K., Suzuki M., eds, *Formation, Dynamics, and Statistics of Patterns* Vol. 1, *Statistics and Geometry of Random Interface systems*. World Scientific, Singapore, p. 113
- van de Weygaert R., 2002, in Plionis M., Cotsakis S., eds, *Modern Theoretical and Observational Cosmology* Vol. 276 of *Astrophysics and Space Science Library*, Froth across the Universe. Springer, Berlin, Heidelberg, p. 119
- van de Weygaert R., Bertschinger E., 1996, *MNRAS*, 281, 84
- van de Weygaert R., Platen E., Vegter G., Eldering B., Kruithof N., 2010, Proc. 2010 Int. Symp. Voronoi Diagrams in Science and Engineering ISVD '10, Alpha shape topology of the cosmic web. IEEE Computer Society, Washington DC, p. 224
- van de Weygaert R., Schaap W., 2009, in Martínez V. J., Saar E., Martínez-González E., Pons-Bordería M.-J., eds, *Data Analysis in Cosmology* Vol. 665 of *Lecture Notes in Physics, The Cosmic Web: Geometric Analysis*. Springer Verlag, Berlin, p. 291
- van de Weygaert R. et al., 2011, preprint ([arXiv:1110.5528](https://arxiv.org/abs/1110.5528))
- van de Weygaert R. et al., 2011, *Trans. Comput. Sci.*, 14, 60

- van de Weygaert R. et al., 2011, *Transactions on Computational Science*, XIV. Springer Verlag, Berlin
- Vegter G., 1997, *Chapt. Computational Topology*. CRC Press, Inc., Boca Ratonp. 517
- Wasserman L., 2018, *Annu. Rev. Stat. Appl.*, 5, 501
- Weinberg D. H., Gott J. R., III, Melott A. L., 1987, *ApJ*, 321, 2
- Wiegand A., Buchert T., Ostermann M., 2014, *MNRAS*, 443, 241
- Wintraecken M., Vegter G., 2013, *Topology Appl.*, 160, 2175
- Xu X., Cisewski-Kehe J., Green S. B., Nagai D., 2018, preprint ([arXiv:1811.08450](https://arxiv.org/abs/1811.08450))
- Zeldovich Y. B., 1972, *MNRAS*, 160, 1P
- Zomorodian A. J., 2009, *Topology for Computing*. Cambridge Univ. Press, New York

APPENDIX A: GAUSSIAN FIELD PEAK DENSITY

For an evaluation of the number density of peaks in a Gaussian field, we use the expressions derived by Bardeen et al. (1986) for the (comoving) differential peak density $\mathbb{N}_{pk}(\nu)$ for peaks of (normalized) density $\nu = f_{pk}/\sigma$ in a density field $f_s(\vec{x})$ filtered on a spatial scale R_s .

A Gaussian field $f(\vec{x})$ filtered on a scale R_s with filter kernel $W_s(\vec{r}; R_s)$,

$$f_s(\vec{x}) = \int f(\vec{y}) W_s(\vec{y} - \vec{x}; R_s) d\vec{y}, \quad (\text{A1})$$

can be written in terms of the Fourier integral, following Parseval's theorem,

$$f_s(\vec{x}) = \int_{\mathbb{R}^3} \frac{d^3\vec{k}}{(2\pi)^3} \hat{f}(\vec{k}) \hat{W}(kR_s) \exp(-i\vec{k} \cdot \vec{x}), \quad (\text{A2})$$

in which $\hat{W}(kR_s)$ is the Fourier transform of the filter kernel. From this, it is straightforward to see that the corresponding power spectrum $P_s(k)$ of the filtered field is the product of the unfiltered power spectrum $P(k)$ and the square of the filter kernel $\hat{W}(kR_s)$

$$P_s(k; R_s) = P(k) \hat{W}^2(kR_s). \quad (\text{A3})$$

Two spectral parameters are instrumental for assessing the number density of peaks – and dips and other singularities – in the filtered density field. The spectral parameter γ and spectral scale R_* are combinations of various moments of the filtered power spectrum $P_s(k)$,

$$\gamma = \frac{\sigma_1^2}{\sigma_2\sigma_0}, \quad R_* = \sqrt{3} \frac{\sigma_1}{\sigma_2}, \quad (\text{A4})$$

in which the spectral moments σ_j are defined as

$$\sigma_j^2 = \int_0^\infty \frac{d^3\vec{k}}{(2\pi)^3} k^{2j} P_s(k), \quad (\text{A5})$$

(and thus $\sigma = \sigma_0$). To appreciate the dependence of the spectral parameters γ and R_* on the power spectrum and filter scale R_s of

the field, a useful reference is the values for a field with a power-law power spectrum of index n and filter scale R_s (Bardeen et al. 1986),

$$\gamma^2 = \frac{(n+3)}{(n+5)}, \quad R_* = \left(\frac{6}{n+5}\right)^{1/2} R_s. \quad (\text{A6})$$

The influence of the power spectrum and smoothing scale R_s on the cumulative and differential peak number densities propagates via the values and behaviour of the spectral parameters γ and R_* . The differential number density of peaks $\mathbb{N}_{pk}(\nu)$ in the filtered field $f_s(\vec{x})$ at normalized (dimensionless) density level $\nu = f_s/\sigma$ is given by (Bardeen et al. 1986),

$$\mathbb{N}_{pk}(\nu) d\nu = \frac{1}{(2\pi)^2 R_*^3} e^{-\nu^2} G(\gamma, \gamma\nu). \quad (\text{A7})$$

While an analytical expression for the function $G(\gamma, w)$ is not available, Bardeen et al. (1986) provide a fitting formula for the function $G(\gamma, w)$ that is accurate to better than 1 per cent over the range $0.3 < \gamma < 0.7$ and $-1 < w < \infty$, and even better than 1 in 10000 for $w > 1$,

$$G(\gamma, w) = \frac{w^3 - 3\gamma^2 w + [B(\gamma)w^2 + C_1(\gamma)] \exp[-A(\gamma)w^2]}{1 + C_2(\gamma) \exp[-C_3(\gamma)w]}. \quad (\text{A8})$$

The coefficients A and B can be inferred by assuring the fitting formula to agree with the asymptotic behaviour for peak at high ν , while C_1 , C_2 , and C_3 follow from the fitting procedure (see Bardeen et al. 1986, Section 4),

$$\begin{aligned} A &= \frac{5/2}{(9 - 5\gamma^2)}, & B &= \frac{432}{(10\pi)^{1/2} (9 - 5\gamma^2)^{5/2}}, \\ C_1 &= 1.84 + 1.13(1 - \gamma^2)^{5.72}, \\ C_2 &= 8.91 + 1.27 \exp(6.51\gamma^2), \\ C_3 &= 2.58 \exp(1.05\gamma^2). \end{aligned} \quad (\text{A9})$$

To find the cumulative number density $n_{pk}(\nu)$ of peaks in the filtered field $f_s(\vec{x})$ with a height of ν or higher, we need to evaluate the integral,

$$n_{pk}(\nu) = \int_\nu^\infty \mathbb{N}_{pk}(\nu) d\nu. \quad (\text{A10})$$

While in general the integral has to be evaluated numerically, its asymptotic value for the full peak density n_{pk} can be inferred analytically (Bardeen et al. 1986),

$$n_{pk} = n_{pk}(-\infty) = \frac{29 - 6\sqrt{6}}{5^{3/2} 2(2\pi)^2 R_*^3} = 0.016 R_*^{-3}. \quad (\text{A11})$$

We refer to the diagram in Figure 2 of Bardeen et al. (1986) for a representative sample of differential number density $\mathbb{N}_{pk}(\nu)$ curves for different values of spectral parameters γ . Likewise, Figure 3 in the same study shows the dependence of the cumulative peak density as function of normalized density threshold ν .

This paper has been typeset from a $\text{\TeX}/\text{\LaTeX}$ file prepared by the author.